ABSTRACT

Title of Thesis: POLARIZATION-INSENSITIVE TECHNIQUES

FOR OPTICAL SIGNAL PROCESSING

Degree candidate: Reza Salem

Degree and year: Doctor of Philosophy, 2006

Thesis directed by: Professor Thomas E. Murphy
Department of Electrical and Computer Engineering

This thesis investigates polarization-insensitive methods for optical signal processing. Two signal processing techniques are studied: clock recovery based on two-photon absorption in silicon and demultiplexing based on cross-phase modulation in highly nonlinear fiber. The clock recovery system is tested at an 80 Gb/s data rate for both back-to-back and transmission experiments. The demultiplexer is tested at a 160 Gb/s data rate in a back-to-back experiment. We experimentally demonstrate methods for eliminating polarization dependence in both systems. Our experimental results are confirmed by theoretical and numerical analysis.

POLARIZATION-INSENSITIVE TECHNIQUES

FOR OPTICAL SIGNAL PROCESSING

by

Reza Salem

Thesis submitted to the faculty of the Graduate School of the
University of Maryland, College Park in partial fulfillment
of the requirements for the degree of
Doctor of Philosophy
2006

Advisory Committee:

        Professor Thomas E. Murphy, Chair
        Professor Christopher C. Davis
        Professor Julius Goldhar
        Professor Ping-Tong Ho
        Professor Wendell T. Hill

ACKNOWLEDGEMENTS

I would like to give special thanks to my advisor Professor Thomas Murphy. His guidance, encouragement and support have definitely had a substantial impact on this work. I have learned experimental techniques, numerical methods and theoretical analysis from him. He also taught me how to present my work effectively and write professionally. What I have learned from Dr. Murphy will always be with me in my professional career and I greatly appreciate his time and effort. He has been a kind advisor, teacher and friend.

Several people have helped me with my PhD research projects. Most of the projects included in my thesis have been done in collaboration with Prof. Gary Carter's group from University of Maryland, Baltimore County (UMBC). I want to thank Dr. Carter for his support and useful discussions. I would also like to thank the researchers in his group, Dr. Gaston Tudury and Dr. Anthony Lenihan, for their help with various parts of this work. Gaston helped me with the clock recovery project and Anthony helped and provided ideas for the demultiplexing work. Without them I would not have been able to accomplish what is presented in this thesis. Finally, I want to thank Dr. Tim Horton from Laboratory for Physical Sciences for his help and support in parts of this work.

I want to thank the faculty members of the University of Maryland who were my teachers during these years of graduate studies. I especially want to thank Prof. Christopher Davis, Prof. Julius Goldhar, Prof. Ping-Tong Ho, and Prof. Wendell Hill for agreeing to

serve on my thesis committee. I have also benefited from discussions with them in preparing this thesis.

Amir-Ali Ahmadi was an undergraduate member of our group who helped a great deal in the clock recovery project. His work on the optical dithering system was very important to our progress. I have benefited from discussions with Paveen Apiratikul, a member of our research group, during various parts of my research. Also, Arash Komaei and Kuldeep Amarnath, both UMD graduate students, helped me with some theoretical and experimental work during the demultiplexing work. I thank all of them for their help.

Dr. Naoki Sugimoto from Asahi Glass Co. provided the bismuth-oxide-based nonlinear fiber that was used in the demultiplexing experiments. I greatly appreciate his help.

I am so grateful to my wife, Suzanne, for her help, love and support. She has always been supportive of my work and encouraged me to achieve my career goals. And finally, I want to thank my family, Hassan, Mansooreh and Mahsa, whose love and support from thousands of miles away have always given me the energy to work.

CONTENTS

LIST OF TABLES

LIST OF FIGURES

1. INTRODUCTION

The demand for higher communication bandwidth especially caused by the growth of the internet has stimulated new changes in the architecture of optical communication networks. One of the ways to increase the data rate in optical communication systems is to define different data channels carried by different optical wavelengths. This method is called wavelength division multiplexing (WDM) and has been deployed in current optical networks. Another approach proposed for next generation optical networks is to define different optical channels carried by the same wavelength and multiplex them in the time domain. This method is called optical time division multiplexing (OTDM) and future optical communication systems can be seen as a combination of WDM and OTDM methods. New advances in high-speed ethernet technology have also shown the necessity to multiplex data from different users in the time domain. For example in 10 Gb/s ethernet system, it is impractical to assign a different wavelength to each user. OTDM networks can be realized using systems that multiplex and demultiplex optical pulses in the time domain. The data rate in the future OTDM systems will be a multiple of the data rate in each data channel. Therefore the data rate in such systems will go beyond the speed of available electronic circuits making it almost impossible to perform signal processing on the data by means of current

electrical methods.

One way to process very fast optical signals without relying on high-speed electronics is to use optical nonlinear processes that have very fast response times. This method has been the most common way to demonstrate high-speed OTDM systems in recent years [1–4]. However, there are several disadvantages associated with the use of nonlinear optical processes instead of conventional signal processing methods. One of these problems is the polarization dependence of nonlinear processes. In fiber optic networks, optical data may travel through thousands of kilometers of fiber, which causes the light polarization state to fluctuate. In addition, thermal effects and mechanical vibrations cause polarization fluctuations. The speed of polarization fluctuations can be very high (microsecond scale) especially when a WDM configuration is desired [5]. Polarization tracking at these high speeds is both difficult and expensive. These fluctuations are unimportant in most optical receivers that are currently used in optical networks. This is because the process of photo-detection is polarization independent. In high-speed optical receivers that use nonlinear optics, the polarization dependence issue should be addressed.

In this thesis, we investigate methods to build a polarization-independent receiver. We study two systems that are used as main sections of an OTDM receiver (clock recovery and demultiplexing). The first system is clock recovery based on two-photon absorption in silicon and the second one is a demultiplexer based on cross-phase modulation in fiber. In the next sections of this chapter we review some of the work done in clock recovery and demultiplexing. We also review some of the methods for achieving polarization-insensitive

2

systems. Chapter 2 explains the development of clock recovery system based on two-photon absorption. In this chapter we also investigate the polarization dependence issue in the clock recovery process theoretically and experimentally. Finally, we show how the clock recovery system can be incorporated into a long distance transmission system. Chapter 3 presents our work in optical demultiplexing using cross-phase modulation in nonlinear fibers. We investigate new techniques for performing polarization-independent cross-phase modulation in nonlinear fibers. Photonic crystal fiber and bismuth-based nonlinear fiber are used in our experiments to demonstrate these two techniques. We provide computer simulation results that confirm our experiments and prove the polarization-insensitivity of these methods.

1.1   Signal Processing in OTDM Networks

In the past decade a great deal of attention has been paid to the applications of nonlinear optical processes. One of the main motivations for research in this area is the fast time response of these processes. One of the first applications of nonlinear optics was performing autocorrelation measurements on very short optical pulses generated by pulsed laser sources. The introduction of ultra-fast OTDM systems fuelled the research on nonlinear optics. A simplified diagram of an OTDM system is shown in Fig. 1.1. In such a scheme, N data channels with a bit rate of f_0 are generated by N transmitters (TX1,...,TXN). A multiplexer is used to combine these channels into a single fiber with an aggregate rate of
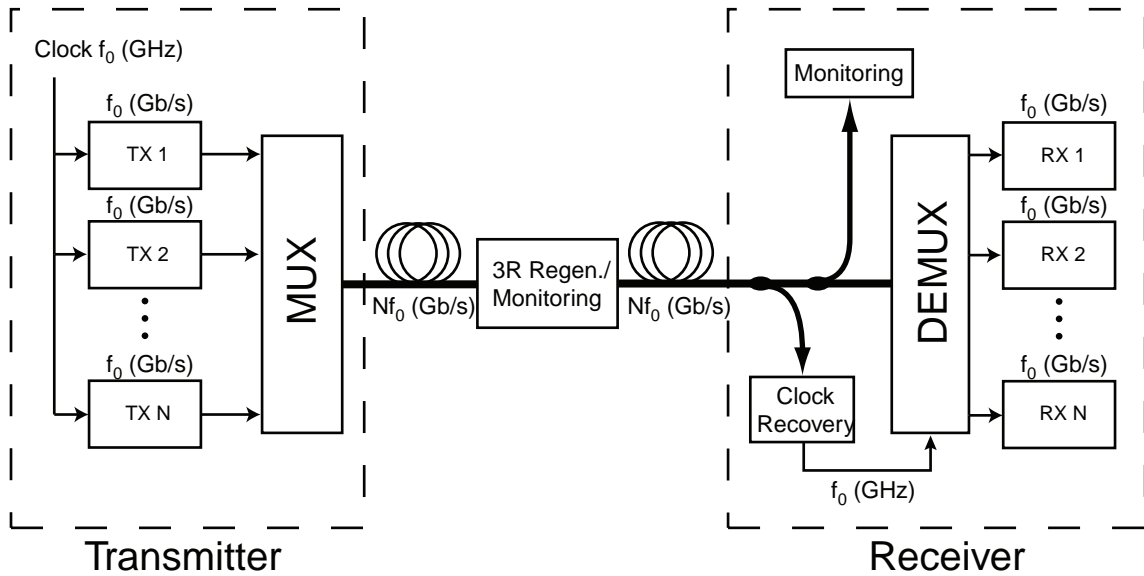
Fig. 1.1: Diagram of Optical Time Division Multiplexed (OTDM) system.

$N \times f_0$. Depending on the distance over which the data is sent, there might be a 3R regen-erator section at a number of intermediate points on the transmission line. At the receiver, part of the signal is used to perform clock recovery to generate the original data clock (f_0). This recovered clock is used to demultiplex the data into N channels that can be received by N receivers (RX1,...,RXN). In some cases a monitoring section can be added to the re-ceiver or somewhere along the transmission fiber that can include measurement of chirp, pulse shape, polarization mode dispersion, degree of polarization and eye diagram.

As seen in this diagram, 3R regeneration, clock recovery, demultiplexing and perfor-mance monitoring all have to be done at the aggregate data rate of $N f_0$, a speed well beyond the capabilities of electronics. Therefore all of these tasks require some optical

signal processing technique in order to be realized in optical networks. Clock recovery and demultiplexing are two major tasks in an OTDM receiver and in this thesis we focus on these two.

1.2   Optical Clock Recovery

As seen in Fig. 1.1 the first stage in receiver is the clock recovery. In addition to the receiver section, one of the regenerating processes that is done in 3R regenerator is re-timing which requires a clock recovery process as well. Electrical clock recovery systems have been used for data rates up to 40 Gb/s, a rate that is limited by the speed of electronic circuits. Optical clock recovery has been demonstrated using nonlinear optical processes for data rates up to 400 Gb/s [6]. Techniques previously used for optical clock recovery include injection locked laser cavities [7–9], electrical ring oscillators [10–12], and a variety of optical phase-locked loop systems [6, 13–16]. The third method, which is based on phase locking, can be realized by nonlinear optical processes. In this method, optical clock recovery is achieved by measuring the timing discrepancy between incoming optical data and a local optical clock using a nonlinear optical process. Figure A.1 shows a simple diagram of this method. In most cases the nonlinear process is followed by a slow optical detector. Many nonlinear processes have been exploited for the type of system shown in this diagram. These processes include four-wave mixing in fiber [13] or semiconductor waveguides [6], cross-absorption modulation in electroabsorption modulators (EAM) [14],

5

and cross-phase-modulation in semiconductor amplifiers [15], and optoelectronic mixing in modulators [16, 17].

Although these methods have enabled sub-harmonic clock recovery at speeds up to hundreds of Gb/s, few of these techniques provide polarization- and wavelength- independence comparable to what is routinely achieved in slower electronic clock recovery systems.

Methods for mitigating polarization dependence include polarization interleaving [18], in which neighboring pulses are orthogonally polarized and polarization diversity [19, 20], in which the optical signal is split into orthogonally polarized components that are processed separately. Each of these techniques introduces additional complexity in the system that would not be necessary if the underlying optical process were itself polarization independent. Injection-locking techniques have been shown to have lower polarization-dependence [7], but they are usually tied to a specific repetition frequency and wavelength.

Wavelength-dependence is another challenge associated with optical clock recovery. With the exception of DFB lasers, most components in optical communication systems (e.g., modulators, amplifiers, photodetectors) can be used for many different wavelength channels without incurring a significant penalty. By contrast, many of the nonlinear optical techniques used in optical clock recovery systems require specific wavelengths for both the clock and data. In some cases the clock and data must be sufficiently separated in wavelength to be spectrally distinguishable, for example, when an optical filter is used to separate the clock and data after mixing. In some cases, the clock and data cannot

6

Data In
Nf$_0$(Gb/s) →

Nonlinear Medium → slow PD → H(ω) loop filter → VCO → Electrical Clock Out f$_0$(GHz)

Optical Clock f$_0$(GHz) ← Optical Pulse Source ←
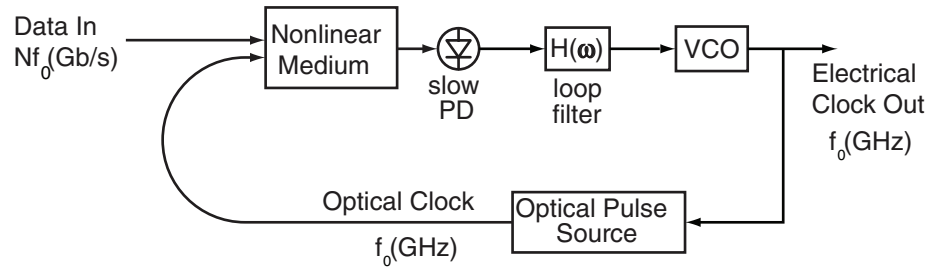
Fig. 1.2: Diagram of optical subharmonic clock recovery system based on phase-locked loop.

be too far apart because the nonlinear mixing efficiency decreases with separation. For many nonlinear processes, the attainable wavelength range is limited by phase-matching conditions or the wavelength characteristics of the devices used. In wavelength-division multiplexed networks, it is especially important that the clock recovery not be constrained in wavelength.

In Chapter 2, we demonstrate a high-speed clock recovery system based on two-photon absorption in silicon. In this case, the nonlinear process and slow detection shown in Fig. 1.2 are combined into the same device. The device used in these experiments is a silicon avalanche photodiode. Also, we develop a model that predicts the polarization dependence, and a new technique to minimize it. We demonstrate low polarization sensitivity and wide optical bandwidth for this system. We also demonstrate a long-haul transmission experiment using this clock recovery system.

7
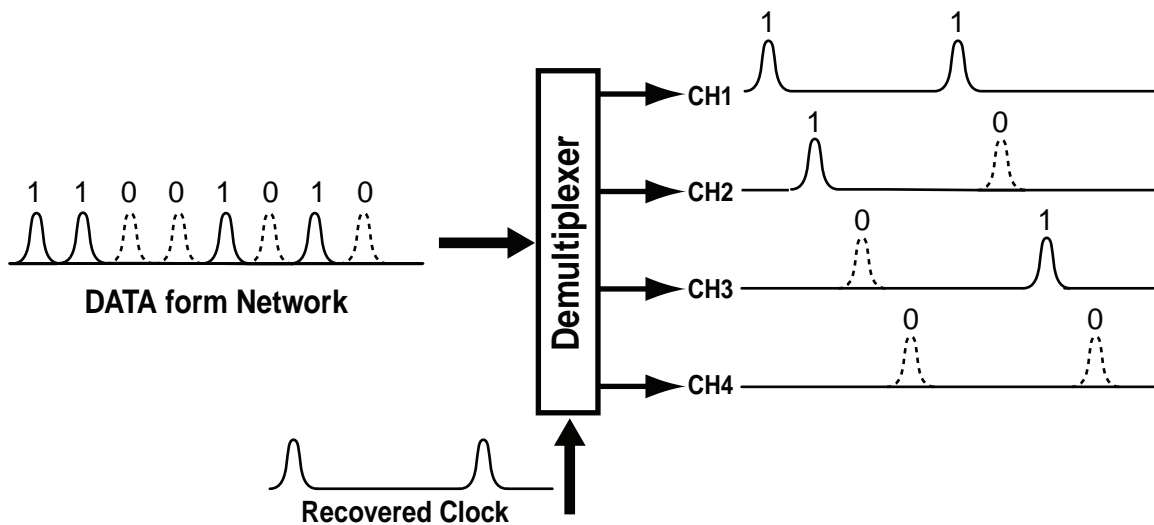
Fig. 1.3: Diagram of a demultiplexer in OTDM system.

1.3   Optical Demultiplexing

After the clock rate is recovered it can be used in a demultiplexer to extract one tributary

channel from a high-speed data stream. Fig. 1.3 shows a simple diagram of demultiplexing

in an OTDM system. In this example, a high-speed stream of data is demultiplexed into 4

channels at $\frac{1}{4}$ the original data rate. Nonlinear optical processes were also used in demon-

strating high-speed OTDM demultiplexing for data rates higher than the speed of electronic

circuits. Cross-absorption modulation in electroabsorption modulator [21], four-wave mix-

ing in fiber [19] and semiconductor optical amplifiers [22], cross-phase modulation in non-

linear optical loop mirror containing fiber [23] or semiconductor amplifier [24], cross-phase

modulation with spectral filtering using semiconductor amplifier [25] or fiber [7, 26] have

been used to perform optical demultiplexing.

8

Among the techniques for optical demultiplexing, those that use optical fiber nonlinearities like cross-phase modulation (XPM) or four-wave mixing (FWM) are attractive because of their fast response time and low insertion loss. One problem with fiber-based nonlinearities is that the FWM or XPM efficiency depends on the polarization state of the incoming data signal, which cannot be controlled in most fiber optic systems [26–28].

In theory, polarization-independent mixing can be achieved if the clock signal is circularly polarized, but in practice the residual birefringence of the fiber makes it difficult to maintain a circular polarization state over the length of the fiber. One method to maintain circular polarization is to twist the fiber either during or after fabrication [29, 30], but this approach cannot be easily implemented in fibers with significant linear birefringence. Another method to overcome polarization dependence is polarization diversity, in which the clock is split into two orthogonal states that independently interact with the data [19, 31–34]. In longer fibers, the random polarization mode dispersion can cause the polarization dependence to average out, leading to polarization-independent operation [35].

In the second part of this thesis, we introduce two new methods for performing polarization-independent cross-phase modulation in optical fibers. The two methods are demonstrated using two different nonlinear fibers and are both used in demultiplexing systems. These methods are not based on polarization diversity and do not add to the system complexity.

2. OPTICAL CLOCK RECOVERY BASED ON TWO-PHOTON

ABSORPTION

In this chapter we describe the concept of using two-photon absorption (TPA) to synchronize a clock and data signal. We start by explaining the nonlinear process of two-photon absorption in silicon. Then we describe the principle of operation of optical phase-locked loop based on this process. Next, we demonstrate an 80 Gb/s clock recovery system based on TPA in back-to-back and transmission experiments. Finally, the issue of polarization dependence in the presented clock recovery system is investigated. We use theoretical and experimental results to study the polarization dependence issue.

Constructing a phase-locked loop (PLL) to synchronize data and clock signals requires
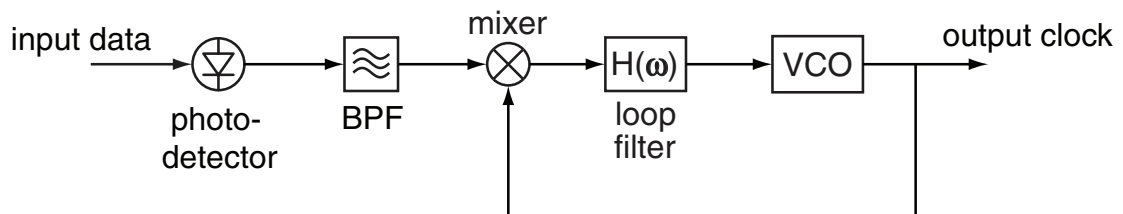
Fig. 2.1: Diagram of electrical clock recovery system.

the generation of a cross-correlation signal that measures the timing difference between the two signals. In electrical clock recovery systems, this is accomplished using an electrical mixer as shown in Fig. 2.1. For high-speed systems, the mixer may be replaced by a faster nonlinear optical process as shown in Fig. 1.2. One candidate nonlinear process that we explore here is two-photon absorption (TPA). Although TPA has been widely used in auto-correlation measurements [36], it has not been utilized as much in optical communications applications.

If E_g is the bandgap energy of a semiconductor material and $h\nu$ is the photon energy and the following condition is satisfied:

$$h\nu > \frac{E_g}{2} \quad , \tag{2.1}$$

two photons can be absorbed at the same time and generate an electron-hole pair in the semiconductor that in turn produces a photocurrent. The difference between this process and linear absorption process in an optical detector is shown in the simple diagram of Fig. 2.2. As seen in this diagram, two-photons can generate one electron-hole pair in the TPA process. In silicon ($E_g \simeq 1.12\text{eV}$), TPA can be observed for wavelengths ranging from 1100 nm to 2200 nm. The linear absorption in this case is negligible because $h\nu < E_g$. This is the ideal condition for observing the TPA since the linear absorption (when present) is much higher than the TPA and can make it difficult to detect the TPA. In our experiments we utilize a silicon avalanche photodiode which converts the optical power absorbed thought

11

LINEAR ABSORPTION   TWO PHOTON ABSORPTION
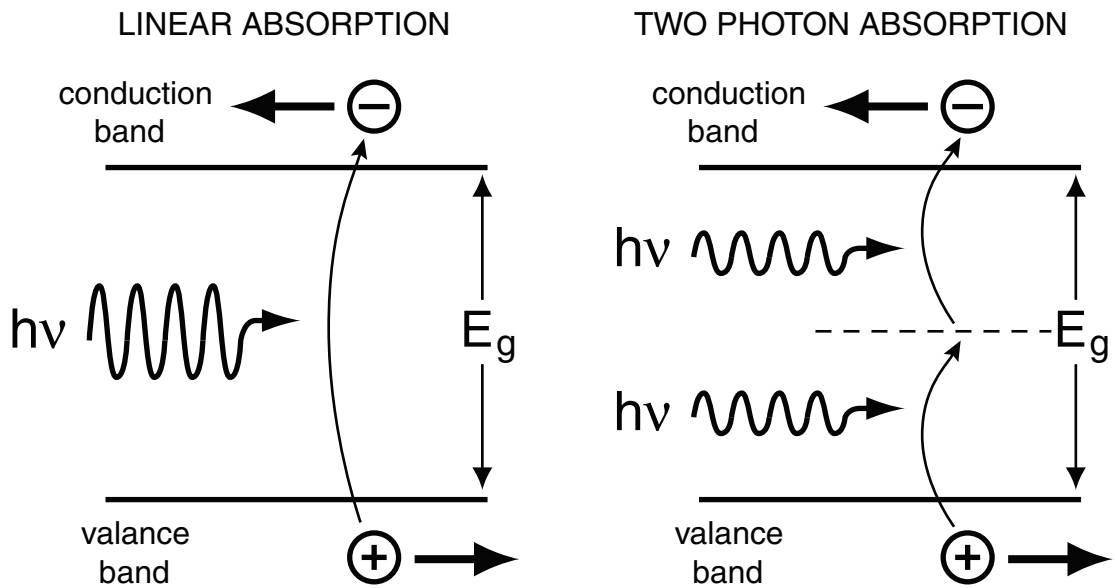
Fig. 2.2: The absorption of photons in a two-level system showing the difference between linear (single-photon) and nonlinear (two-photon) absorptions.

the TPA process into an electric current that can be easily measured.

Unlike conventional (linear) photo-detection, two-photon absorption produces a photocurrent proportional to the square of the optical power. Because of this quadratic nonlinearity, two-photon absorption can be used to measure the correlation between high-speed optical signals, in much the same way that sum-frequency generation is used in optical autocorrelators to diagnose pulses that are too short to be measured electrically. Two-photon absorption was first used in ultrashort pulse measurements more than three decades ago [37]. TPA as an alternative to second order nonlinearity has been demonstrated for measuring the pulse width of very short laser pulses using autocorrelation techniques. Different detectors

and devices have been used to perform TPA-based autocorrelation measurement. One of the devices used to build a highly sensitive autocorrelator for a 1550 nm wavelength laser is a silicon avalanche photodiode [38]. The same method can be modified to be used as a cross-correlation measurement technique by using two different signals [39]. There are few examples of cross-correlation measurements on high-speed time-division multiplexed signals [40] and also a chirp measurement technique that can be used in communication systems [41]. Also, there have been reports of performance monitoring [42] and all-optical light modulation [43] using TPA. Beyond these examples that are based on pulse characterization techniques, the applications of TPA for ultra-fast OTDM systems has not been broadly investigated.

Detection of TPA is simply done by a single photo-detector. Unlike some other nonlinear processes such as sum-frequency generation [44] and four-wave mixing [45], TPA does not require phase-matching. The TPA process has been shown to exhibit ultra-fast response time in autocorrelation measurements. In Ref. [46], TPA in a silicon photodiode was used to measure 20-fs optical pulses. Also, in Ref. [47], TPA in a GaAsP detector was used to characterize a 6-fs optical pulse. These examples show one of the main motivations for this research, which is the high-speed response of the TPA process, and the associated broad optical bandwidth. Linear (single-photon) detectors often exhibit nonlinear responses such as saturation for certain input power levels. These nonlinearities are usually due to electrical effects inside the semiconductor or the detector circuit. It is important to note that these types of nonlinearities are not ultra-fast and their speed is limited to the speed of the

detector circuit. Therefore, the main advantage of the TPA detection comes from the fact that the nonlinear process is ultra-fast.

2.1   Nonlinear Absorption of Light in a Photodiode

In a photodiode like the one used in our experiments, the absorption layer can be modelled as a thin slab. The light which is focused onto a small spot travels through the slab and gets absorbed as it goes through. There are practical issues that can complicate this model such as the reflection from the back surface of the absorption layer. These factors have been considered in [48], but in this thesis we will briefly consider the simplified case just to give an estimate of how much light gets absorbed in a thin slab of material.

The amount of light absorbed in TPA process can be estimated if the beam form and dimensions of the absorbing layer are given. Consider a slab of absorbing material with thickness d and light travelling along the z direction, which is perpendicular to the slab. The two-photon absorption coefficient β gives the rate of change in the intensity of light as it travels through the medium:

$$\frac{dI}{dz} = -\beta I^2 \tag{2.2}$$

At first let us assume the light beam travelling through the medium is a plane wave with constant intensity in a confined area A. In that case the power of the beam as a function of z can be written as $P(z) = I(z)A$. If the input intensity at $z = 0$ is I_0, we can write the

output intensity at $z = d$ by solving the differential equation given by Eq. 2.2:

$$I(d) = \frac{I_0}{1 + \beta d I_0} \tag{2.3}$$

Therefore, the change in the light intensity $\Delta I = I_0 - I(d)$ is given by:

$$\Delta I = \frac{\beta d I_0^2}{1 + \beta L I_0} \tag{2.4}$$

If we assume every two photons that are absorbed through the TPA process generate one electron-hole pair in the detector, the photocurrent density generated in the detector is given by:

$$J_{\text{TPA}} = \left(\frac{e}{2h\nu}\right) \Delta I = \left(\frac{e}{2h\nu}\right) \frac{\beta d I_0^2}{1 + \beta d I_0} \tag{2.5}$$

It is interesting to look at this equation in two limiting cases:

- When the absorbed intensity (ΔI) is much smaller than the input Intensity or $\beta d I_0 \ll 1$, Eq. 2.5 yields:

$$J_{\text{TPA}} \approx \left(\frac{e\beta d}{2h\nu}\right) I_0^2 \tag{2.6}$$

Therefore, the relationship between the photocurrent ($i_{\text{TPA}} = J_{\text{TPA}} A$) and incident power P is a quadratic relationship:

$$i_{\text{TPA}} \approx \eta P^2 \quad , \quad \eta = \frac{e\beta d}{2h\nu A} \quad , \tag{2.7}$$

15

where η is a quantity that determines the efficiency of the TPA detection.

- When most of the incident intensity gets absorbed in the medium or $\beta d I_0 \gg 1$,
  Eq. 2.5 yields:

$$J_{\text{TPA}} \approx \left(\frac{e}{2h\nu} \right) I_0 \tag{2.8}$$

Therefore, the relationship between the photocurrent and incident power is a linear

one:

$$i_{\text{TPA}} \approx \eta' P \quad , \quad \eta' = \frac{e}{2h\nu} \quad , \tag{2.9}$$

In our experiments we use a silicon photodiode. The TPA coefficient for silicon is about

0.8 cm/GW [49, 50]. The detector is designed for linear absorption of light around 800

nm wavelength. For this design the thickness of the absorption region is typically 50-100

μm. If we assume 100 mW of CW power focused on a spot with 3 μm diameter, the

incident intensity is $I_0 \simeq 1.4 \times 10^{10}$ W/m^2. Using this intensity and assuming $d = 100$

μm, the dimensionless parameter $\beta d I_0$ is about 1.12×10^{-5}. Therefore, only a very small

portion (0.01 percent) of the input power gets absorbed and we are well within the quadratic

operation region of the detector.

The plane wave assumption is not very realistic when the light is focused on a small spot

using a lens. In this case, the Gaussian beam formulation can better describe the intensity

profile. In a Gaussian beam the intensity is a function of z and the distance r from the beam

axis:

$$I(r, z) = I(0, z) \exp \left(-\frac{2r^2}{w^2(z)} \right) \quad , \tag{2.10}$$

16

where $w(z)$ shows the beam radius which depends on the distance from the beam waist by:

$$w^2(z) = w_0^2 \left[1 + \left(\frac{z}{z_0} \right)^2 \right] \quad .$$

(2.11)

In this equation, w_0 is the beam radius at the beam waist and $z_0 = \dfrac{\pi w_0^2}{\lambda}$. As we discussed before, the beam power stays essentially constant throughout the absorption layer because a very small portion of the light gets absorbed in the TPA process. Therefore, the intensity along the axis of the beam can be related to the incident optical power by this equation:

$$I(0, z) = \frac{2P}{\pi w^2(z)}$$

(2.12)

Using this equation and integration over the thickness of the absorption layer, the total absorbed power in the detector is calculated to be:

$$P_{\text{abs}} = \frac{2n\beta}{\lambda} \tan^{-1} \left(\frac{\lambda d}{2\pi n w_0^2} \right) P^2 \quad ,$$

(2.13)

where P is the power of the incident beam and n is the slab refractive index. Now let us look at the limiting cases of this absorbed power:

- The spot-size is big enough so that the detector can be considered a very thin slab, mathematically: $z_0 \gg \dfrac{d}{2n}$. By approximating the inverse tangent with its argument

17

we get:

$$P_{\text{abs}} \simeq \frac{\beta d}{\pi} \frac{P^2}{w_0^2} \tag{2.14}$$

This equation shows that the absorbed power is inversely proportional to πw_0^2 which

is the spot area.

- The spot-size is very small and the thickness of the detector is much bigger than the

  confocal parameter of the beam, mathematically: $z_0 \ll \dfrac{d}{2n}$. In this case the value of

  the inverse tangent is approximately $\dfrac{\pi}{2}$ and we get:

$$P_{\text{abs}} \simeq \frac{n\beta\pi}{\lambda} P^2 \tag{2.15}$$

This equation shows that for very small spot-sizes the absorbed power has a limit

and cannot be further increased by making the spot-size smaller. This is the most

important result of this calculation which indicates a limit for the TPA photocurrent

as the spot-size of the beam is decreased.

2.2   Principle of Operation of the Phase-Locked Loop

Fig. 2.3 plots the measured photocurrent as a function of the input optical power for the

silicon avalanche photodiode used in this work, clearly showing the quadratic relationship

over several orders of magnitude. In these measurements, a continuous-wave (CW) optical

signal at 1550 nm was focused through a microscope objective to a 3 μm spot on the surface

18
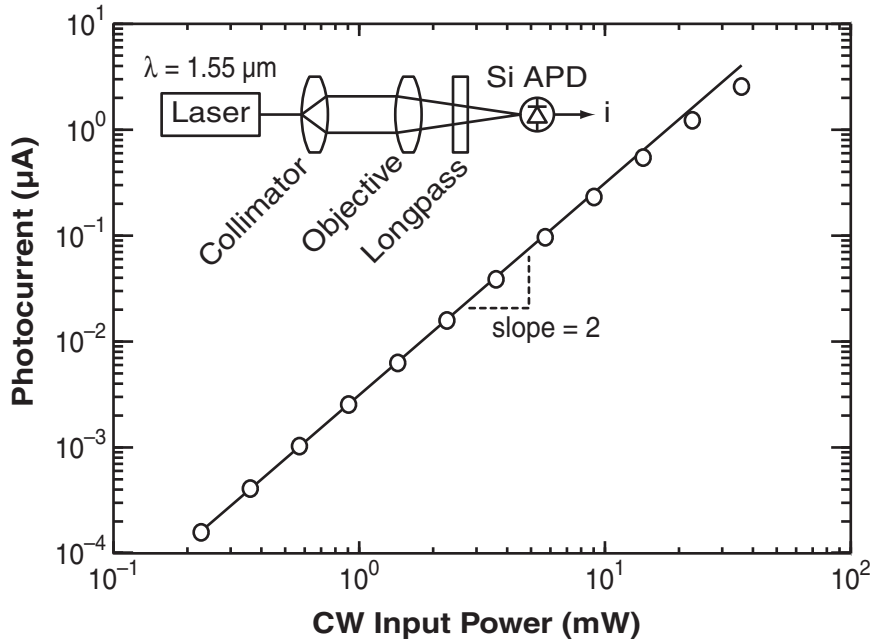
Fig. 2.3: Measured photocurrent as a function of the CW optical input power for the silicon avalanche photodiode used in this work.

of the silicon detector. A long-pass filter was inserted to block shorter wavelengths that would otherwise produce a linear photocurrent. Although TPA is an inefficient process, with inherently low quantum efficiency, we can observe a measurable photocurrent even for milliwatt CW power levels.

This quadratic response allows us to measure the cross-correlation signal between two optical pulses. In particular, in a clock recovery system, we are interested in the cross-correlation signal between optical data (from the network) and optical clock (generated locally). The cross-correlation signal measures the timing discrepancy between clock and data which can be used as the error signal in a phase-locked loop. This concept is shown in
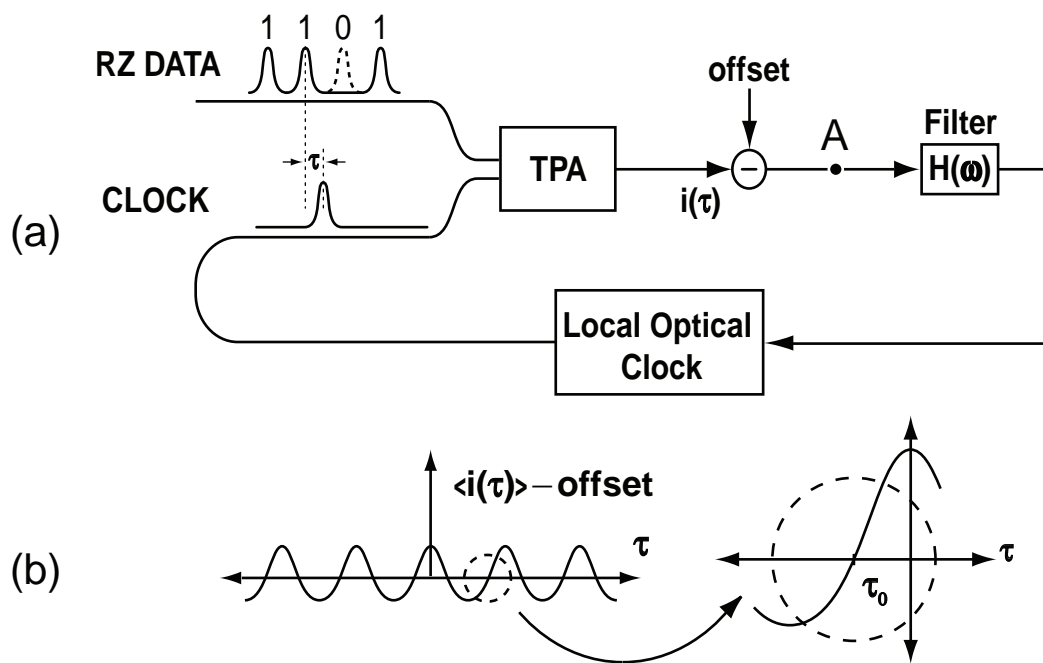
Fig. 2.4: Block diagram for Phase-Locked Loop based on TPA (a). Signal at point "A" showing the typical phase-detector output (b).
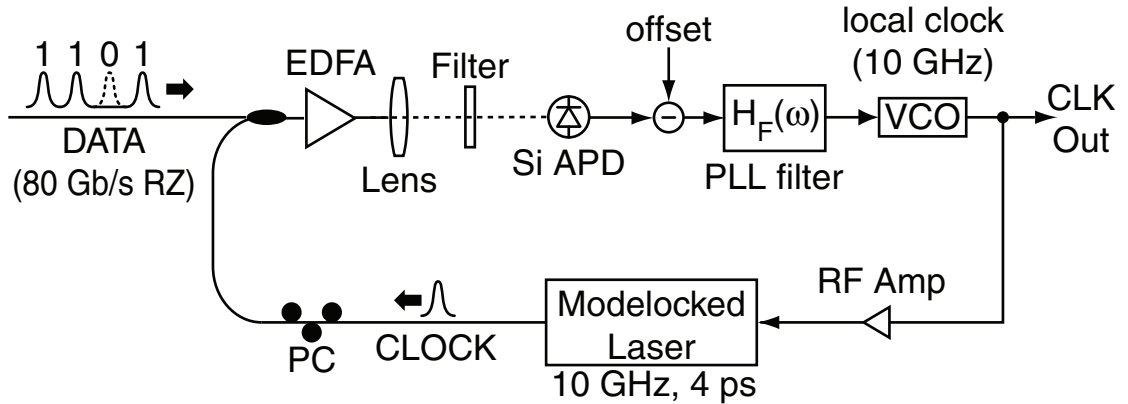
Fig. 2.5: Diagram of 80 Gb/s optical clock recovery system.

Fig. 2.4. As shown in the block diagram, in order to use the output of TPA detector as the error signal, a constant offset voltage should be subtracted from the output of the detector (point A). The PLL synchronized data and clock together at the time delay τ_0 shown in this figure.

2.3   80 Gb/s Clock Recovery Experiment

2.3.1   Experimental Setup

Fig. 2.5 depicts the experimental setup used to demonstrate 80 Gb/s clock recovery using two-photon absorption [51]. The 10 GHz, 4 ps clock pulses were generated from a semiconductor mode-locked laser driven by an electrical voltage-controlled oscillator. Data pulses with duration of 4 ps were generated using a 10 GHz mode-locked fiber laser, which
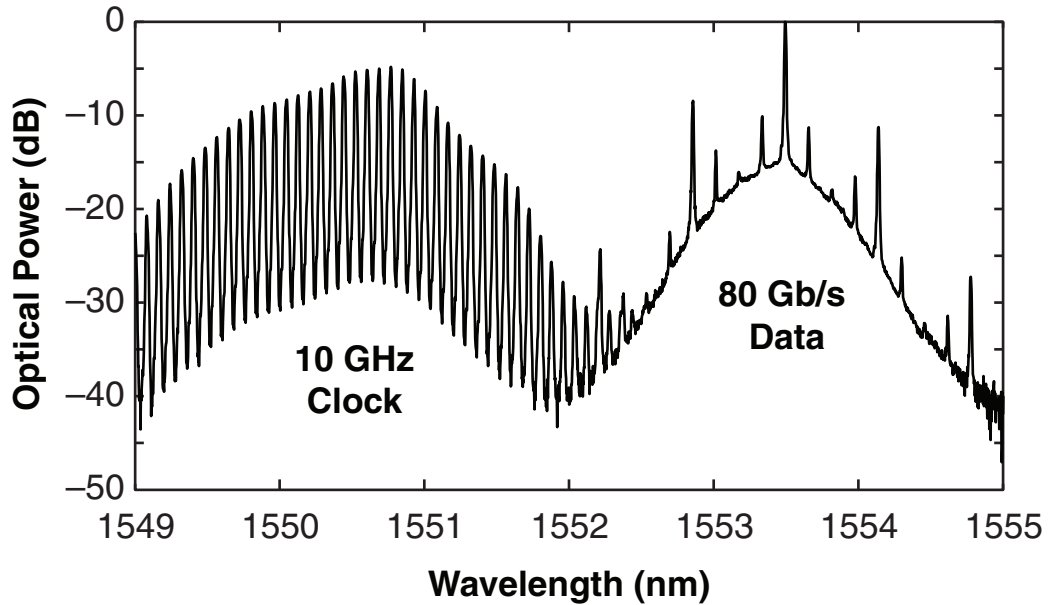
Fig. 2.6: Optical spectrum of the 10 GHz clock and 80 Gb/s data.

was passively multiplexed to 40 GHz and on-off modulated with a $2^{23} - 1$ pseudorandom binary data sequence. One additional multiplexing stage was employed to produce an 80 Gbit/s data sequence. The average optical powers of data and clock signals impinging on the detector surface were 3 mW and 6 mW respectively. Fig. 2.6 shows the optical spectrum of combined data and clock signals.

Fig. 2.7(a) depicts the cross-correlation between the 10 GHz optical clock and 80 Gb/s RZ data signal, as measured by two-photon absorption in the silicon photodiode. The measurement was performed while the phase-locked loop is disabled (open) and there is a constant frequency difference (about 3 kHz) between the two synthesizers that generate data and clock signals. As mentioned before, offset-subtraction is necessary in order to

obtain a bipolar error signal for the PLL. Fig. 2.7 (b) shows one of the zero crossing points to which data and clock signals are synchronized. When the clock synthesizer is free-running and the loop is enabled (closed) this bipolar error signal is driven to zero by the negative feedback in the loop.

The electrical filter $H_F(\omega)$ was designed so that the phase-locked loop would have a closed-loop transfer function with 5.5 kHz bandwidth. The system diagram for the PLL, loop filter design and the close-loop transfer function are described in Appendix A of this thesis. Fig. 2.8 (a) shows the theoretical closed-loop transfer function of the PLL indicating a third order response and a 5.5 kHz bandwidth. Part (b) of Fig. 2.8 plots the step response of the PLL as calculated (dashed curve) and measured (solid curve) showing good agreement between the two. The step response was measured by observing how the error signal responds when a square wave stimulus is artificially applied inside of the phase-locked loop. As seen here, the rise-time of the phase-locked loop is about 0.15 ms.

One important figure of merit of a clock recovery system is the timing jitter of the recovered clock. The output electrical clock is a sinusoidal signal with a randomly varying phase deviation $\phi(t)$. The one-sided power spectral density of the phase deviation is $S_\phi(f)$. According to [52], the signal phase noise is defined as $\frac{1}{2}S_\phi(f)$. The factor $\frac{1}{2}$ is due to the fact that the measured phase noise is double-sided (on both sides of the carrier). The measurement of phase noise is performed using the following relationship:

$$\text{phase noise} = \frac{\text{power density in spectral sideband, per Hz}}{\text{total signal power}} \quad , \qquad (2.16)$$

23
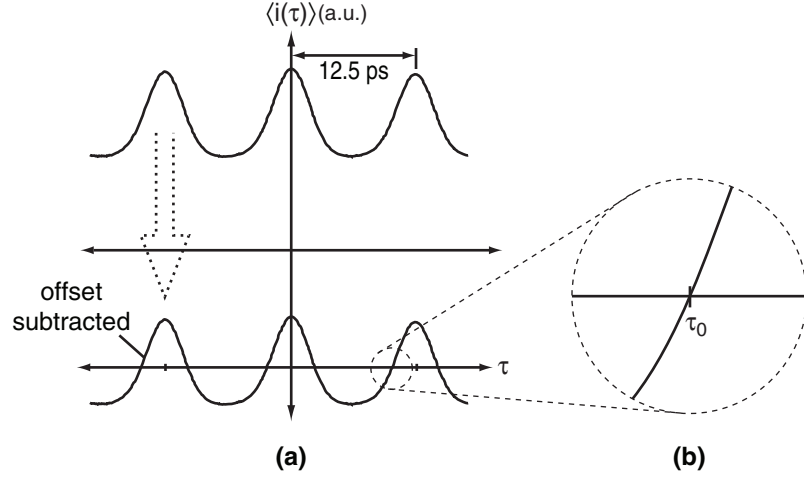
Fig. 2.7: (a) Measured cross-correlation between 10 GHz clock and 80 Gb/s data before and after the offset is subtracted. (b) Magnified view of cross-correlation, showing the zero-crossing location.

which is expressed in dBc/Hz (dB below the carrier per Hz) units. Phase jitter is the integral of $S_\phi(f)$ over the frequency range of the application:

$$\phi_{\text{jitter}}^2 = \int_{f_1}^{f_2} S_\phi(f) df \quad , \tag{2.17}$$

where ϕ_{jitter} refers to the phase jitter and (f_1, f_2) defines the frequency range for integration. It is usually difficult to measure the spectral density at small frequency offsets with respect to the carrier using standard RF spectrum analyzers. Also, the effect from the phase noise components at very high frequency offsets may be negligible. Such considerations along with others that are specific to the application can determine the frequency range. One common frequency range in used in optical communication experiments is (100 Hz, 10

24
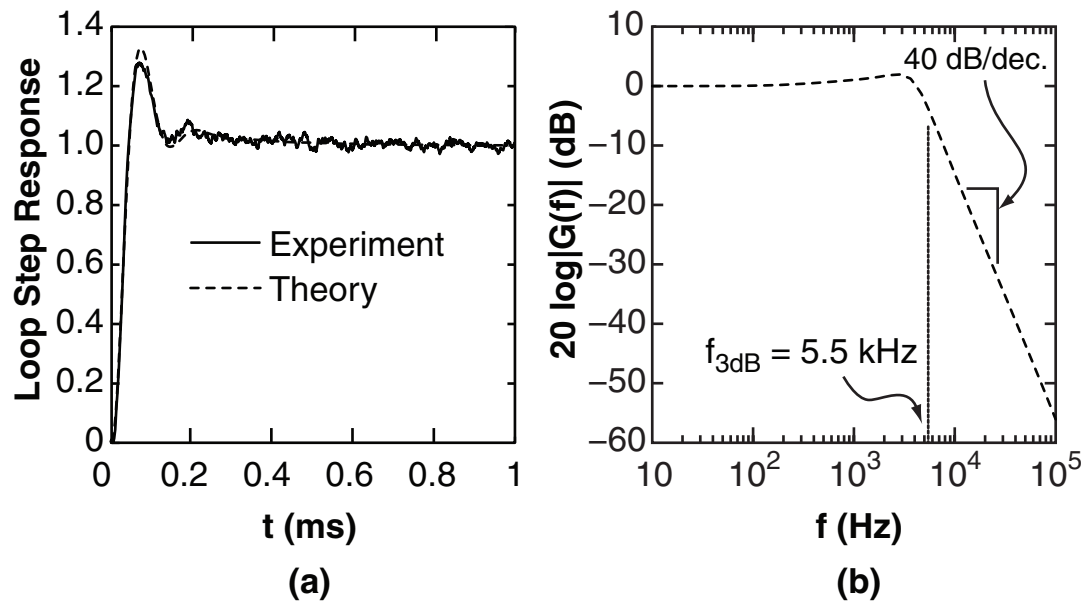
Fig. 2.8: (a) Measured and theoretically-predicted step-response of the phase-locked loop clock recovery system. The system exhibits a rise time below 0.20 ms. (b) The corresponding closed-loop spectral response of the phase-locked loop, showing a bandwidth of 5.5 kHz.

MHz). The timing jitter is simply defined as:

$$\sigma_t = \frac{\phi_{\text{jitter}}}{2\pi f_0} \quad , \tag{2.18}$$

where f_0 is the carrier frequency.

Fig. 2.9 plots the electrical spectrum and single-sideband phase noise of the recovered clock in comparison to the original clock used in the transmitter. Integrating the phase noise pedestal from 100 Hz to 10 MHz yields a timing jitter of 110 fs for the recovered clock, compared to 170 fs of the transmitter clock. In this system, the recovered clock exhibits less phase noise than the original clock because the VCO used in the clock recovery system is less noisy than the RF synthesizer used in the transmitter.

2.3.2   Bit-Error-Rate Measurements

The clock recovery system was also evaluated using bit-error-rate measurements. As depicted in Fig. 2.10, the data was demultiplexed from 80 to 40 Gb/s using an electroabsorption modulator, driven by a 40 GHz signal derived from the clock recovery system. The clock recovery system requires a prescribed input power to operate, which makes it difficult to perform conventional BER vs. power measurements. To avoid this problem we instead maintained a fixed input power and adjusted the optical signal-to-noise ratio (OSNR) by injecting broadband amplified spontaneous emission prior to the clock recovery and receiver. Instead of BER, we measure the Q-factor which is related to the BER. In a binary system
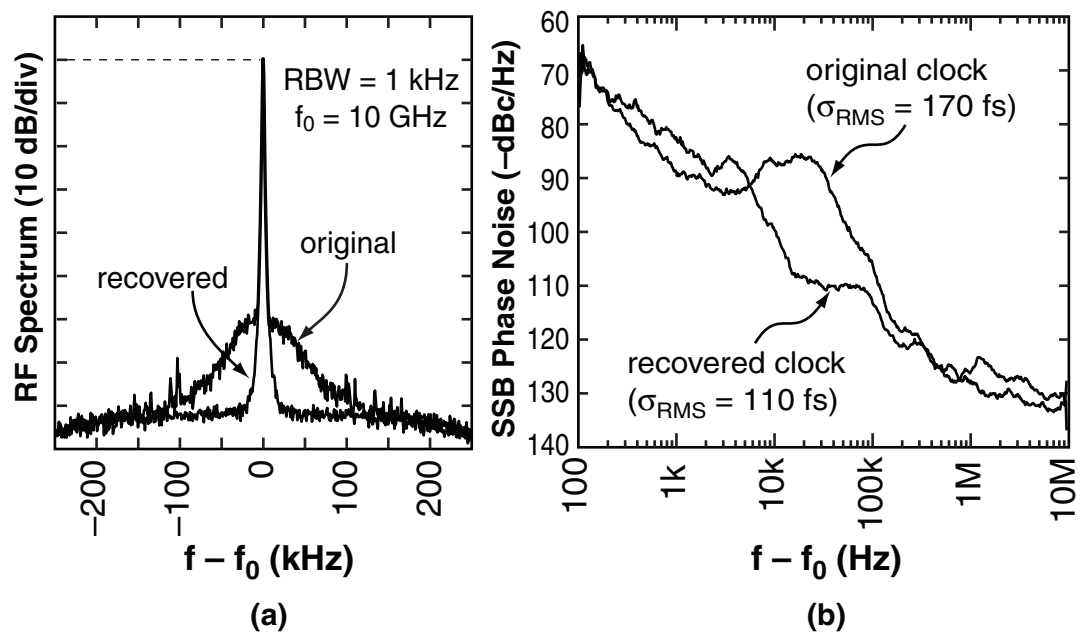
Fig. 2.9: (a) Measured RF spectrum and (b) single-sideband phase noise of the recovered 10 GHz electrical clock, compared to the original clock used in the transmitter.
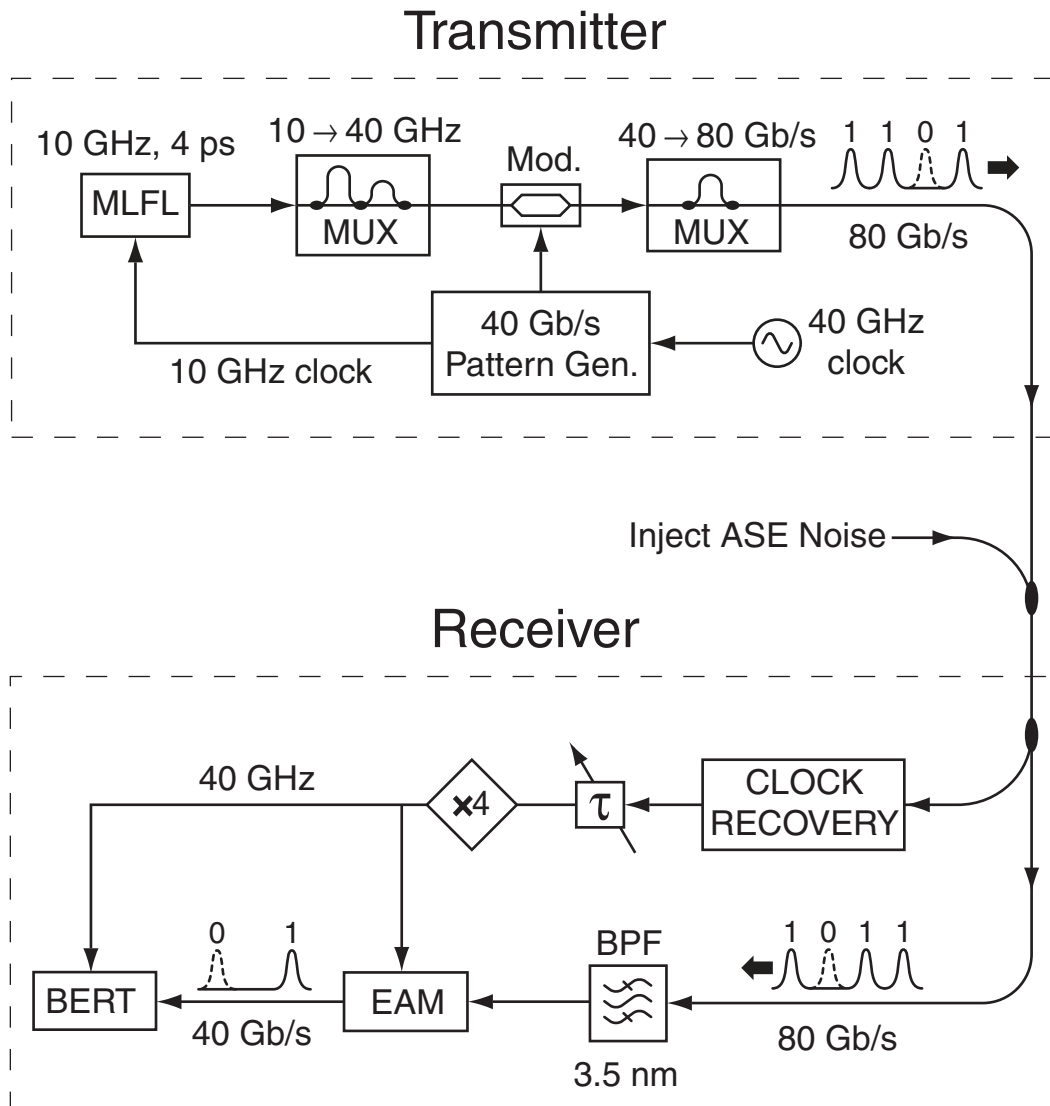
Fig. 2.10: Diagram of 80 Gb/s optical transmitter, demultiplexer, and receiver used to characterize the clock recovery system. Instead of varying the received optical power, the optical signal-to-noise ratio was adjusted by injecting broadband optical noise prior to the receiver.

where the mean values of marks (ones) and spaces (zeros) are represented by μ_1 and μ_0 respectively, one can define the Q-factor as:

$$Q = \frac{|\mu_1 - \mu_0|}{\sigma_1 + \sigma_0} \quad , \tag{2.19}$$

where σ_1 and σ_0 are the standard deviations for ones and zeros respectively. The standard deviations show the noise level on each data rail. In such a system, the BER can be written in terms of these parameters and the decision level D assuming a Gaussian model for the noise:

$$BER(D) = \frac{1}{4}\left[\mathrm{erfc}\left(\frac{|\mu_1 - \mathrm{D}|}{\sqrt{2}\sigma_1}\right) + \mathrm{erfc}\left(\frac{|\mu_0 - \mathrm{D}|}{\sqrt{2}\sigma_0}\right)\right] \quad , \tag{2.20}$$

where $\mathrm{erfc}(x)$ is a form of complementary error function given by:

$$\mathrm{erfc}(x) = \frac{2}{\sqrt{\pi}} \int_x^\infty e^{-\beta^2} d\beta \tag{2.21}$$

The Q-value was determined by measuring the BER as a function of the decision threshold, as depicted in Fig. 2.11(a) for one Q-value. By fitting the erfc function to the measured data, we estimate the value of Q based on Eqs. 2.19 and 2.20 as explained in [53]. Fig. 2.11(b) plots the measured Q-value as a function of the OSNR for back-to-back transmission using both the recovered clock and the original clock. The OSNR is defined as the ratio of optical signal power to the noise power in 0.1 nm bandwidth. There is no significant difference between the two curves, which shows that there is no performance penalty associated with the clock recovery system.
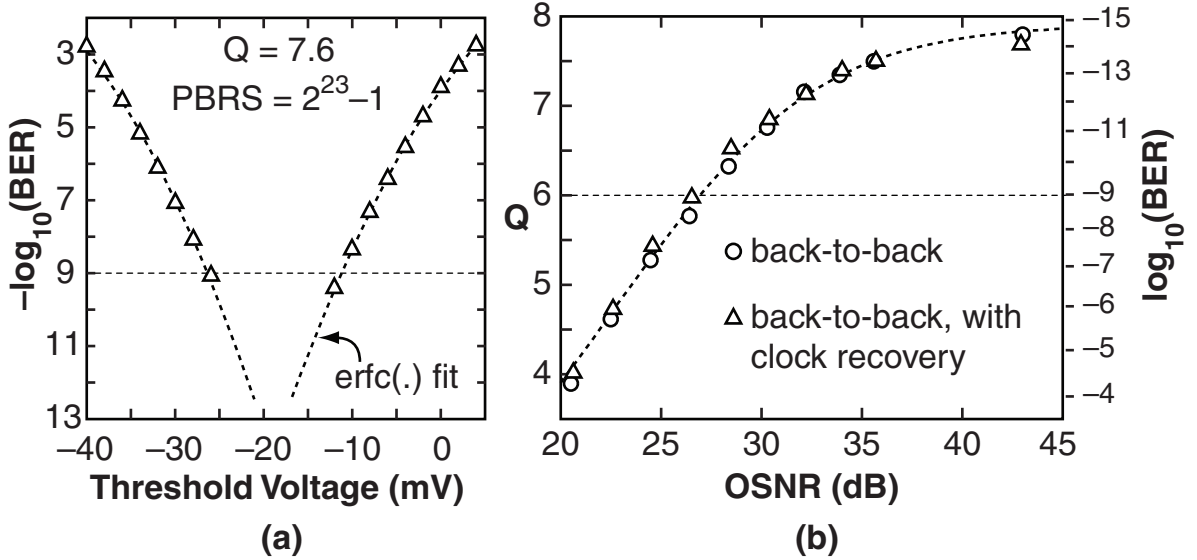
Fig. 2.11: (a) Measured bit-error-rate vs. decision threshold for the case when $Q = 7.6$. (b) Measured back-to-back Q vs. OSNR for the system depicted in Fig. 2.10, with and without clock recovery, showing no appreciable penalty.

2.4 Polarization Dependence in Clock Recovery

In order to look closely at the polarization dependence issue in the clock recovery system, we first have to understand how the two-photon absorption process behaves as a function of the light polarization state. This can be studied both for a single optical input and also cross-correlation between two optical pulses. The polarization dependence issue in TPA process has been experimentally [54–56] and theoretically [57,58] investigated in different materials. To the best of our knowledge, none of these studies considers silicon as the non-linear material. Furthermore, these studies have not considered a two-input system that in designed to generate the cross-correlation between two optical pulses. In this section we

first investigate the polarization dependence of TPA with respect to one continuous wave optical input. Then we consider the case of two optical inputs in a cross-correlation experiment. Using the theoretical and experimental results we find a guideline for minimizing the polarization dependence in the cross-correlation signal. Next, we get back to the clock recovery experiment and investigate the effect of polarization fluctuations on the system.

2.4.1   *Polarization Dependence of the Two-Photon Absorption Process in a Silicon*

Photodiode

Under the assumption that two-photon absorption in silicon is isotropic, the photocurrent generated through TPA can be modelled by the following simple relation:

$$i_{\text{TPA}} \propto \left\langle |\mathbf{E}(t)|^4 \right\rangle, \tag{2.22}$$

where $\langle \cdot \rangle$ indicates the time-average and $\mathbf{E}(t)$ is the real-valued electric field vector of the light. In Appendix B we discuss a more general treatment of TPA polarization dependence in the case that the material has some anisotropy. We show that in an isotropic material the formulas simplify to Eq. 2.22. If the optical signal is a continuous-wave (CW) signal with power P, Eq. 2.22 predicts that the photocurrent is given by:

$$i_{\text{TPA}} = \eta \left(1 - \frac{S_3^2}{3} \right) P^2, \tag{2.23}$$
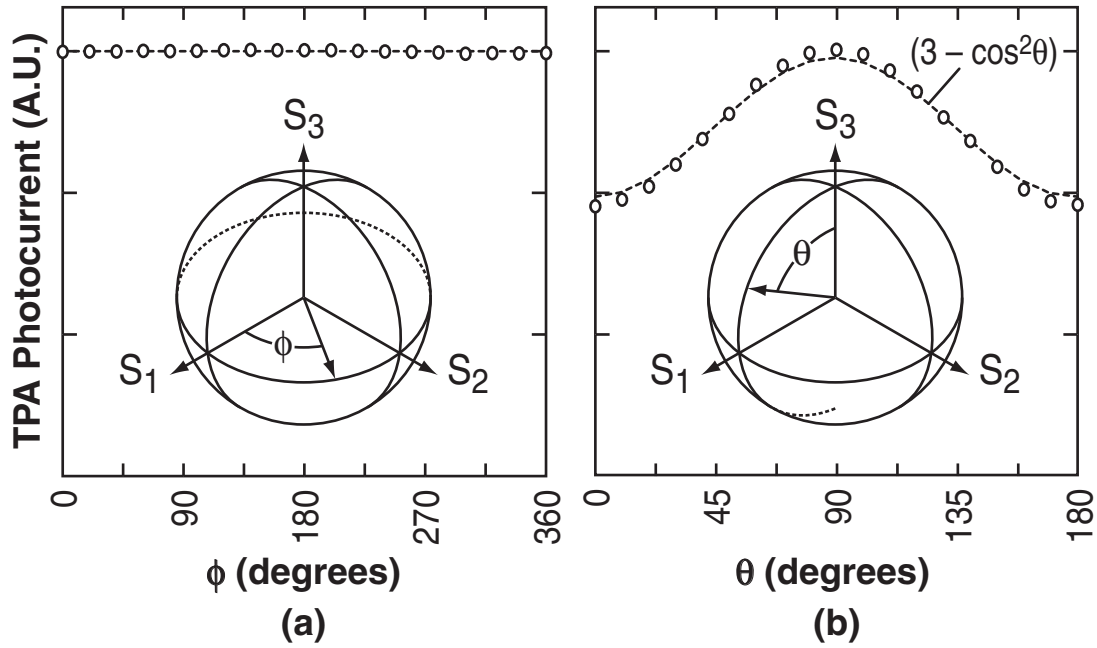
Fig. 2.12: Measured photocurrent produced by two-photon absorption as a function of the polarization state. (a) The photocurrent produced by two-photon absorption is the same for all linear polarization states. (b) When the polarization state changes from linear to circular, the photocurrent decreases by a factor of approximately $2/3$.

where η is an efficiency factor for the process, and (S_1, S_2, S_3) are the normalized Stokes parameters describing the polarization state, i.e., the coordinates on the Poincaré sphere. Eq. 2.23 predicts that for a given power P, the amount of two-photon absorption depends only on the degree of ellipticity of the polarization state, described by S_3. This equation predicts that the TPA photocurrent for circularly polarized light is $\frac{2}{3}$ that of linearly polarized light. The similar factor has been described in [59] for the nonlinear refractive index in isotropic media.

Fig. 2.12 plots the measured TPA photocurrent as a function of the input polarization

state when the power is fixed. While the photocurrent is the same for all linear polarization states, it decreases by a factor of $2/3$ for circular polarization states. This 2:3 circular-to-linear ratio is theoretically expected for isotropic $\chi^{(3)}$ nonlinear processes. The dashed lines plotted in Fig. 2.12 were calculated using Eq. 2.23, and show excellent agreement with our experimental measurements.

2.4.2   Polarization Dependence of Cross-Correlation Signal Measured by TPA

The analysis of the polarization dependence is more complicated if there are two optical signals with different wavelengths and polarization states as shown in Fig. 2.13 [60]. We assume that the difference between the optical carrier frequencies is higher than the speed of the electrical detector, so that the optical beating between the two signals is not observed. The detector is also not fast enough to resolve the individual pulses in either optical input. Despite the limited speed of the detector, the time-averaged photocurrent depends on the relative delay (τ) between the two inputs. For example, if we use square pulses for both optical signals, the resulting cross-correlation function should have a triangular shape as shown in Fig. 2.13. The average output photocurrent, $i(\tau)$, consists of the intensity cross-correlation function $C(\tau)$ on top of a uniform background level B:

$$i(\tau) = B + C(\tau). \tag{2.24}$$
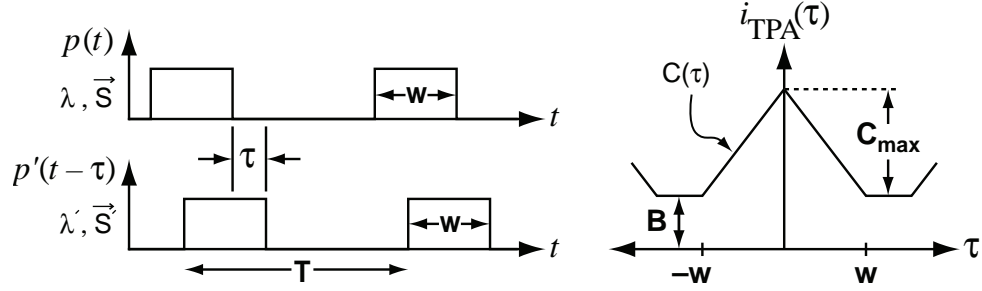
Fig. 2.13: Cross-correlation between two optical pulses generated by two-photon absorption. The cross-correlation ($C(\tau)$) is on top of a constant background level (B).

In general, both the background B and the cross-correlation $C(\tau)$ depend upon the polarization states and powers in the two optical signals. When the simple model given in Eq. 2.22 is applied to the case of two optical signals, we find after some calculation that

$$B = \eta \left[\langle p^2(t) \rangle \left(1 - \frac{S_3^2}{3} \right) + \langle p'^2(t) \rangle \left(1 - \frac{S_3'^2}{3} \right) \right] \tag{2.25}$$

$$C(\tau) = \frac{8\eta}{3} \langle p(t - \tau)p'(t) \rangle \left(1 + \frac{1}{2}S_1 S_1' + \frac{1}{2}S_2 S_2' \right) \tag{2.26}$$

where $p(t)$ and $p'(t)$ are the power envelopes of the two optical signals (as shown in Fig. 2.13), and $\mathbf{S}$ and $\mathbf{S}'$ describe their corresponding normalized Stokes vectors.

In many applications that require cross-correlation between two optical signals including the clock recovery system, one optical signal (clock in the case of clock recovery) is generated locally and can therefore have a prescribed polarization state. On the other hand the second optical signal (data in the case of clock recovery) has an arbitrary polarization

34
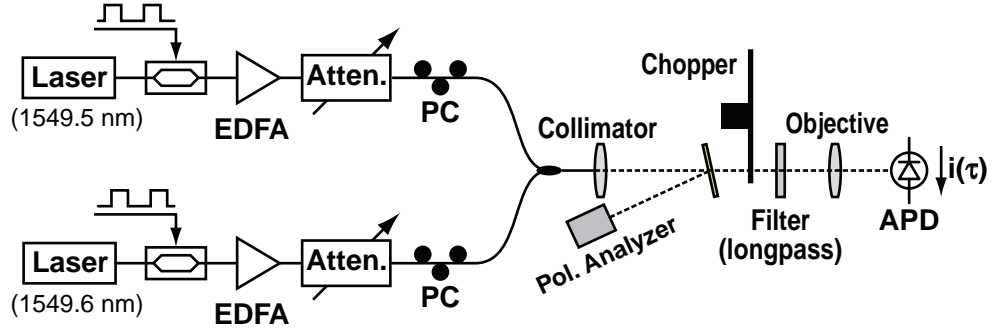
Fig. 2.14: Setup used for investigating polarization dependence of two-photon absorption when used to measure cross-correlation between two optical pulses.

state. Since the polarization state of the second optical signal (**S**) is difficult to control or predict in practice, it is desirable to have a cross-correlation measurement that is independent of the polarization state of this signal. One important observation that follows from Eq. 2.26 is that by fixing **S** to circular state , i.e., setting $S_1 = S_2 = 0$, the cross-correlation component $C(\tau)$ becomes independent of $\mathbf{S}'$, the polarization state of the second signal. Under this condition, Eqs. 2.25-2.26 simplify to:

$$B = \eta \left[\frac{2}{3} \left\langle p^2(t) \right\rangle + \left(1 - \frac{S_3^2}{3} \right) \left\langle p'^2(t) \right\rangle \right] \tag{2.27}$$

$$C(\tau) = \frac{8\eta}{3} \left\langle p(t-\tau) p'(t) \right\rangle \tag{2.28}$$

In order to confirm this theoretical result, we performed experimental measurements using the setup shown in Fig. 2.14. Each of the two signals was generated using a tunable laser and chirp-free (X-cut Lithium Niobate) electrooptic modulator, driven by a programmable

35

pulse generator. The resulting rectangular pulses had a duration of 300 ns, peak power of 8 mW (measured at the detector) and a repetition rate of 1 MHz. The relative delay τ was varied electrically. A long-pass filter was used to reduce the effects of ambient light. The beam was focused to a spotsize of approximately 3.5 μm (FWHM) onto the surface of a silicon APD (EG&G C30902E). We used a chopper and lock-in amplifier to improve the signal-to-noise ratio, but it is also possible to directly measure the nonlinear photocurrent on an oscilloscope. The removable near-normal incidence mirror redirects the beam to a polarization analyzer, which allowed us to control and monitor the polarization state of each input signal prior to the measurement by adjusting the fiber polarization controllers.

Fig. 2.15 plot the measured cross-correlation using the setup shown in Fig. 2.14. As shown in Fig. 2.15 (a), when one of the signals has a fixed linear polarization, the cross-correlation magnitude C varies by a factor of about $3\times$, with the largest correlation occurring for co-polarized linear states and the smallest correlation occurring for orthogonally-polarized linear states. Fig. 2.15 (b) shows that when one of the signals instead has a fixed circular polarization, the cross-correlation signal is invariant to the second polarization state, and the background level changes by only 25%. These results agree with the simple theory presented above. For the more general case when the uncontrolled polarization state is elliptical, we have confirmed that the cross-correlation curve falls between the two extremes plotted in Fig. 2.15 (b), and that variations in the polarization state cause only the background level to change. It is important to note that by using the circular polarization state for the clock signal we sacrifice part of the efficiency.
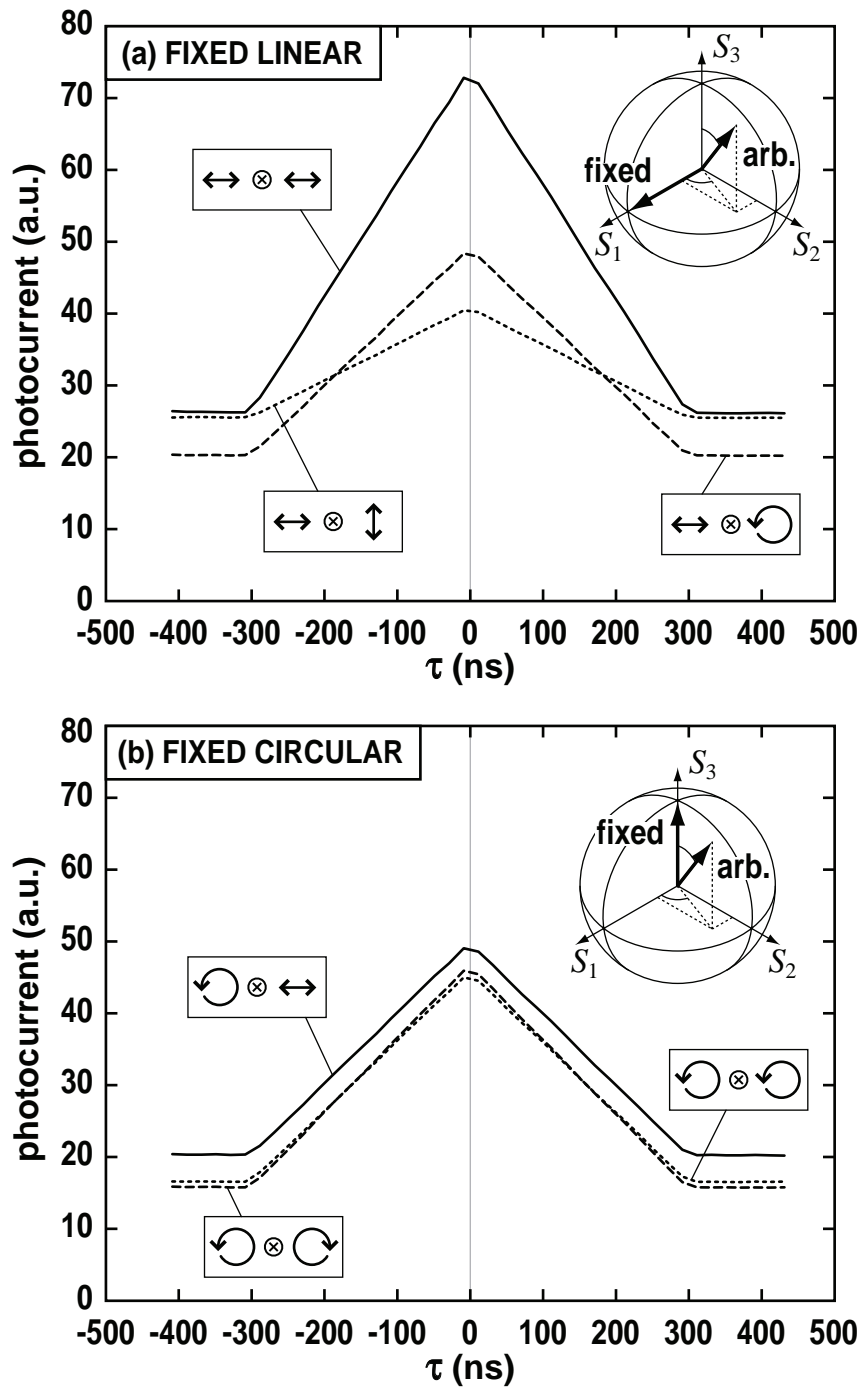
Fig. 2.15: Measured cross-correlation functions (a) when the fixed input polarization state is linear and (b) when the the fixed polarization state is circular.

This is a significant result for developing the clock recovery system or any other system that relies on cross-correlation. We use this concept in order to minimize the effect of polarization fluctuations on the clock recovery system. A similar effect is predicted for other third-order processes in isotropic media. For example, four-wave mixing in fiber becomes polarization-independent when one of the input signals is circularly polarized. [61].

2.4.3 Effect of Polarization Fluctuations on the Optical Clock Recovery

For clock recovery, we are interested in the case where two optical pulses (data and clock) generate a cross-correlation signal in the detector, as shown schematically in Fig. 2.16(a). This is very similar to the cross-correlation measurement performed in Section 2.4.2. One difference is that data and clock pulses have different shape and therefore the cross-correlation function will have a different form. The other difference is that the data signal is a random digital signal meaning that the bits can be one or zero with equal probabilities. Also, in subharmonic clock recovery, the data rate is a multiple of the clock repetition rate as shown in Fig. 2.16.

TPA photocurrent will again consist of two components: constant background level (B) and cross-correlation ($C(\tau)$). B and $C(\tau)$ follow the formulas give in Eqs. 2.25-2.28. Note that $C(\tau)$ does not necessarily go to zero at some delay τ.

As mentioned before, when the clock is circularly polarized, changes in the data polar-
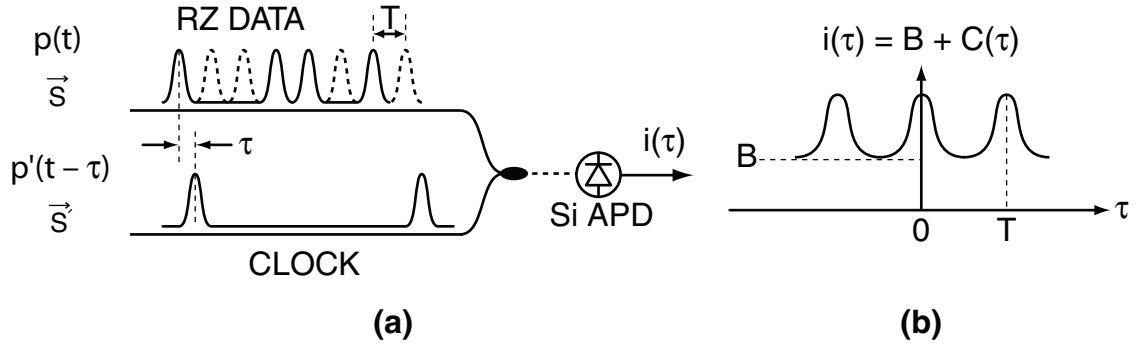
Fig. 2.16: Schematic of cross-correlation measurement produced by two-photon absorption. (a) Two optical signals are combined and directed to the silicon detector. (b) The time-averaged photocurrent $\langle i(\tau) \rangle$ is comprised of a cross-correlation signal $C(\tau)$ on top of a constant background level B.

ization state produce only a shift in the background level while leaving the cross-correlation signal unchanged. We exploited this polarization insensitivity in achieving the results shown in Figs. 2.9-2.11. Unfortunately, even with a circularly-polarized clock signal, the background level B can vary with the data polarization, as described by Eq. 2.28. This variation ΔB can be seen in Fig. 2.17, which plots the measured cross-correlation between the clock and data when the phase-locked loop is deactivated. The two curves in Fig. 2.17 show the maximum shift in the background level that can be obtained by adjusting the data polarization state, while maintaining a circular state for the clock.

As shown in Fig. 2.17, after a fixed offset is subtracted, the cross-correlation signal exhibits a zero-crossing for any input polarization state. This ensures that the clock recovery system can acquire and maintain lock regardless of the data polarization; a prediction that we have verified experimentally. This condition will be maintained provided the max-
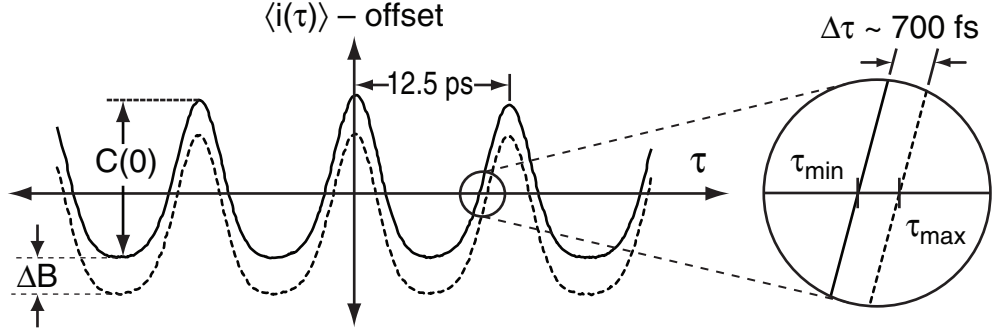
Fig. 2.17: Measured minimum and maximum cross-correlation signals obtained by adjusting the data polarization, when the clock is circularly polarized. Changes in the polarization state produce a change ΔB in the background level, which can shift the zero-crossing point by as much as 700 fs.

imum change in the background level does not exceed the peak-to-peak amplitude of the cross-correlation signal, i.e., $\Delta B < C(0)$.

The ratio $\Delta B/C_0$ can be estimated using Eqs. 2.27–2.28. For simplicity, we assume that the clock and data are comprised of Gaussian pulses with pulsewidths of T and T', and that the pulses are sufficiently short that the cross-correlation function $C(\tau)$ goes almost to zero at the point of minimum overlap. We also assume equally likely marks and spaces and on-off keying modulation. Under this condition we obtain:

$$\frac{\Delta B}{C_0} = \frac{\langle p'^2(t) \rangle}{4 \langle p(t)p'(t) \rangle} = \frac{1}{4}\sqrt{\frac{T^2 + T'^2}{2T'^2}} \left(\frac{P'_{\text{avg}}}{P_{\text{avg}}} \right), \qquad (2.29)$$

where P_{avg} and P'_{avg} represent the time-averaged powers of the clock and data respectively, and the data power is averaged over a random sequence of equally likely ones and zeros. Eq. 2.29 holds for all data rates, and also applies when the data rate is a multiple of the

40
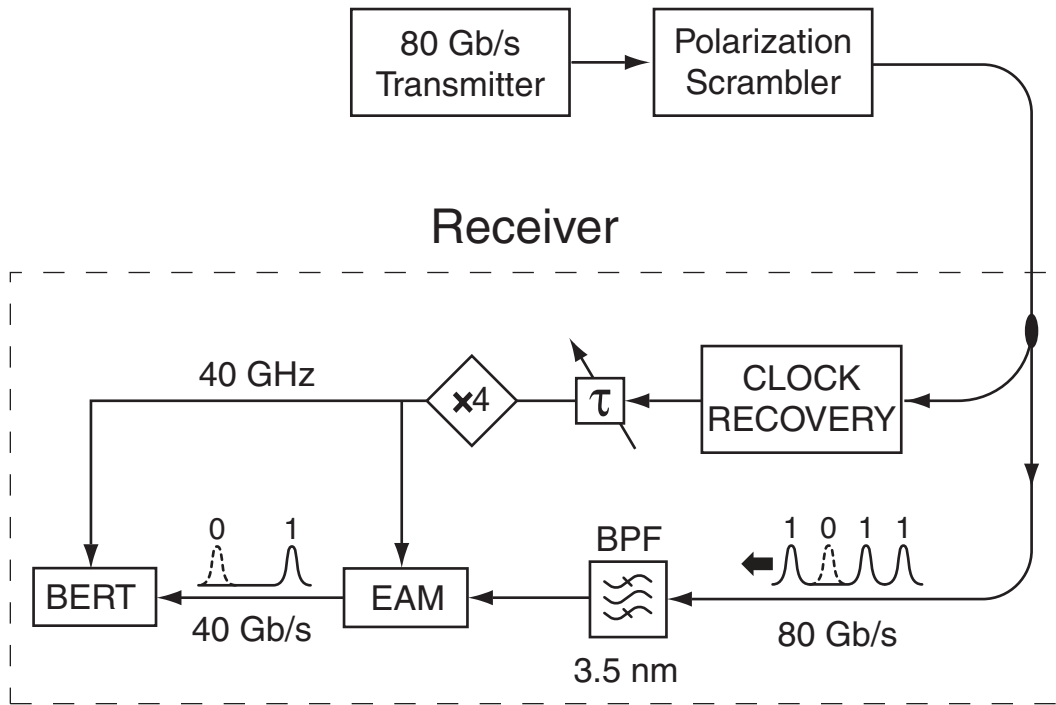
Fig. 2.18: Experimental setup used to investigate the effect of polarization fluctuations on the clock recovery system.

clock frequency.

Eq. 2.29 reveals that once the data and clock pulsewidths are known, the ratio $\Delta B/C(0)$ depends only on the ratio of the average powers. One can therefore minimize the sensitivity to polarization fluctuations by choosing the clock to be circularly polarized with average power much larger than the data. Unfortunately, this choice also causes the signal amplitude $C(0)$ to become much smaller than the total background level B, which degrades the signal-to-noise ratio in the avalanche photodiode. For the experiments reported here, we compromised by choosing the clock power to be twice as high as the data power.
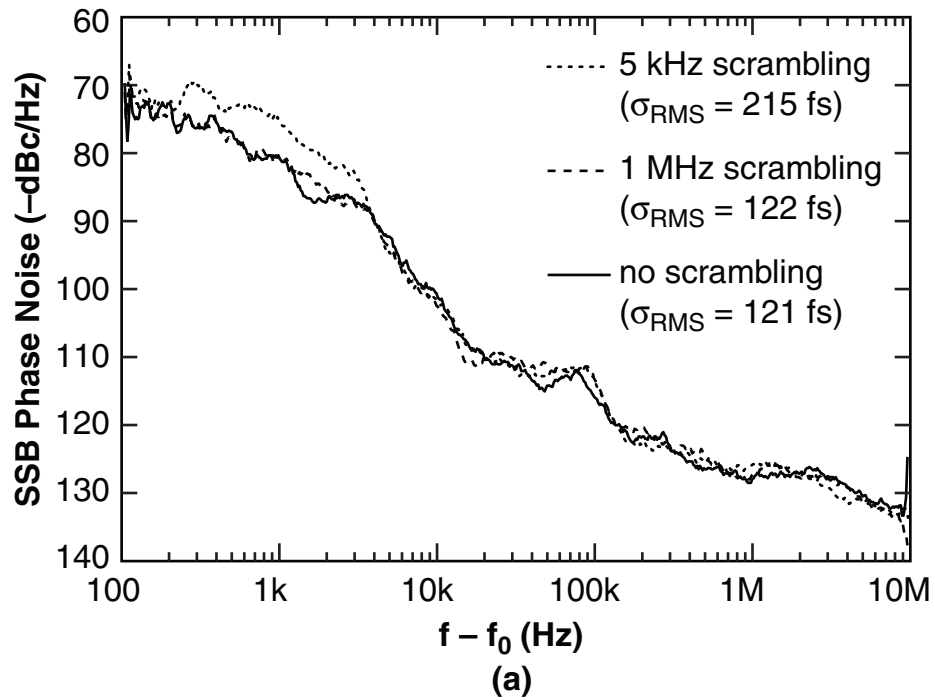
Fig. 2.19: Measured single-sideband phase noise of the recovered clock, when the data polarization state is scrambled at two different speeds. When the polarization fluctuations are within the PLL bandwidth, the timing jitter increases as a result of polarization-induced timing fluctuations.

As shown in Fig. 2.17, when the data polarization changes, the position of the zero-crossing can vary by up to 700 fs, which produces a corresponding shift in the timing of the recovered clock. In order to study the effect of polarization-induced timing fluctuations, we inserted a variable-speed polarization scrambler prior to the receiver as depicted in Fig. 2.18. The electro-absorption modulator used in the demultiplexer is polarization-independent. Therefore, this experiment demonstrated the effect of polarization fluctuations on the clock recovery system. Fig. 2.19 plots the measured phase-noise spectrum of the recovered clock for two different scrambling speeds. When the polarization is scrambled at 1 MHz, we see no significant increase in the phase noise of the recovered clock compared to the un-scrambled system, because in this case the speed of the PLL (5.5 kHz) is not fast enough to track the rapid changes caused by the polarization scrambling. However, when the polarization is scrambled at 1 kHz, the phase noise shows a marked increase at low frequencies, and the timing jitter increases from 121 to 215 fs as a result of low-frequency polarization fluctuations. Assuming that the polarization-induced fluctuations (with σ_{pol} standard deviation) are uncorrelated with the intrinsic clock jitter (with σ_0 standard deviation), we have:

$$\sigma_{\mathrm{pol}}^2 = \sigma_{\mathrm{total}}^2 - \sigma_0^2 \tag{2.30}$$

Using this relationship the timing jitter associated with polarization variations is $\sigma_{\mathrm{pol}} = 180$ fs.

The effect of polarization fluctuations can also be measured by observing the recov-
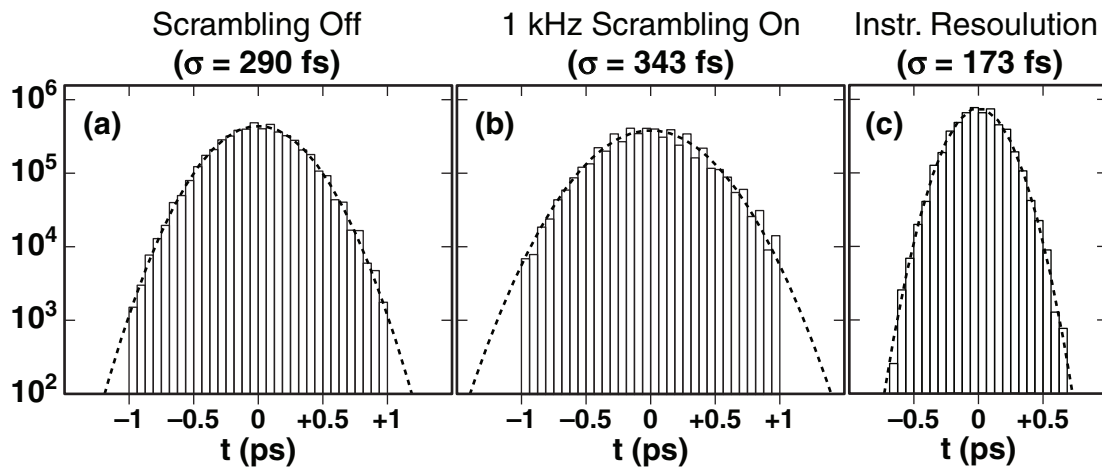
Fig. 2.20: Histograms showing the distribution of the zero-crossing time for the electrical clock when the oscilloscope is triggered with the original clock. Histograms show the results for: (a) without scrambling, (b) with 1 kHz scrambling and (c)intrinsic jitter measured by using the original clock instead of the recovered clock.

ered clock signal on a high-speed sampling oscilloscope, using the original clock signal as a trigger. The histograms shown in Fig. 2.20 (a) and (b) plot the statistical distribution in the timing of the recovered clock, accumulated over approximately 400,000 samples. We used a precision time-base system (Agilent 86107A) to reduce the effect of intrinsic sampling jitter. The RMS timing jitter increases from 285 fs to 340 fs when the polarization scrambling is enabled. These figures are considerably larger than those obtained from phase-noise measurements, in part because of the large intrinsic jitter of the sampling oscilloscope, which was measured to be 170 fs. Fig. 2.20 (c) shows the measurement of this intrinsic jitter associated with the sampling oscilloscope. Despite these limitations, the component of timing jitter due to polarization fluctuations can be calculated by subtracting

44

the variances, which gives 185 fs, in agreement with the independent phase-noise measure-ments. One advantage of using the sampling oscilloscope for jitter measurements is that low frequency (less than 100 Hz) jitter components are also included in this measurement.

As shown in Eq. 2.27, the background photocurrent and zero-crossing point depend only on the degree of ellipticity of the data polarization, which is described by the azimuthal angle θ ($\cos^2(\theta) = S_3''^2$) on the Poincaré sphere. If the cross-correlation is approximated as a linear function of τ in the vicinity of the zero-crossing point, then Eq. 2.28 can be used to derive the following simple relationship between the zero-crossing time and the ellipticity:

$$\tau_z = \tau_{\min} + \Delta\tau \cos^2(\theta), \tag{2.31}$$

where $\Delta\tau$ is the maximum shift in the zero-crossing level. From the data plotted in Fig. 2.17, we infer that $\Delta\tau = 700$ fs.

Fig. 2.21(a) plots the measured distribution of polarization states on the Poincaré sphere when the polarization is scrambled, showing uniform coverage. For a uniform distribution, we can easily see that the probability distribution for the azimuthal angle θ is given by:

$$f_\theta(\theta) = \frac{1}{2}\sin(\theta) \tag{2.32}$$

Using this formula and Eq. 2.31, we can find the probability distribution for the zero-
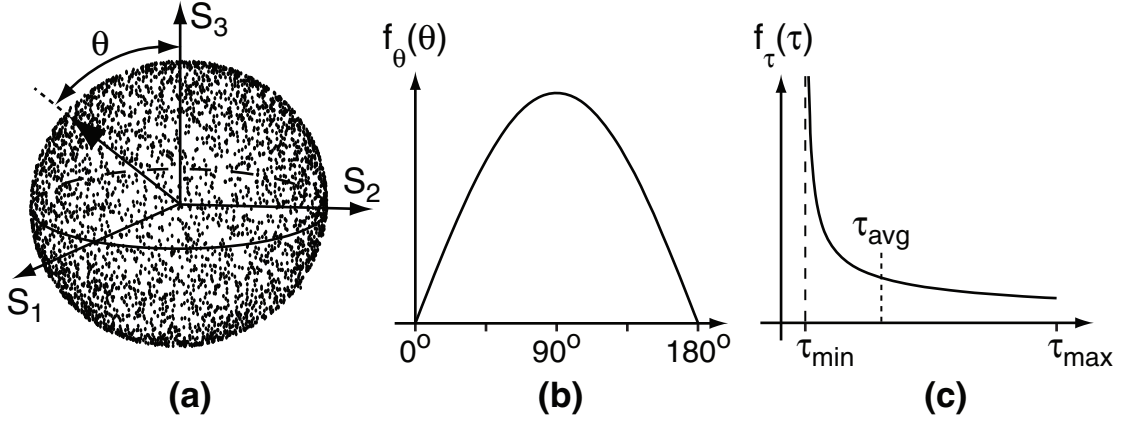
Fig. 2.21: (a) Sampled distribution of polarization states produced by the polarization scrambler, showing uniform coverage of the Poincaré sphere. (b) Calculated probability distribution for the azimuthal angle θ for a point randomly located on the Poincaré sphere. (c) Probability distribution of zero-crossing time, which depends only on the azimuthal angle θ through Eq. 2.31.

crossing point τ;

$$f_\tau(\tau) = \frac{1}{2\sqrt{(\tau_{\max} - \tau_{\min})(\tau - \tau_{\min})}} \tag{2.33}$$

Fig. 2.21(b) plots the predicted distribution of azimuthal angles θ for points uniformly distributed on the Poincaré sphere, and Fig. 2.21(c) plots the corresponding distribution of zero-crossing times, based on Eq. 2.32 and 2.33. Although the polarization states are uniformly distributed over the Poincaré sphere, the distribution of zero-crossing times is highly skewed towards the shorter times. By calculating the variance of this distribution, we predict that the RMS timing jitter associated with slow polarization variations will be

$$\sigma_{\mathrm{pol}} = \frac{2}{3\sqrt{5}}\Delta\tau \simeq 210 \text{ fs.} \tag{2.34}$$

46
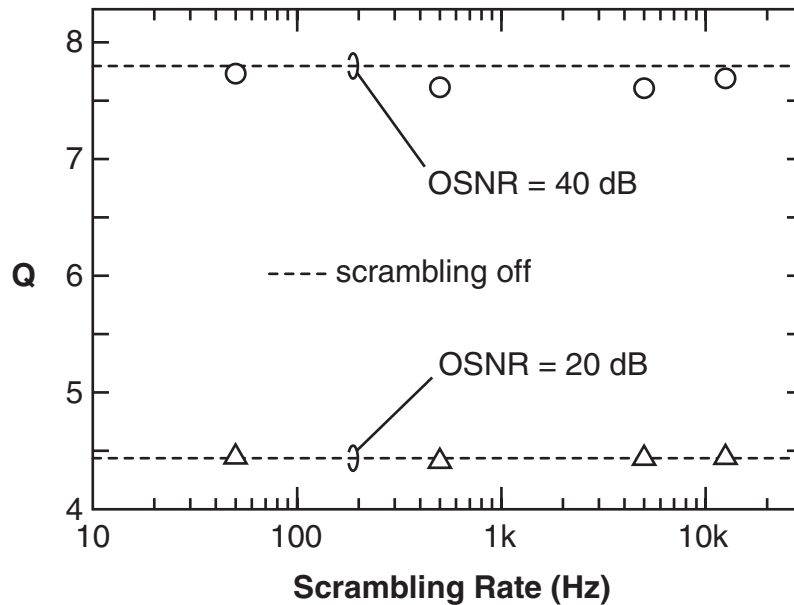
Fig. 2.22: Q as a function of the speed of polarization scrambling, measured at two representative OSNR levels. The dashed line indicates the value of Q obtained without scrambling.

This result agrees approximately with the 180 fs figure inferred from experimental measurements. Furthermore, careful examination of the histogram in Fig. 2.20(b) reveals a slight asymmetry when compared to the symmetric Gaussian curve indicated by the dashed line, which is explained by the skewed distribution described in Fig. 2.21(c).

In order to determine whether the polarization fluctuations lead to any real system impairment, we measured the bit-error-rate as a function of the polarization scrambling rate for two representative OSNR levels. The data points in Fig. 2.22 plot the measured Q-value for four different polarization scrambling rates ranging from 50 Hz to 12 kHz, and the dashed lines indicate the value of Q obtained without polarization scrambling. Each

data point in this plot was computed by making a measurement similar to the one shown Fig. 2.11 (a). Although the Q value depends on the OSNR, we observed no significant change in the bit-error-rate or Q as a result of polarization scrambling.

2.5 Transmission Experiments

At speeds up to 40 Gb/s, there has been a significant effort to conduct laboratory transmission experiments that accurately simulate the polarization effects that occur in deployed fiber systems. In contrast, many of the ground-breaking high-speed optical-time-division multiplexed (OTDM) transmission experiments have implicitly required manual polarization control either after the transmitter or before the receiver [62–65]. One reason for this discrepancy is that many of the optical clock recovery and demultiplexing schemes used at speeds of beyond 40 Gb/s are polarization-dependent and therefore require an established input polarisation state at the receiver. Also, because of the stringent requirement on fiber dispersion, OTDM experiments often use polarization-interleaved multiplexing [64] and sometimes polarization-based demultiplexing to mitigate inter-symbol interference that would otherwise result from uncompensated dispersion. Finally, in order to overcome the effects of PMD and PDL, many high speed systems require that the signal be launched along a principal polarization state of the fiber [65]. In this experiment we use out polarization-independent receiver in order to demonstrate high-speed data transmission without polarization control [66].

Fig. 2.23: Diagram of recirculating loop used to test the clock recovery system in a transmission environment.

2.5.1 Transmission Setup

In previous sections of this chapter we described a high-speed clock recovery system that exhibits very low polarization dependence. But measurements described in the foregoing sections were all conducted with the transmitter and receiver connected back-to-back. In reality, clock recovery is only required when the transmitter and receiver are physically separated. To test the clock recovery system in a transmission environment, we used the recirculating loop configuration shown in Fig. 2.23. The loop uses two acousto-optic modu-

lators to pass one packet of data multiple times through the fiber loop. The resulting output of the recirculating loop system is a stream of data packets that have been passed through the loop an increasing number of times. Therefore a discrete set of transmission distances can be achieved using this method. The transmitter and receiver used in this experiment are identical to the ones shown in Fig. 2.10. The length of the loop is 210 km, which is divided into six identical dispersion maps. Each dispersion map is comprised of 10 km of conventional Corning SMF-28 fiber (D = 17 ps/nm km), 7 km of dispersion-compensating fiber (DCF), followed by an additional 10 km of SMF-28. The DCF was designed to compensate for both the dispersion and dispersion slope of the SMF fiber, and the length of DCF is not included in the propagation distances quoted here. A combination of backward-pumped Raman amplification and conventional EDFAs were used to compensate for fiber losses. The average data power at the beginning of each dispersion map is about 0 dBm.

The signal emerging from the circulating loop consists of discontinuous packets of data that have each been circulating for increasing numbers of round trips. In order for the clock recovery system to operate properly in this configuration, it must quickly acquire lock at the beginning of each packet before bit-error-rate measurements can commence. In this case, the error signal is not always zero and it jumps to a non-zero value any time a discontinuity in the data packet reaches the clock recovery system. In an optical communication system, the amount of time that the clock recovery takes in order to acquire lock and drive the error signal to zero should be much smaller than the length of each packet.

As seen in our measurements shown in Fig. 2.8, the rise time for the phase-locked

50
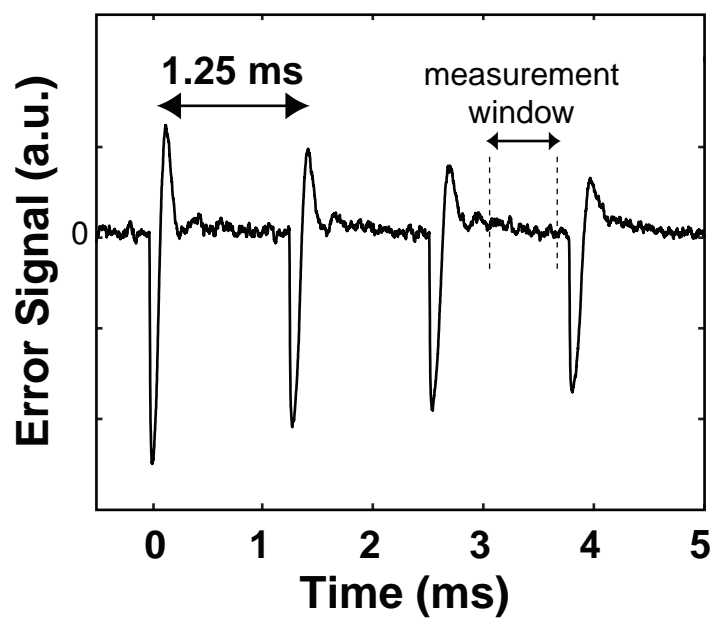
Fig. 2.24: Phase-locked loop error signal when the clock recovery is used in transmission experiment with recirculating loop configuration.

loop is approximately 0.15 ms, whereas the packet length for the 250 km circulating loop is 1.25 ms. Therefore, the clock recovery system can stabilize within the first 20% of each packet, still allowing ample time to conduct bit-error-rate measurements before the next packet arrives. This can be seen by observing the error signal in the clock recovery system as shown in Fig. 2.24. Although the recirculating loop is an artificial way to achieve long propagation distances, even in real networks, the data is sometimes organized into discontinuous packets and the clock recovery system must acquire lock quickly.

Polarization scrambling was employed both prior to and inside of the loop in order to more realistically simulate straight-line performance and prevent spurious performance improvements associated with preferred launch conditions or loop periodicity [67–70]. We emphasize that polarization scrambling is unique to this work and most OTDM transmission measurements do not use scrambling. The signal emerging from the loop was studied using time-gated optical spectrum, autocorrelation, and bit-error-rate measurements.

2.5.2   Transmission Results

Fig. 2.25 shows the optical spectra of the data after 0, 1, 2, 3, and 4 round trips in the loop, measured on a spectrum analyzer with a 2 nm resolution bandwidth. While the spectral shape and bandwidth show very little change after propagation, the background noise level accumulates steadily as a result of accumulated amplified spontaneous emission. After four round-trips (840 km), the ratio of the optical signal power to the noise in a 0.1 nm
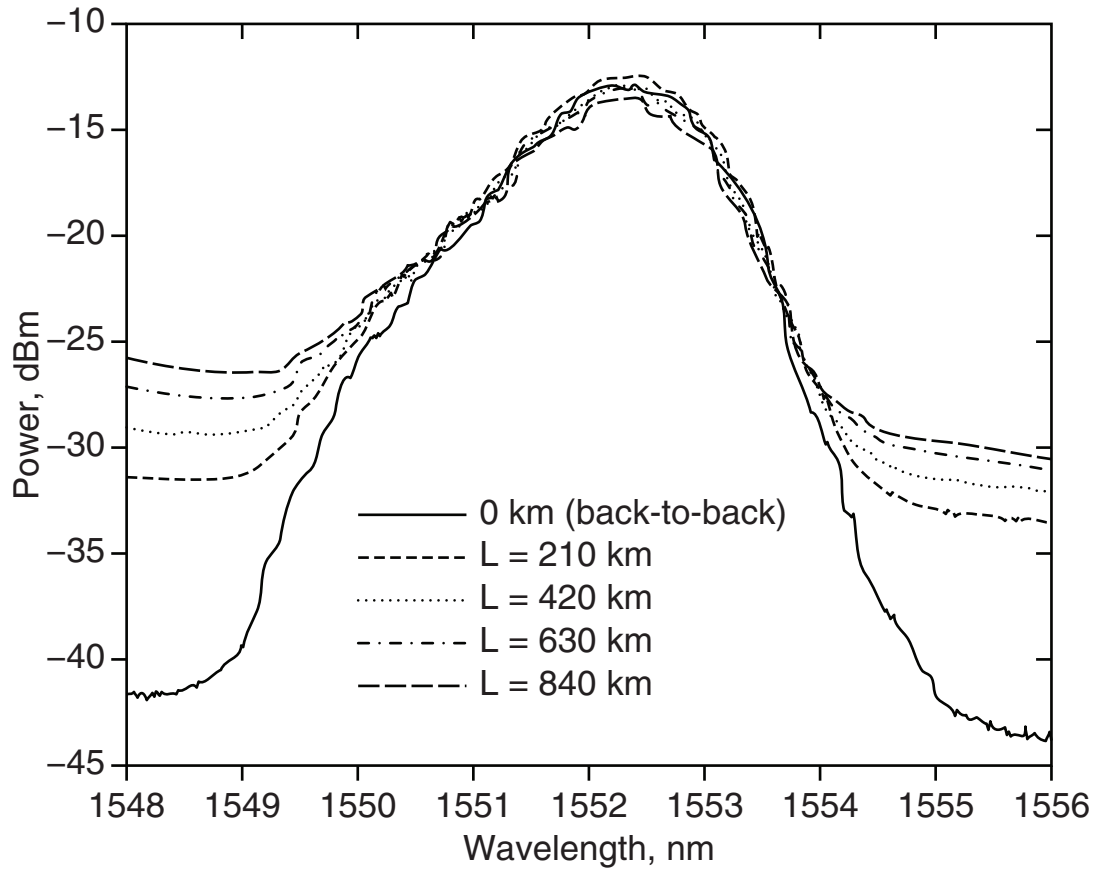
Fig. 2.25: Time-gated optical spectra of received signal after 0, 1, 2, 3, and 4 round trips in circulating loop.

bandwidth was measured to be 27.7 dB. Based upon back-to-back measurements of Q vs. OSNR with noise injection, we predicted that an OSNR level of 27.7 dB should be sufficient for error-free operation, provided there are no additional penalties from dispersion or nonlinearities. Fig. 2.26 (a)-(e) plots the measured autocorrelation traces after 0, 1, 2, 3, and 4 round trips. Although the fiber span was nominally dispersion-compensated, the autocorrelation peak broadens from 4 ps to 5.6 ps over 840 km, as a result of uncompensated dispersion. By adding 100 meters of additional SMF-28 fiber outside of the loop to compensate for this residual dispersion, we obtained the autocorrelation shown in Fig. 3(f), which closely matches the input autocorrelation.

Fig. 2.27 (a) plots the Q-value vs. distance, as determined by measuring the bit-error-rate as a function of the decision threshold. The squares denote the measured Q-value obtained without the additional 100 m of post-compensation fiber. The open circle shows the performance after 840 round trips with the additional post-compensation fiber. To help separate the roles of dispersion and noise in the system, we compared the Q-values observed after propagation to the Q-value obtained in back-to-back measurements with the same OSNR levels. The triangles in Fig. 4(a) plot the back-to-back performance obtained with four-different OSNR levels selected to match the OSNR levels that were experimentally observed after 1, 2, 3, and 4 round-trips. When performing the back-to-back measurements, the OSNR was varied by artificially injecting amplified spontaneous emission noise prior to the receiver. The measurements shown in Fig. 4(a) show that when the dispersion of the system is fully compensated, the performance of the system approaches

54
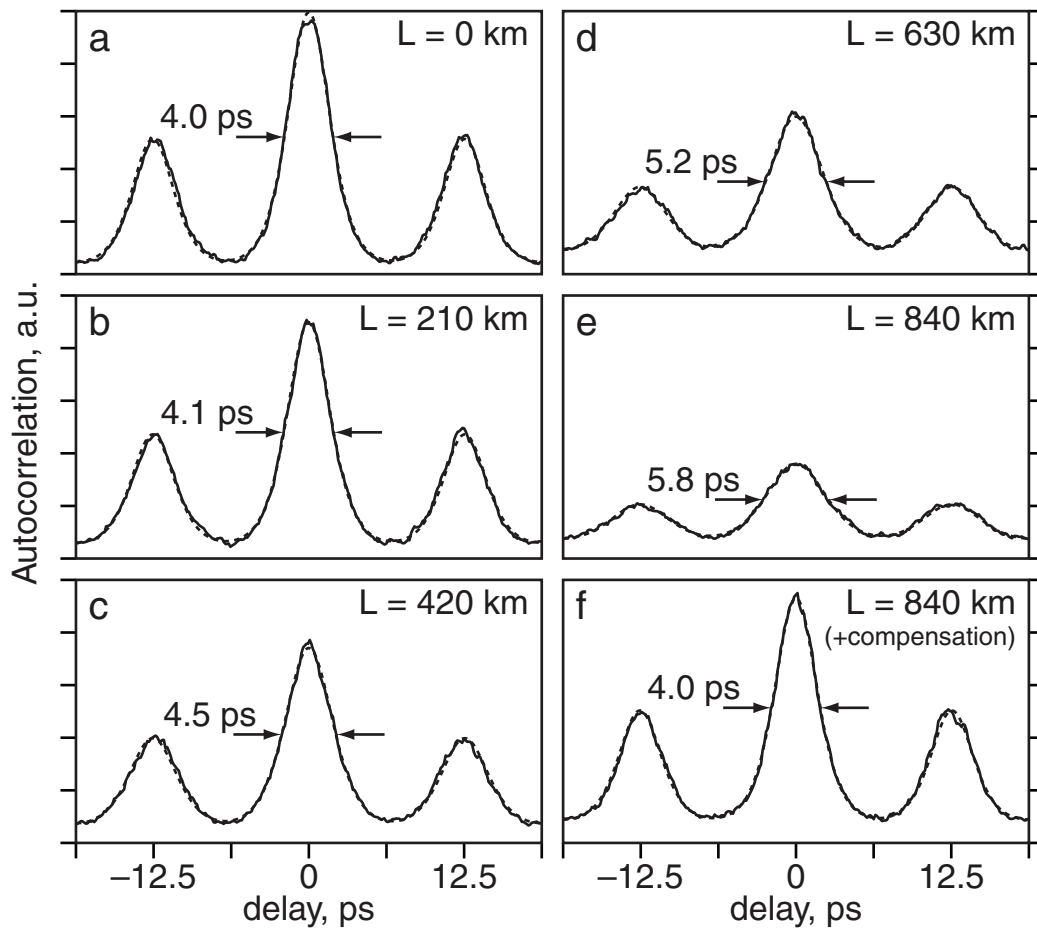
Fig. 2.26: Time-gated autocorrelation measurements of 80 Gbit/s data after 0, 1, 2, 3, and 4 round trips. The final trace shown in (f) depicts the autocorrelation after residual dispersion is compensated by adding 100 meters of additional fiber.
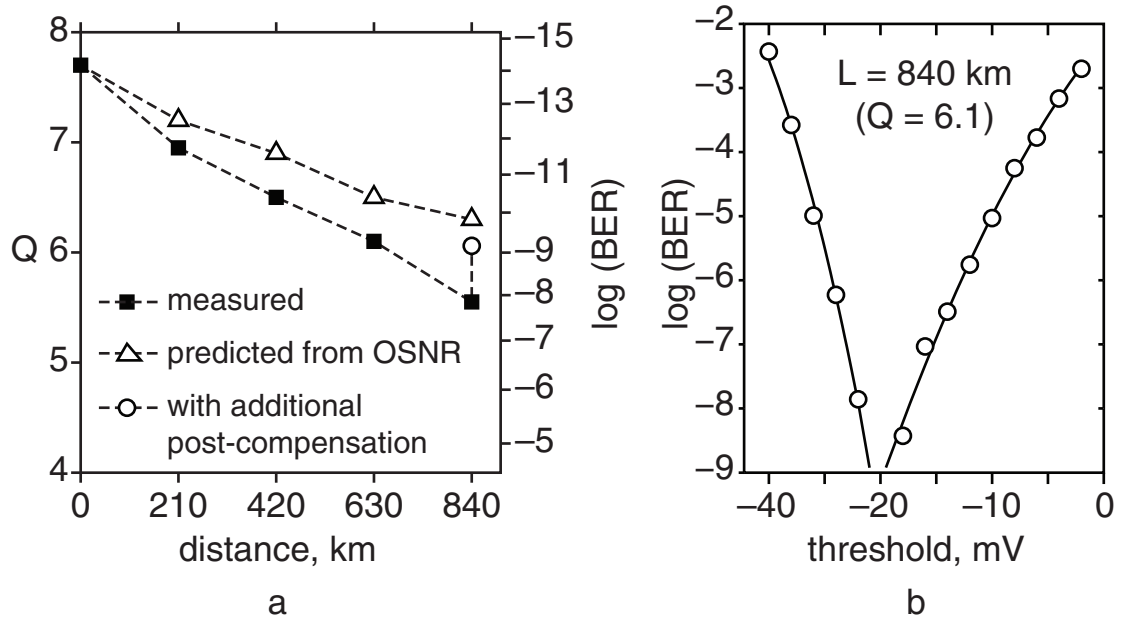
Fig. 2.27: (a) Measured Q vs. distance. (b) Bit-error-rate vs. decision threshold after 840 km transmission, with post-compensation of residual dispersion.

that obtained in back-to-back measurements with the same OSNR, which suggests that in this system the attainable bit-error-rate is limited primarily by accumulated noise. Fig. 4(b) plots the bit-error-rate as a function of threshold voltage after 840 km, confirming error-free operation.

2.6 Dithering Phase Detection

One disadvantage of the clock recovery scheme described here is that the background level depends on the input data power and polarization state. As described in Sec 2.4, in such a system, the ratio between the average powers of clock and data signals should be selected carefully in order to provide low polarization sensitivity. Even when selected properly, variations in the input power levels or ambient light levels in the laboratory can change the background photocurrent which can cause timing jitter or in extreme cases synchronization loss.

One solution to this problem is to generate the bipolar error signal using balanced detectors [14, 17, 71]. This would require two matched silicon detectors with identical avalanche gain, which adds to the cost and complexity of the system. Another approach that can track the peak of the cross-correlation using only one detector is to dither the timing of the clock signal by modulating the phase of the voltage-controlled oscillator [19, 72]. When the resulting cross-correlation signal is mixed with the dithering signal and low-pass filtered, it produces a bipolar error signal that approximates the slope of the original cross-correlation
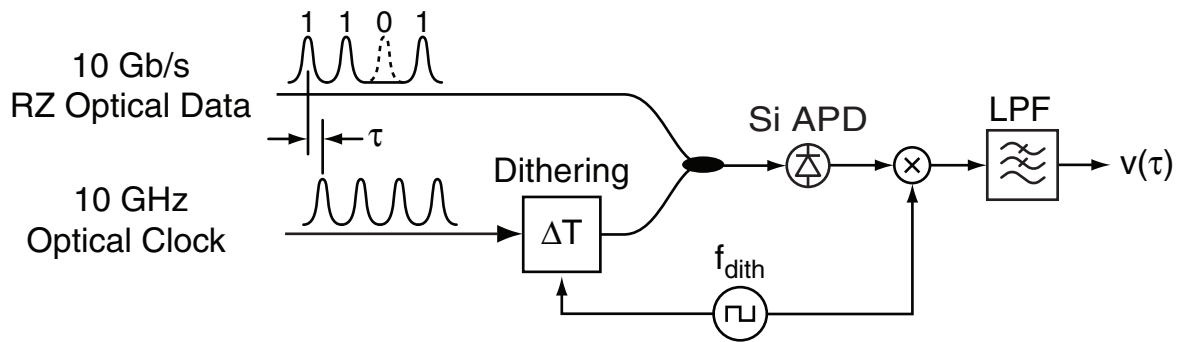
Fig. 2.28: Diagram of dithering clock recovery experiment.

function. The only disadvantage of this technique is that the recovered optical and electri-

cal clocks are dithered and exhibit spectral sidebands at the dither frequency. Because it is

hard to remove these components from the final clock signal, the recovered clock may be

unsuitable for later use in optical regeneration or transmission. An ideal dithering system

should dither the timing of the optical clock in a way that undithered electrical and optical

clock are accessible. Also, the ideal dithering system should not have any moving parts

and should be fast compared to the speed of the phase-locked loop.

To overcome those issues, we have developed an *optical* time-dithering system depicted

in Fig. 2.28. We have tested the optical dithering system at 10 Gb/s as a proof of concept

and we expect the system to operate at higher speeds.

The optical dithering system is comprised of an electro-optic phase modulator followed

by a length of birefringent (PM) fiber, as depicted in Fig. 2.29(a). The clock polarization

is adjusted so that the clock signal entering the phase modulator is linearly polarized at 45

Optical Time Dithering

CLOCK   PC   Phase Mod.   45°   PM fiber   ΔT   PC

f_{dith} = 200 kHz

(a)

Phase Modulator   45°   PM Fiber   PM Fiber   45°   V
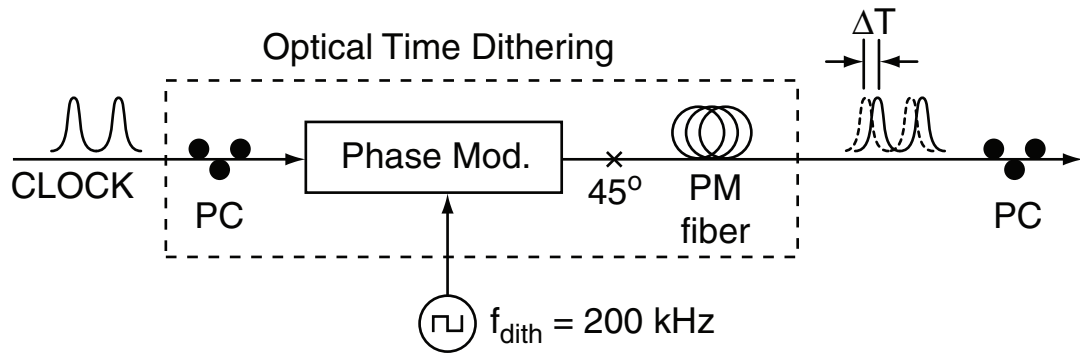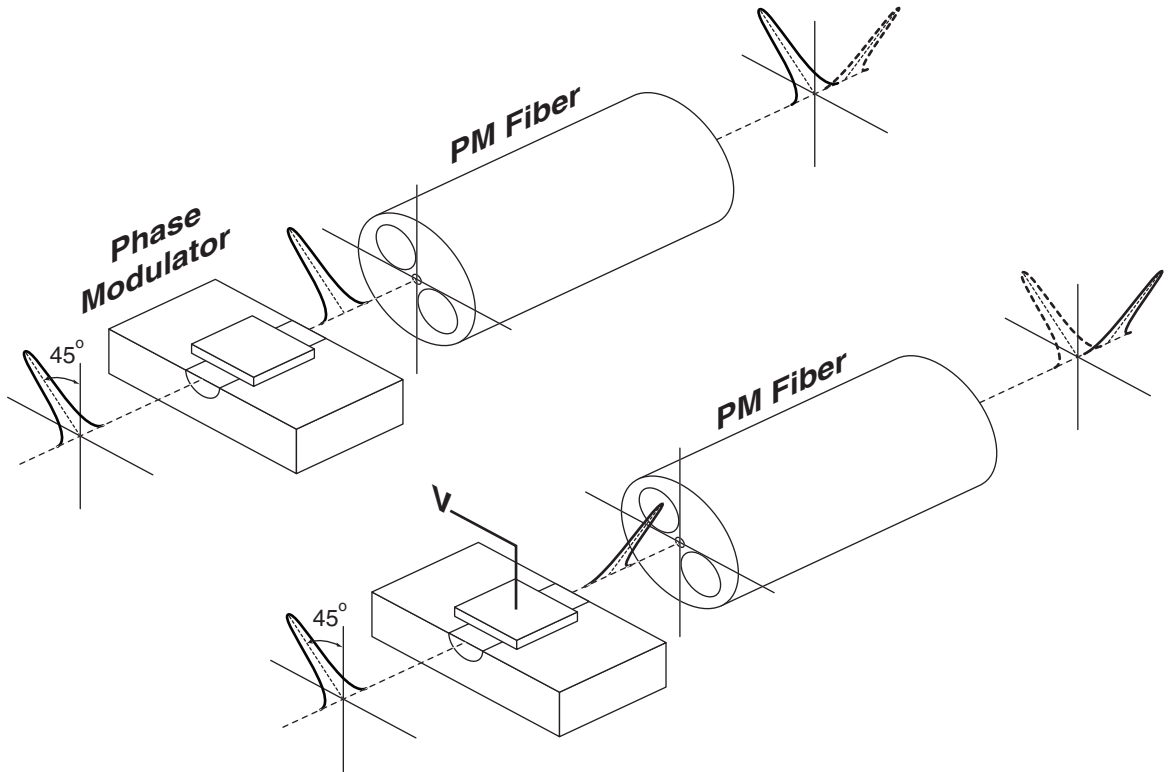
(b)

Fig. 2.29: (a)Simple diagram of the optical dithering system. (b)principle of operation of the optical dithering.

59
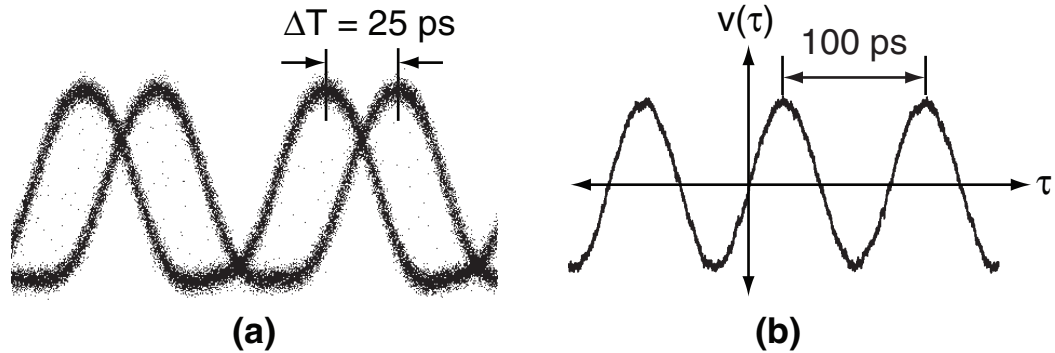
Fig. 2.30: (a) Measured eye diagram of the dithered clock. The dither amplitude of 25 ps is determined by the length of PM fiber. (b) The measured error signal always exhibits a zero-crossing at $\tau = 0$.

degrees to the z-axis of the modulator. The phase modulator is driven with a square wave at frequency $f_{\mathrm{dith}} = 200\mathrm{kHz}$. When the amplitude of the square wave is adjusted properly, the signal emerging from the modulator is periodically switched between two orthogonal polarization states at ± 45 degrees as shown in Fig. 2.29(b). The axes of the PM fiber are also oriented at ± 45 degrees with respect to the modulator, so that the signal entered into the fast and slow axis of the fiber, depending on the applied voltage. The amplitude of the timing dither is then entirely determined by the length and birefringence of the PM fiber. The advantage of this scheme over other dithering approaches is that it allows access to the undithered optical and electrical clock. Another advantage is there are no moving parts in the system and the speed of dithering can be very fast.

Fig. 2.30(a) shows the dithered optical clock measured on a sampling oscilloscope in eye diagram mode. The amount of timing dither is 25 ps which was achieved by using

18 meters of PM fiber. The dithered clock signal alternates between two orthogonal polar-ization states, and by using a manual polarization controller it is possible to convert these two states to right- and left-hand circular polarizations, which is optimal for polarization-insensitive performance, as described in Section 2.4.

After the clock and data signals are combined and focused onto the silicon avalanche photodiode, the resulting photocurrent is mixed with a reference dither signal and low-pass filtered. Fig. 2.30(b) plots the resulting error signal $v(\tau)$, which approximates the deriva-tive of the original cross-correlation signal $C(\tau)$. Unlike the original cross-correlation signal which exhibits a non-zero background, the dithered phase-detection circuit always produces a bipolar error signal $v(\tau)$ which has a zero-crossing when $\tau = 0$, as shown in Fig. 2.30(b).

Fig. 2.31(a) plots the electrical spectrum of the 10 GHz recovered clock obtained with the dithering phase-locked loop. The dithering tones at ± 200 kHz offset frequency can be seen on the spectrum but they are suppressed by 68 dB compared to the carrier. In order to estimate the effect of these sidebands on the RMS timing jitter, we assume that the recovered clock voltage can be written as:

$$V(t) = V_m \cos(\omega t + \phi_m \sin \omega_m t) \quad , \tag{2.35}$$

where ω_m is the dithering frequency and ϕ_m is the amplitude of phase deviation. For calculation simplicity we have assumed a sinusoidal variation in the phase while the real
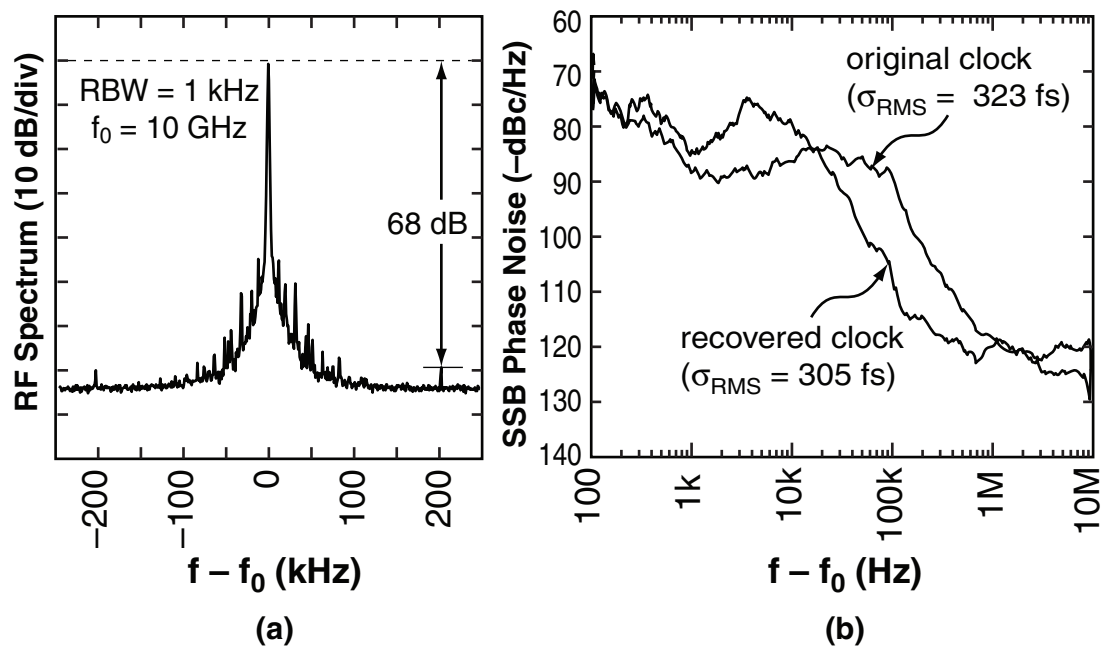
Fig. 2.31: (a) RF spectrum and (b) single-sideband phase noise of the recovered 10 GHz electrical clock. The dither tone at ± 200 kHz is suppressed by 68 dB.

phase variation in this case is closer to square wave. The voltage $V(t)$ can be expanded in the form:

$$V(t) = V_m \sum_{-\infty}^{+\infty} J_n(\phi_m) \cos\left[(\omega + n\omega_m)t\right] \quad , \qquad (2.36)$$

where $J_n(\cdot)$ represents the Bessel function of the first kind. Therefore, the ratio of the power in the first sideband to the carrier power can be found:

$$\frac{P_1}{P_0} = |J_1(\phi_m)|^2 \quad , \qquad (2.37)$$

where P_1 and P_0 are the powers in the first sideband and the carrier respectively. Using this equation we estimate the RMS timing jitter caused by a side band that is 68 dB weaker than the carrier:

$$\sigma_{\mathrm{rms}} = \frac{\phi_m}{\sqrt{2}\omega} \simeq 9 \text{ fs} \qquad (2.38)$$

When we instead produced the same 25 ps timing dither by electrical phase modulation, the sidebands increase to only 8 dB below the carrier as shown in Fig. 2.32. Such strong sidebands will be difficult to remove for later use in the receiver.

Fig. 2.31(b) plots the single-sideband phase-noise of the recovered clock and original transmitter clock. The integrated phase noise from 100 Hz to 1 MHz was 305 fs for the recovered clock, compared to 323 fs for the original clock.

One of the advantages of this system compared to the system based on offset subtraction (explained in Sec. 2.3) is lower polarization sensitivity. As discussed in Sec. 2.4, changes

63
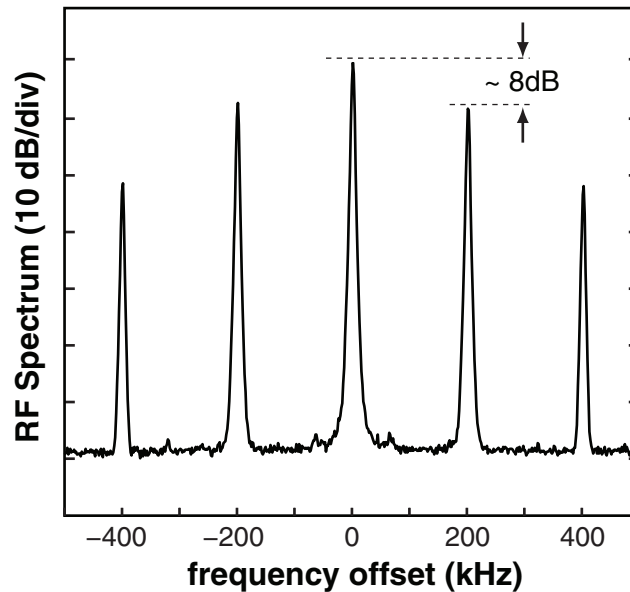
Fig. 2.32: Output RF spectrum when the timing of a signal generator is electrically dithered with a 25 ps peak-to-peak. Sidebands are as high as 8dB below the carrier.

in the data polarization can cause a shift in the background level, which in the conventional system induces a measurable shift in the timing of the recovered clock. The dithering system by contrast does not require the subtraction of an offset signal, and it is therefore expected to perform much better in the presence of polarization or power fluctuations.

This effect is clearly illustrated in Fig. 2.33, which plots the eye diagram of the received data when the the recovered clock signal is used as a trigger. In both cases, the polarization state of the data was randomly varied during the measurement. When the offset-subtraction method is used, we see a significant broadening of the eye as a result of polarization-induced timing fluctuations. By contrast, when the new dithering phase detection is used, the eye diagram remains stable even when the polarization state changes.

64

offset subtraction (no dithering)	with optical time dithering
(a)	**(b)**
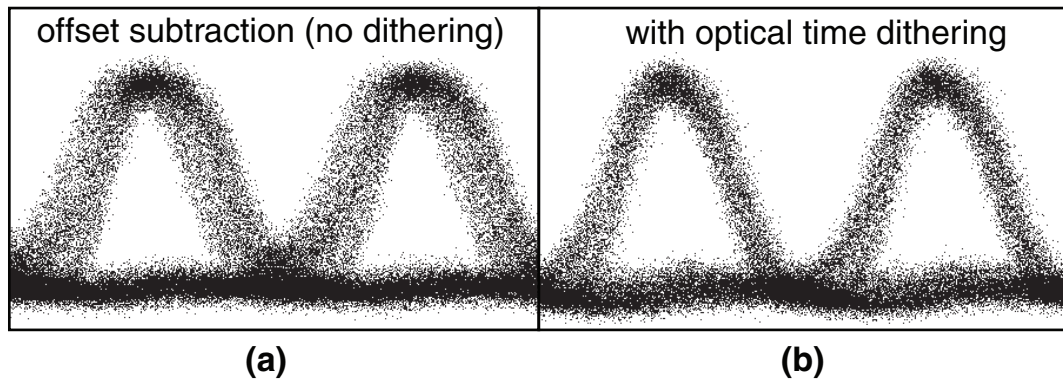
Fig. 2.33: Eye diagram of received 10 Gb/s data, measured while the polarization state is varied. (a) The undithered system exhibits significant polarization-dependent timing, as described in Sec. 2.4. (b) The dithering clock recovery instead locks to the peak of the cross-correlation signal, which reduces the polarization dependence.

The dithering system brings a similar improvement to the dynamic range of the clock recovery system. To quantify this improvement, we varied the power of the data signal while keeping clock average power fixed at 5 mW. The ratio of the data to the clock power was varied from -8 dB to +2dB and the system was able to acquire and maintain lock at all of these power levels. For comparison, the conventional subtraction technique requires adjustment of the offset value whenever the data power changes. Fig. 2.34 (a) plots the timing jitter of the clock recovery system based on dithering as a function of the ratio of data to clock power. The variation of timing jitter as a result of changing data power level is due to the fact that the sensitivity of the PLL phase detector (Appendix A) varies as a function of the optical power. This change in the sensitivity changes the PLL closed-loop transfer function and consequently the amount of phase noise in the output.
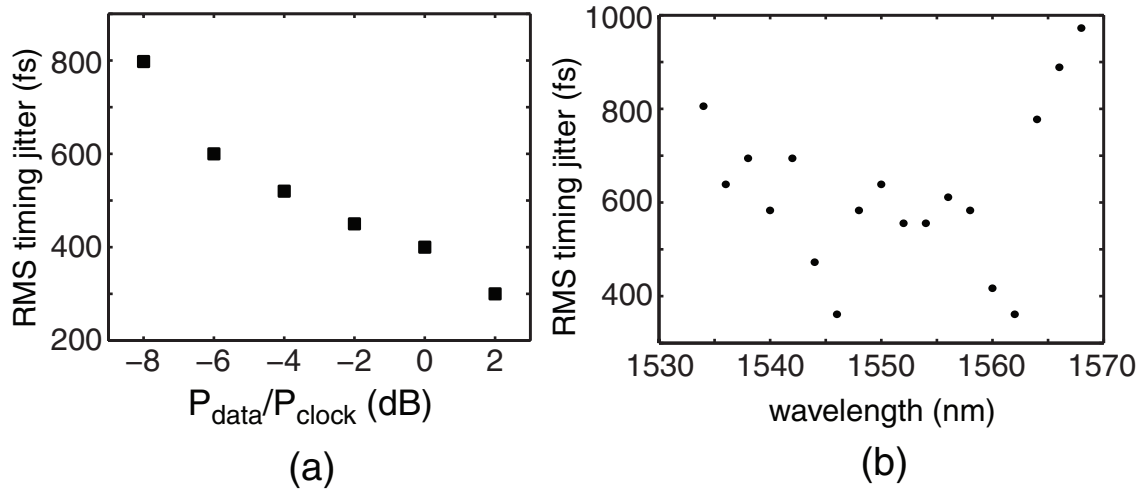
Fig. 2.34: Timing jitter in the clock recovery system based on optical dithering as a function of (a)ratio of data to clock average power and (b) wavelength of data signal.

In the prototype 10 Gb/s system described in this section, the data was produced by externally modulating a tunable CW laser. This allows us to easily investigate the wavelength dependence of the clock recovery system – something that is difficult to explore with mode-locked lasers. We successfully tested the clock recovery system at wavelengths from 1534 nm to 1568 nm, a range limited only by the bandwidth of our EDFAs, and we found that it functioned properly at wavelengths tested. Fig. 2.34 (b) plots the timing jitter in the recovered clock obtained from this system as a function of wavelength. For $\lambda < 1530$ nm and $\lambda > 1570$ nm the power drops out because of the EDFAs used in the experiment. The variation of timing jitter as a function of wavelength is related to the change in photo-detector TPA sensitivity as a function of wavelength. Although in theory the nonlinear absorption coefficient β should not depend strongly on wavelength, the detector used here exhibits sig-

66

nificant wavelength dependence because of the non-optimized antireflection coating. We believe this is due to inefficient antireflection coating on the detector and can be solved by depositing the right antireflection coating. The topic is explained more in Ref. [48].

2.7 Summary

In summary, we have demonstrated a new technique for optical clock recovery based on two-photon absorption in a silicon photodiode. This technique was tested at 80 Gb/s data rate while it is expected to operate at higher speeds. Main advantages of the system include low polarization sensitivity and broad wavelength range over which the system can operate. We investigated the polarization dependence of the TPA in the silicon photodiode. A method for minimizing the polarization dependence was theoretically proposed and experimentally demonstrated. We used this technique in our clock recovery experiment and demonstrated very low polarization sensitivity for the system. Transmission experiments were performed over 840 km of fiber while polarization scrambling was used in the transmission channel. Error-free transmission over this distance was achieved. At the end, we studied an optical dithering system that is shown to reduce the dependence of the clock recovery on data polarization state, power and wavelength. This system was tested at 10 Gb/s but is expected to operate at higher speeds.

3. POLARIZATION-INDEPENDENT OPTICAL DEMULTIPLEXING USING HIGHLY NONLINEAR FIBERS

In Chapter 1 we briefly mentioned techniques that have been used for optical demultiplexing. Most of these techniques utilize a nonlinear process as an optical switching gate that can distinguish between different tributaries in a high-speed data stream. Our focus in this thesis is the fiber-based techniques meaning the methods that use fibers as their nonlinear medium. The development of new fibers with ultra high nonlinearity has sparked a renewed interest in all-optical signal processing using these fibers. One way to realize an optical switch using nonlinear fiber is to use a process called cross-phase modulation (XPM). This process like two-photon absorption is a $\chi^{(3)}$ process. In the case of two-photon absorption, the imaginary part of the $\chi^{(3)}$ tensor causes an absorption in the nonlinear material that depends on the light intensity, whereas in the case of cross-phase modulation, the real part of the $\chi^{(3)}$ tensor causes the refractive index to change in proportion to the light intensity. Therefore, a weak optical signal (probe) can be affected by a strong optical signal (pump). This idea has been used for optical demultiplexing [7, 23, 26]and wavelength conversion [73–75] in nonlinear fibers. One method to observe the effect of the pump on the
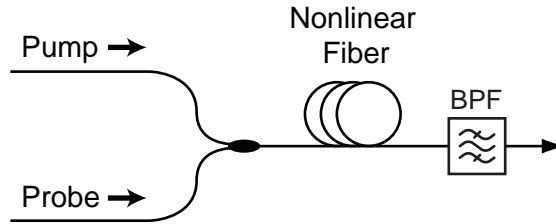
Fig. 3.1: Optical signal processing using cross-phase modulation in nonlinear fiber.

probe is to use an interferometric method to detect the nonlinear phase shift induced in the probe pulse as a result of XPM. The most coomon interferometric configuration is the nonlinear optical loop mirror (NOLM) [23, 75–78]. Another way to detect the effect of the pump over the probe through cross-phase modulation is to monitor the changes in the probe spectrum [7, 26, 73, 74]. Cross-phase modulation between strong pump pulses and weak probe signal causes a broadening in the probe spectrum [79, 80]. Fig. 3.1 depicts a simple diagram that shows how optical switching can be achieved using XPM process in fiber and bandpass filtering [26]. The role of the bandpass filter is to isolate the broadening caused by cross-phase modulation. If the pump is pulsed, this broadening only occurs when the pump pulse in on.

In this thesis we focus on the spectral filtering method shown in Fig. 3.1 for optical demultiplexing. As we mentioned in Chapter 1, XPM process is polarization dependent in general. In the case of demultiplexing we are interested in a system that is independent of probe (data) polarization state while pump (clock) polarization can be fixed. If the pump signal is circularly polarized (similar to the case of TPA), one can show that the

XPM is independent of the probe polarization state. However, it is difficult to maintain circular polarization along the nonlinear fiber. This can be done by twisting the fiber [30] or generating circular birefringence while manufacturing the fiber [29]. While these methods has been shown to work for polarization-insensitive signal processing, they have not been applied to new highly nonlinear fibers. Most highly nonlinear fibers are customized to provide enough nonlinearity over shorter lengths [3] and controlling the birefringence of these fibers during manufacturing often proves difficult, especially with microstructured or photonic crystal fibers. Consequently, a significant amount of linear birefringence can be seen in these fibers as we will discuss during this chapter.

In this chapter we will introduce two new methods for polarization-independent cross-phase modulation in highly nonlinear fibers. These methods can be used in fibers with linear birefringence and do not require maintaining a certain polarization state along the optical fiber. We will explain our methods using two separate experiments on two different nonlinear fibers.

3.1 Polarization-Independent Demultiplexing in 2-m Bismuth-Oxide-Based Fiber

The first fiber we consider is a bismuth-oxide doped silica fiber that is manufactured by Asahi Glass Co [3, 81]. The fiber is designed to provide a high nonlinear parameter (γ). This nonlinear parameter is defined as [82]:

$$\gamma = \frac{2\pi n_2}{\lambda A_{\text{eff}}} \quad ,$$

(3.1)

where λ is the signal wavelength, A_{eff} is the effective area of the fiber core and n_2 is the Kerr nonlinear coefficient. The fiber parameters according to data provided by the company and also from Ref. [3, 81] are listed in the Table 3.1. It is interesting to compare these parameters to the ones of standard single-mode fiber, which are also listed in Table 3.1. Most parameters for the standard fiber are taken from the data sheet for Corning SMF-28. The nonlinear parameter for standard fiber has been measured in [83]. As seen in this comparison, doping silica with bismuth-oxide increases the Kerr nonlinear coefficient by more than $30\times$. Also, the effective area of the bismuth-oxide-based fiber is about $30\times$ smaller than that of the standard fiber. As a result, the nonlinear coefficient γ is $1000\times$ higher for the bismuth-oxide-based fiber. On the other hand, the dispersion and loss for bismuth-oxide-based fiber are much higher than standard fiber. Unlike many other demonstration of optical signal processing that use tens to hundreds of meters of fiber [7, 19], the high nonlinear parameter of this fiber allows for nonlinear processing in much shorter

lengths [3].

The only parameter not provided by the company was the differential group delay (DGD) in the fiber. DGD is defined as the time difference between two optical pulses that are launched along the two principal axes of the fiber.The DGD was measured using the standard interferometric technique explained in [84, 85]. Fig. 3.2 (a) shows the experimental setup used to measure the DGD. The polarization of the CW laser source is adjusted such that it equally excites the two eigenstates of the fiber. When the wavelength of the CW source is scanned, the output light polarization changes periodically with the optical frequency. Using a polarizer at the output this periodic pattern can be measured on a power meter. Fig. 3.2(b) plots the output power as a function of the wavelength. It is easy to show that the period in the frequency domain is given by:

$$\Omega = \frac{2\pi}{\Delta\tau} \quad , \qquad\qquad (3.2)$$

Fiber Parameter	Bismuth-Oxide Fiber	Standard Fiber	Unit
Dispersion (D)	-260	17	ps/nm·km
Loss	3	5×10^{-5}	dB/m
Effective Area (A_{eff})	3	80	μm^2
Kerr Nonlin. Coefficient (n_2)	8.2×10^{-15}	2.2×10^{-16}	cm^2/W
Nonlinear Parameter (γ)	1100	1.1	$\text{W}^{-1}\text{km}^{-1}$

Tab. 3.1: Comparison between parameters of bismuth-oxide-based and standard fibers at 1550 nm wavelength.

(a)

~ 47 nm
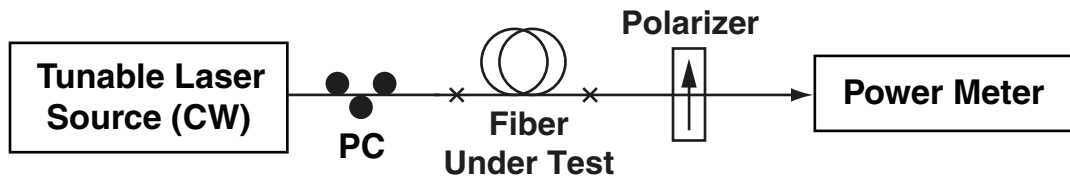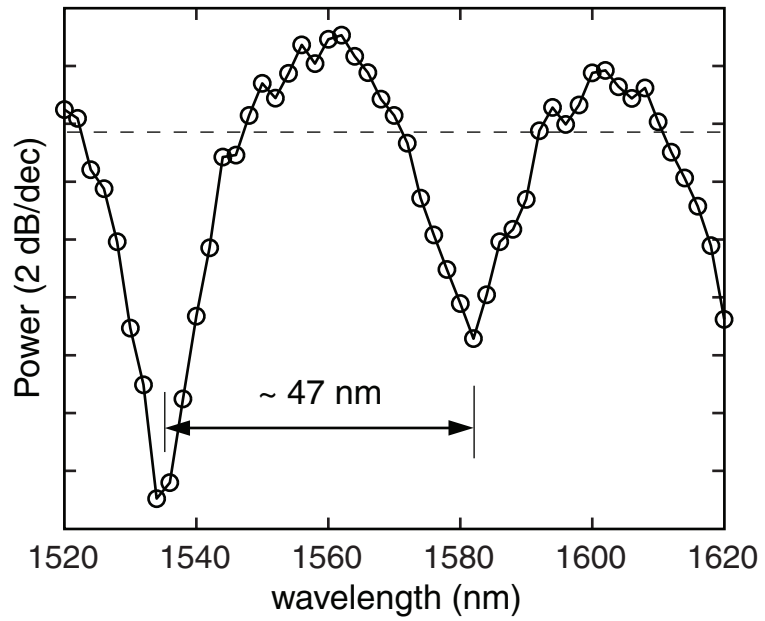
(b)

Fig. 3.2: (a) Setup used to measure the differential group delay in the nonlinear fiber. (b) The measured value for output power as a function of CW wavelength.
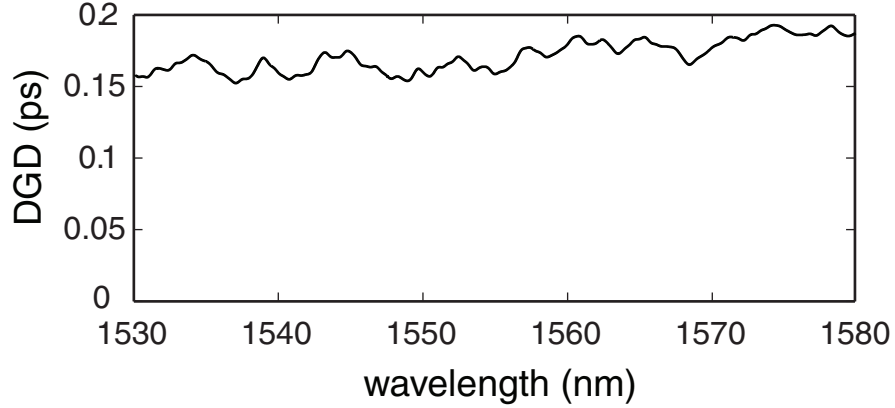
Fig. 3.3: DGD as a function of wavelength as measured by optical vector network analyzer.

where $\Delta\tau$ is the DGD of the fiber. Although the power is not periodic in wavelength domain, we can write an approximate formula for the wavelength spacing between two peaks or two minima:

$$\Lambda = \frac{\lambda_1 \lambda_2}{c\Delta\tau} \quad , \tag{3.3}$$

where λ_1 and λ_2 are the wavelengths at the two peaks or minima. Using this equation and the measurement shown in Fig. 3.2, the DGD of the fiber is estimated to be $\Delta\tau = 0.17$ ps. It is important to note that we are assuming that the fiber principal axes do not rotate within the fiber. This assumption is equivalent to what is called the *short-length regime* in Ref. [85]. Since the length of the fiber is only 2 m, we expect to be in the short-length regime. A method to evaluate the length regime is described in [85]. Based on this method if we draw a horizontal line at the mean output power as shown by the dashed line in Fig. 3.2 (b), the number of mean value crossing should be equal to the total number of minima and

74
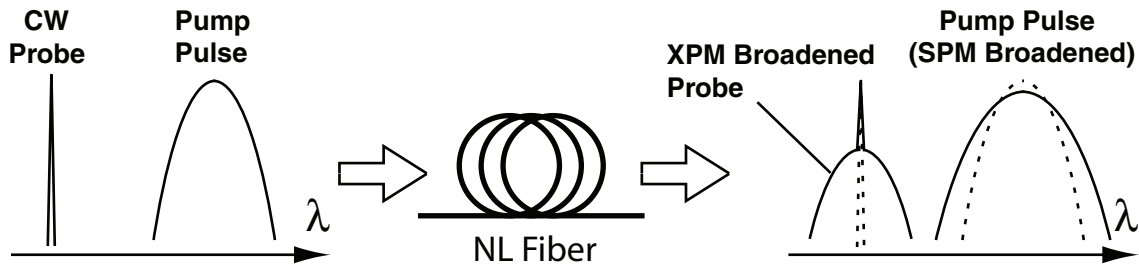
Fig. 3.4: Effect of Kerr nonlinearity in fiber on the pulsed pump and the CW probe inputs.

maxima for the short-length regime. This test shows that we can approximately treat this fiber as a system with fixed principal axes. However, the current measurement is not very accurate because we were able to measure only two periods using this wavelength scanning range.

In order to measure the DGD more accurately, we used an optical vector network analyzer made by Luna Technologies. The principle of operation of this instrument is described in [86]. The measured DGD as a function of wavelength is plotted in Fig. 3.3. As seen in this figure, the value of DGD at 1550 nm is about 0.16 ps which is close to our previous measurement.

3.1.1 Cross-Phase Modulation Experiment with CW Probe

In the signal processing applications discussed here, the signal will be a stream of optical pulses representing high-speed data. However, in order to better investigate the polarization-

75
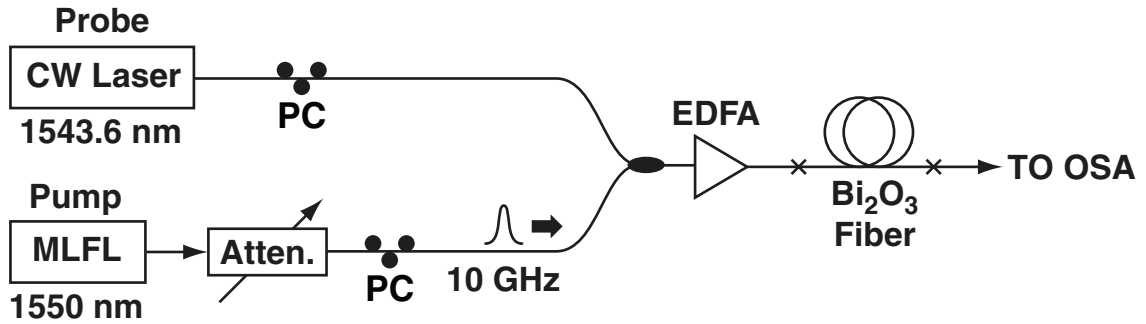
Fig. 3.5: Setup used for investigating the cross-phase modulation process between pulsed pump and CW probe signals.

dependence of cross-phase modulation, we initially replaced the data with a simple continuous wave (CW) tone, as shown in Fig. 3.1. Such an experiment is easier to perform and provides clearer information about the cross-phase modulation process in the fiber. Such a setup can also be used for optical wavelength conversion [73] if the pump signal is on-off modulated with a data pattern. Fig. 3.4 depicts schematically how the pump and CW probe evolve in the presence of nonlinearity. The pulsed pump signal that is much stronger becomes spectrally broadened as a result of self-phase modulation (SPM) [82]. The CW probe signal also acquires a broad pedestal as result of cross-phase modulation. SPM and XPM processes have the same origin which is the Kerr nonlinearity in the fiber. In an ideal fiber with no dispersion both SPM and XPM spectral broadening can be shown to be symmetric as depicted in Fig. 3.4.

Fig. 3.5 shows the experimental setup used to investigate XPM broadening of a CW tone. The pump pulses are generated using a mode-locked fiber laser at 10 GHz rate. A

CW laser source is used as the probe signal which is combined with the pump signal in a 3dB coupler. The coupler is followed by a high-power EDFA which is connected to the nonlinear fiber. The FWHM pulse-width the pump pulses is 2.7 ps the average power of the pump pulse can be controlled using the variable attenuator. The wavelength separation between the pump and probe is about 7.5 nm. This wavelength separation can not exceed the maximum amount allowed by the walk-off caused by the dispersion in the 2m fiber. It is desirable to separate pump and probe signals in wavelength but the group delay walk-off causes the nonlinear interaction to become inefficient for large separations. For the fiber discussed here and 7.5 nm wavelength separation, we estimate the maximum walk-off to be about 2 ps.

Fig. 3.6 (a) plots the measured spectrum of the light coming out of the nonlinear fiber. The broad pedestal around the CW probe is caused by cross-phase modulation by the strong pump pulses. Fig. 3.6 (b) plots maximum and minimum XPM pedestals obtained by adjusting the CW polarization. At least 3dB variation in the XPM level is seen even if the pump polarization is optimized. We will show in the next section that by carefully controlling the pump power level, the shape of XPM spectrum changes which can dramatically affect the polarization dependence.
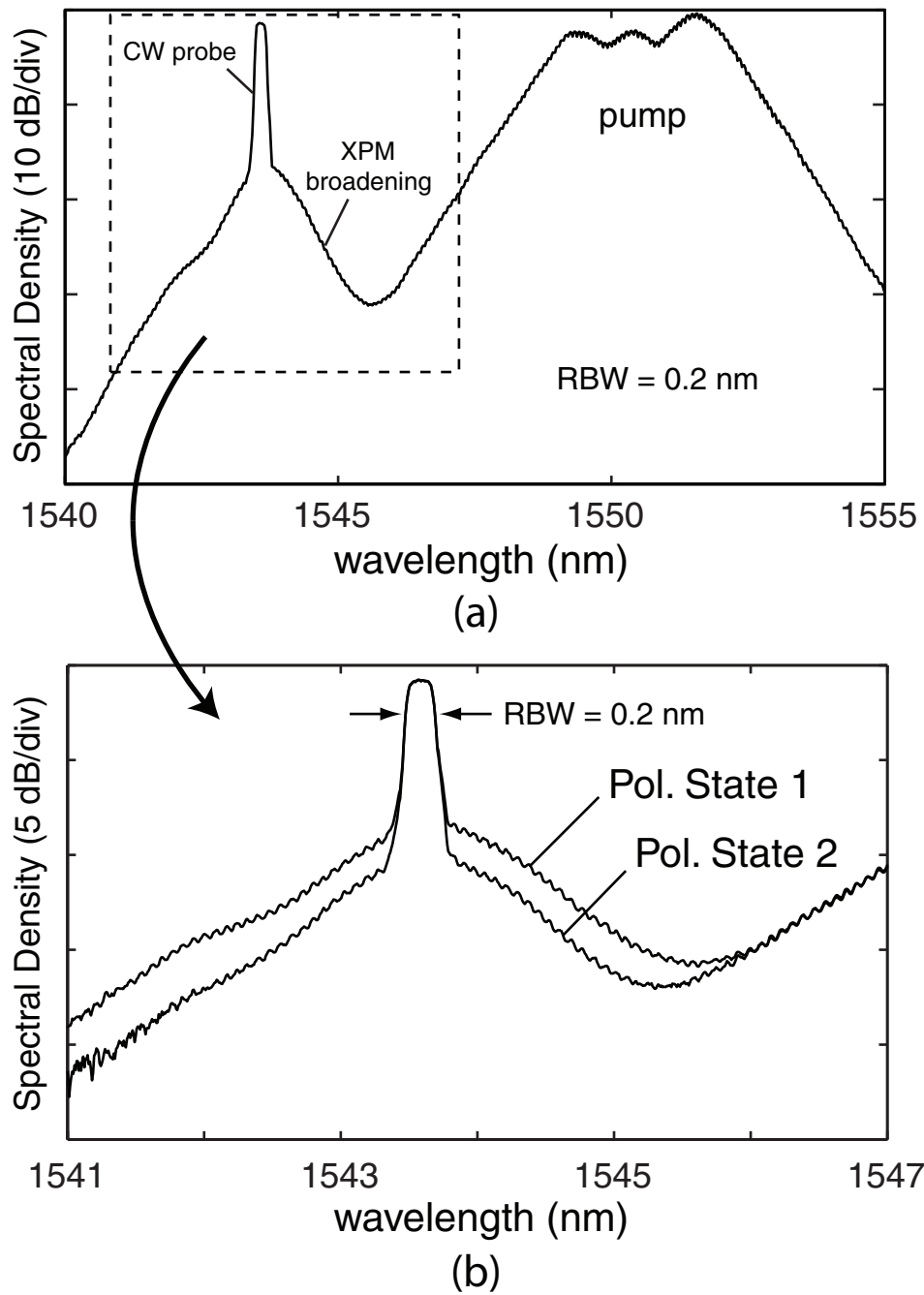
Fig. 3.6: (a) CW probe and pulsed pump spectra at the output of the nonlinear fiber and (b) Magnified XPM pedestal for two extreme probe polarization states.

3.1.2   Polarization-Independent Cross-Phase Modulation

Fig. 3.6 (b) shows the XPM pedestal for two extreme probe polarization states. As we see in this figure, changing the probe polarization state causes the XPM pedestal to simply shift up or down. In other words the polarization state affects the XPM spectral efficiency similarly for all frequencies. This does not have to be the case as we will show in this section. By increasing the pump power level, the simple shape of the XPM pedestal starts to change. Fig. 3.7(a)-(d) shows how the shape of XPM pedestal changes as the pump power increases. Each graph is labeled with the average pump power entering the nonlinear fiber. It is clear that the two extreme polarization states cross at one point on each side of the CW probe when the pump power is increased. In these measurements, the pump polarization state is constant. We confirmed that the same behavior can be seen for any fixed pump polarization state. In an ideal case where the wavelength of pump and probe signals are far enough from each other, the XPM pedestal will be symmetric. In our experiment the wavelength separation between the two signals is only 7 nm and the spectral proximity of the strong pump causes some asymmetry in the XPM pedestal. For this reason the crossing behavior is not symmetric around the CW probe.

If we consider either one of Fig. 3.7 (a)-(d), we have experimentally confirmed that all other polarization states generate XPM spectra that lie in between of these two extreme polarization states. This means that they all cross one point on each side of the probe signal. The physical reason for this crossing is that the equations that describe the evolution of x
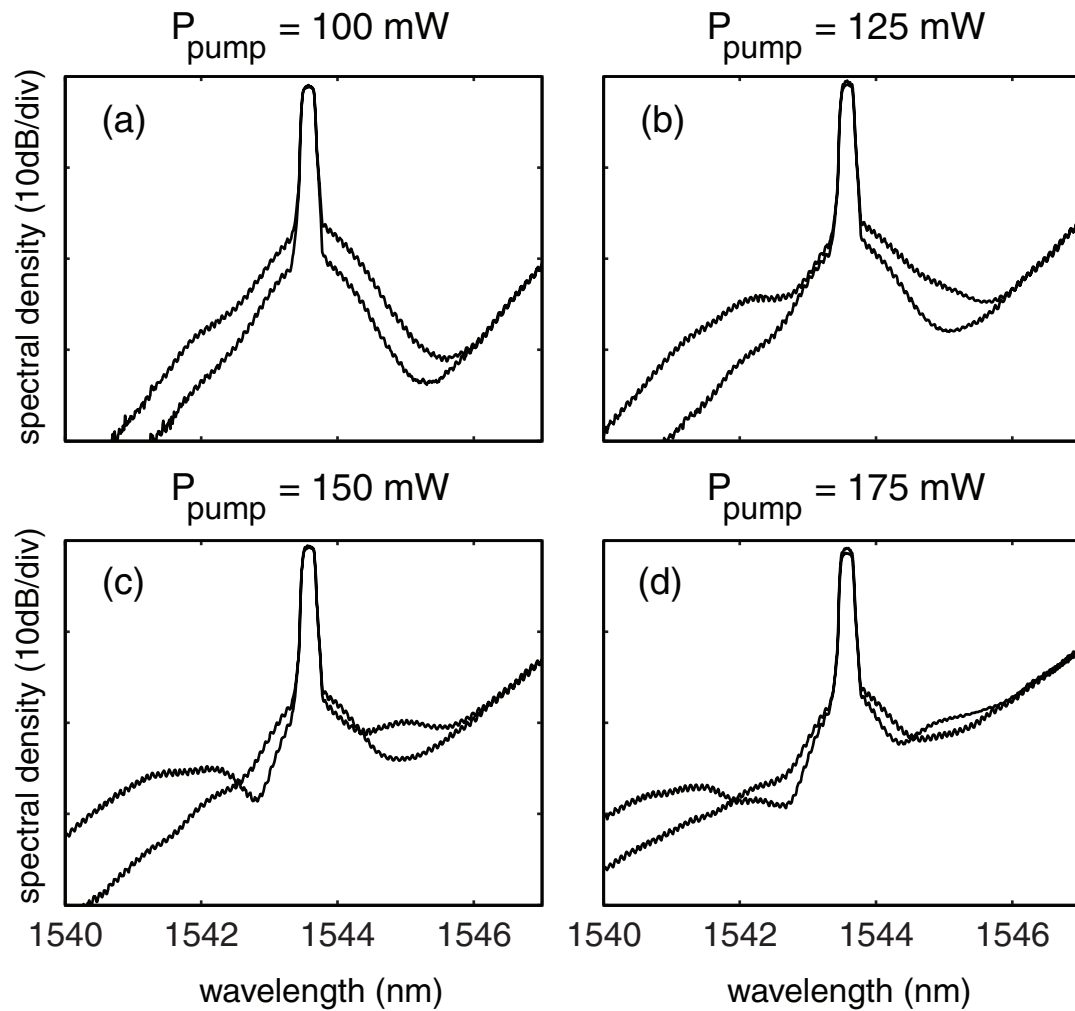
Fig. 3.7: Polarization dependence of XPM spectral density for CW probe signal and pulses pump signal. Parts (a)-(d) plot two extreme cases of probe polarization states for four difference pump average power levels. (RBW = 0.2 nm)

and y probe electric field components are linear with respect to the probe electric field. As a result of this linearity, superposition applies to such a system. One can write the input probe electric field as a linear combination of two orthogonal polarization states. Because of the linearity, the output probe electric field will also be a linear combination of two orthogonal electric fields. Conservation of energy requires that if the spectra for the two orthogonal states intersect at one point, the linear combination of those states also crosses the same point. This concept can be used for polarization-independent cross-phase modulation. If the spectrum is filtered with a narrow-band band-pass filter that is tuned to the crossing point, the output will be polarization-independent.

This peculiar crossing behavior is also confirmed through numerical simulations. We have developed a vector split-step code in order to solve the vector form of the nonlinear Schrödinger equation as provided in [82,87]. The split-step method is described in [88–90]. In our simulation we assume the fiber has linear birefringence and we take into account the effect of dispersion and loss in the fiber. The fiber parameters used in the simulation are taken from Table 3.1. Fig. 3.8 (a) plots the simulated XPM spectra for the two extreme polarization states as well as for 14 other polarization states equally distributed on the Poincaré sphere. The simulation is performed for the pump average power equal to 150 mW and confirms that all 16 spectra cross at one single wavelength on each side of the CW probe. The simulation results are spectrally convolved with an 0.2 nm window in order to match the resolution bandwidth of the optical spectrum analyzer that was used in the measurements. The experimental measurements from Fig. 3.7 (c) are reproduced for

81

comparison in part (b) of Fig. 3.8. Comparison between the experimental results and the simulation show excellent agreement between the two. We emphasize that all the parameters used in the simulation were based on the fiber data sheet or our measurements. The only free parameter that was not possible to measure in our experimental setup is the input pump polarization state.

3.1.3   Simple Analytical Model

As shown in Fig. 3.7, polarization independent behavior can only be obtained when the pump power is properly chosen. One important question to ask is at what power level the crossing points occur. Although numerical simulation can accurately describe this system, it is not easy to generalize to other fibers or pulsewidths. If we simplify the problem by neglecting dispersion and walk-off, it is possible to derive an analytical formula for the power at which the crossing will occur. As we see in Fig. 3.7 (c) and (d), changing the power changes the location of the crossing point. Therefore, this should be done considering a specific wavelength offset at which the crossing is to occur. In this subsection, we will discuss a simple method to find the required power level for a given wavelength offset.

In this model, we first consider the case of pump and probe signals being linearly polarized along the same direction. In this case maximum cross-phase modulation efficiency is achieved. Since the fiber has no birefringence, we can treat the problem as a scalar one. As we mentioned before, we are neglecting the effects of walk-off, dispersion and bire-

(a) SIMULATION

Power (5dB/div)

polarization-independent

wavelength (nm)

(b) MEASUREMENT

Power (5dB/div)

polarization-independent

wavelength (nm)
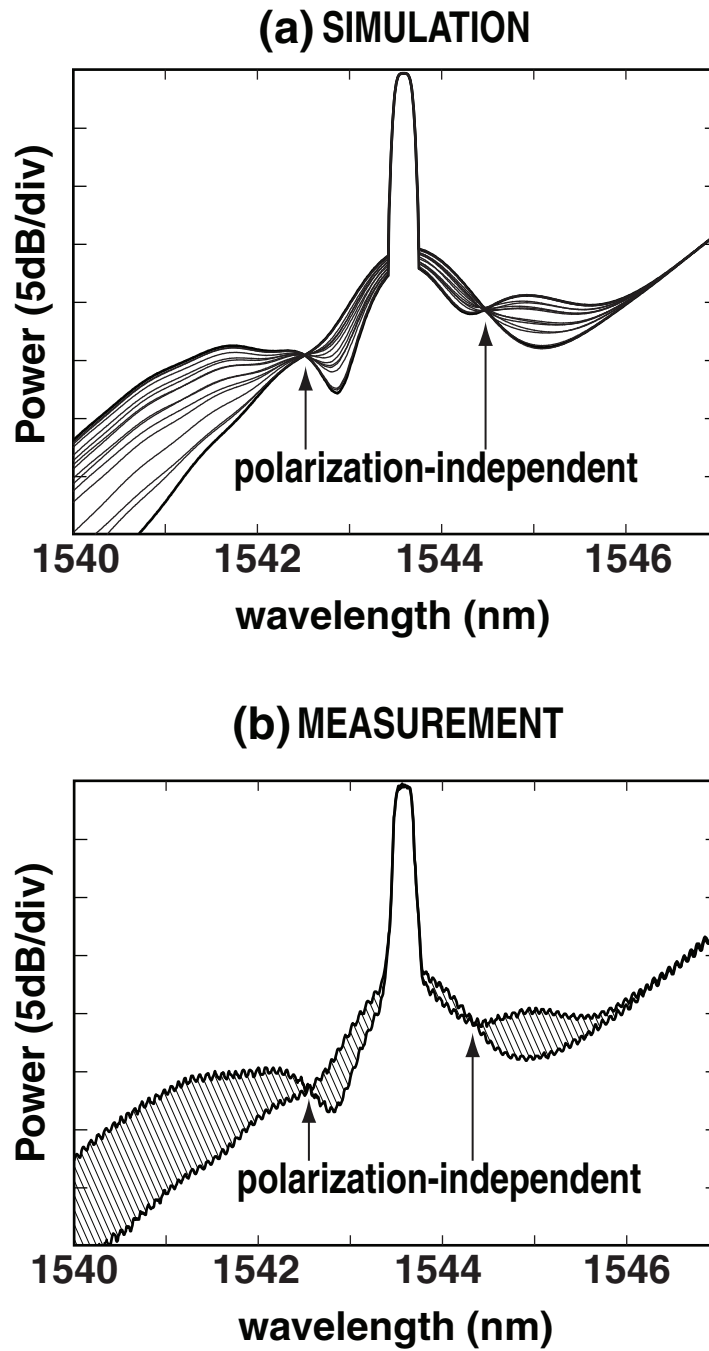
Fig. 3.8: (a) Simulation results and (b) measurements at 150 mW pump average power. Good agreement between the two can be seen. Polarization-independent points on both sides of the CW probe can be predicted with our numerical simulation.

fringence. In addition, we also neglect the effect of four-wave mixing between pump and probe on the XPM pedestal. If $A_1(z,t)$ and $A_2(z,t)$ are the slowly varying amplitudes of pump and probe signals as a function of travel distance in the fiber z, the evolution of the probe signal can be written as:

$$\frac{\partial A_2(z,t)}{\partial z} = 2i\gamma |A_1(z,t)|^2 A_2(z,t) \quad , \tag{3.4}$$

where we have assumed that the pump signal is much stronger than the probe signal. Note that the time derivatives have been eliminated by moving with the frame of reference travelling at the group velocity and neglecting the dispersion effect. To estimate the conditions under which polarization independent performance can be attained, we consider a Gaussian pump pulse at the input of the fiber described by

$$|A_1(0,t)|^2 = P(t) = P_0 e^{-t^2/T^2} \quad . \tag{3.5}$$

In a fiber with no dispersion and loss factor α, we can write the pump power as a function of z:

$$|A_1(z,t)|^2 = P_0 e^{-\alpha z} e^{-t^2/T^2} \quad . \tag{3.6}$$

The phase of the probe signal gets modulated by the pump pulses based on Eq. 3.4. Assuming that the amplitude modulation on the probe signal is small, $A_2(z)$ can be written as:

$$A_2(z,t) = \sqrt{P_{\text{CW}}} e^{-\alpha z} e^{i\phi(z,t)} \quad , \tag{3.7}$$

84

where P_{CW} is the CW probe power and $\phi(z, t)$ is the nonlinear phase induced by the pump signal. Substituting in Eq. 3.4 and integrating over the length of the fiber L, yields:

$$\phi(L, t) = 2\gamma P_0 \int_0^L |A_1(z, t)|^2 dz \quad . \tag{3.8}$$

Substituting Eq. 3.6, we can write the nonlinear phase shift in this form:

$$\phi(L, t) = \phi_0 e^{-t^2/T^2} \quad , \tag{3.9}$$

where the dimensionless quantity $\phi_0 \equiv 2P_0\gamma L_{\text{eff}}$ is the amplitude of the nonlinear phase shift and $L_{\text{eff}} = (1 - e^{-\alpha L})/\alpha$ is the effective length.

The spectrum of the modulated CW tone cannot be expressed analytically, but it can be readily computed numerically based on Eqs. 3.7 and 3.9. When ϕ_0 is small, the XPM spectrum grows in proportion to ϕ_0^2, but as the peak phase shift approaches π, the XPM spectrum begins to exhibit oscillations. This effect is shown in Fig. 3.9(a), which plots the calculated XPM spectral power at an offset frequency of $\Delta\nu = \pm 0.2/T$ away from the CW tone, as a function of $2P_0\gamma L_{\text{eff}}$.

The foregoing analysis assumed that the pump and probe signals were linearly co-polarized. If the CW probe signal is instead polarized orthogonal to the pump then the nonlinearity γ will decrease by a factor of $1/3$ [91]. In order to show where this factor of $1/3$ comes from, we write the coupled nonlinear Schrodinger equations simplified for

the case of zero-dispersion, non-birefringent fiber. For simplicity of the calculations, we assume that the pump signal is polarized along the x axis. The equations that describe the evolution of the x and y components of the probe signal are [87, 92]:

$$
\begin{aligned}
\frac{\partial A_{2x}(z,t)}{\partial z} &= 2i\gamma |A_{1x}(z,t)|^2 A_{2x}(z,t) \\
\frac{\partial A_{2y}(z,t)}{\partial z} &= \frac{2i\gamma}{3}|A_{1x}(z,t)|^2 A_{2y}(z,t) \quad ,
\end{aligned}
\tag{3.10}
$$

where A_{1x} is the pump slowly varying amplitude (polarized along x direction) and A_{2x} and A_{2y} are the x and y components of the probe slowly varying amplitude. It is clear from these equations that the probe nonlinear phase shift for the component that is co-polarized with the pump, x, is $3\times$ higher than that of the cross-polarized component, y.

The two points marked in Fig. 3.9(a) show that for a given peak power P_0, the nonlinear coefficient γ can decrease by a factor of $1/3$ without changing the XPM spectral power. Under this condition, the two orthogonal polarization states will produce the same XPM spectral power at the offset frequency, which leads to polarization-independent operation. Fig. 3.9(b) plots the two calculated XPM spectra that correspond to the points labeled in (a), showing the distinct crossing points analogous to those observed experimentally.

For the selected offset frequency of $\Delta\nu = \pm0.2/T$, polarization independent behavior is predicted when $2P_0\gamma L_{\text{eff}} = 5.5$, whereas for the actual parameters reported here we instead calculate $2P_0\gamma L_{\text{eff}} = 10.9$. The discrepancy arises because the simple theory does not account for dispersion and signal walk-off, which can significantly decrease the XPM
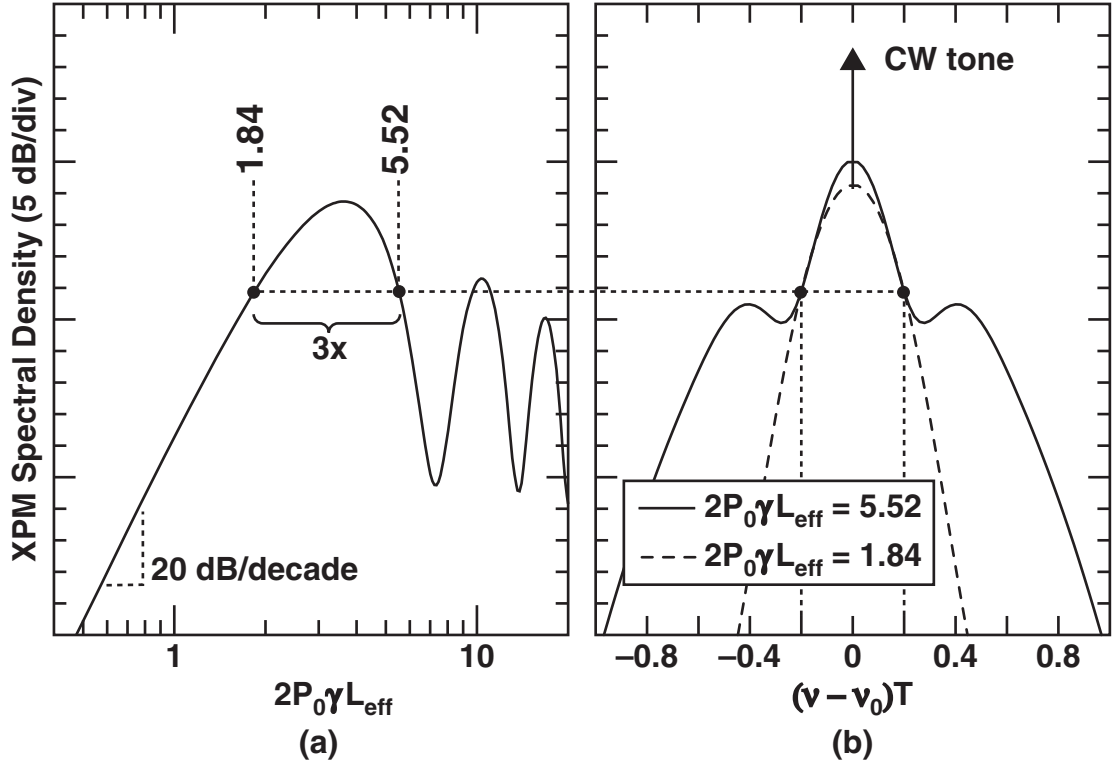
Fig. 3.9: (a) Calculated XPM spectral power at an offset frequency of $(\nu - \nu_0) = \pm 0.2/T$, as a function of $2P_0\gamma L_{\mathrm{eff}}$. The two labeled points show that γ can change by $3\times$ without changing the XPM spectral power. (b) Calculated XPM spectra for the two points labeled in (a), showing the crossing points at $(\nu - \nu_0) = \pm 0.2/T$.

efficiency [93, 94]. As demonstrated in Fig. 3.8(a), more exact agreement between theory and experiment can be obtained by including the measured dispersion and DGD in the simulation. Nevertheless, the dispersion-free theory described here illuminates the underlying physical principle and provides a useful order-of-magnitude estimate of the power needed to obtain polarization independent behavior.

3.1.4   Cross-Phase Modulation Experiment with Pulsed Probe

The concept of using the crossing point in the XPM spectrum in order to eliminate the polarization dependence can be used in optical demultiplexing, if the CW tone is replaced by a data signal comprised of pulses. Before we describe the demultiplexing experiment it is important to note that we are considering RZ data signals. Therefore the demultiplexing experiment can be better understood as cross-phase modulation between two optical pulses (clock and data). For this reason, we first setup an experiment to investigate the cross-phase modulation of a weak data pulse by a strong clock pulse. Our goal is to show through both experiment and numerical simulation that the concept of crossing point can be seen in this case as well. One key difference between the pulsed and CW cases is that for the pulsed case the XPM spectrum depends upon the relative delay τ between the clock and data. In this case the XPM spectral broadening of the probe can be asymmetric. In fact, the cross-phase modulation process causes the probe spectrum to shift to higher or lower frequency, depending on the relative delay between the clock and data. If the probe pulse leads the pump pulse, blue-shift of the probe spectrum occurs and vice versa. Fig. 3.10 shows the concept of spectral shift when two optical pulses are passed through nonlinear fiber. In parts (a) and (b) of the figure, blue- or red-shift occur depending on the relative delay between pulses. The figure shows a simplified picture and in reality the shape of the probe spectrum changes as it is shifted to blue or red side [80].

The experimental setup is shown in Fig. 3.11 which is similar to the one shown in
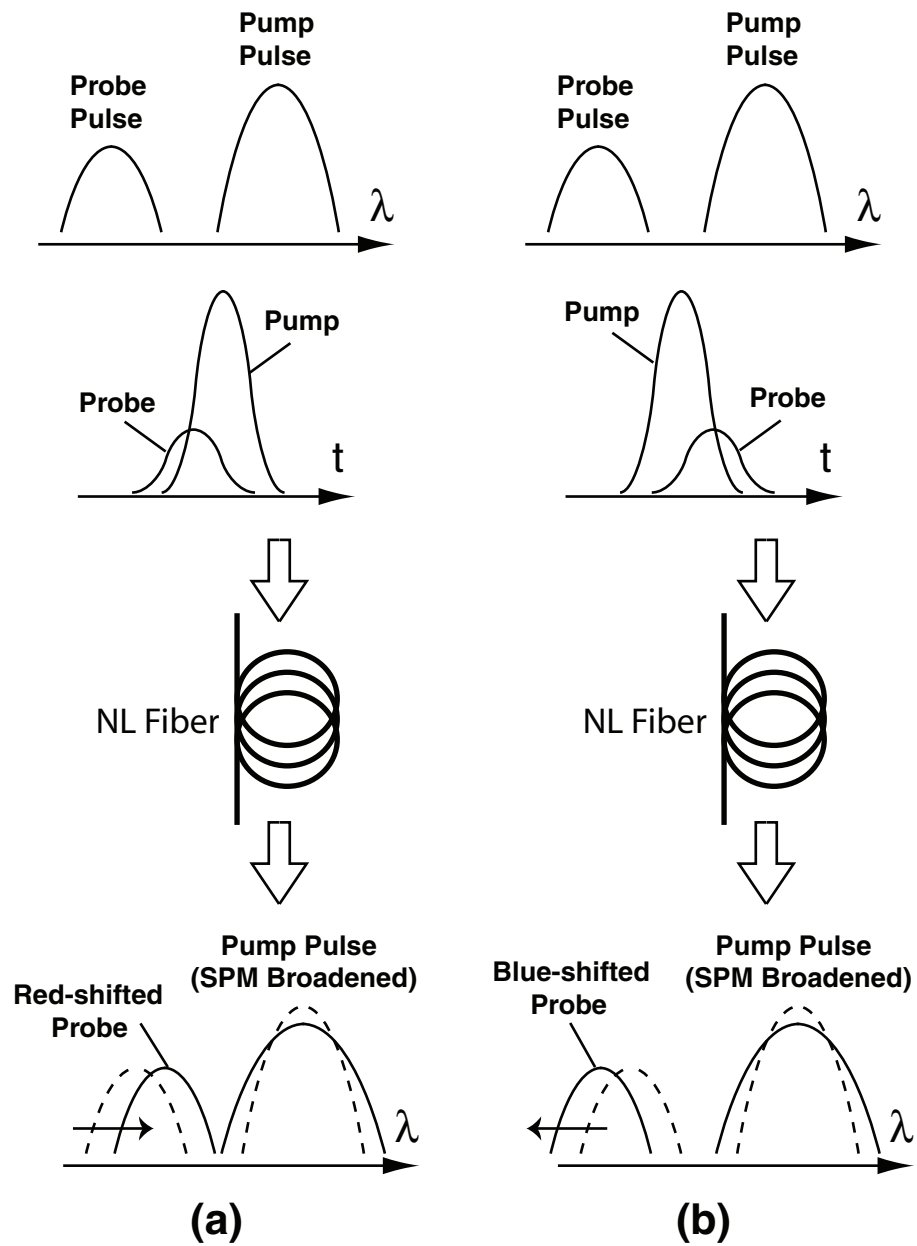
Fig. 3.10: Cross-phase modulation between two optical pulses. Spectral shift on the probe can occur to either blue (a) or red (b) side of the spectrum depending on the relative delay between the two pulses.
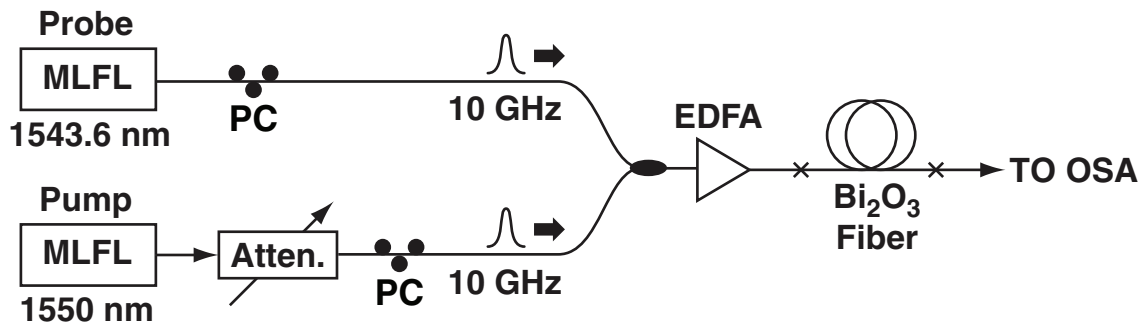
Fig. 3.11: Experimental setup for investigating XPM between two optical pulses.

Fig. 3.5. In this experiment the pulse-widths for probe and pump are 2.5 ps and 1.8 ps respectively. Both pulses are generated from actively mode-locked fiber lasers. The pump and probe average powers before entering the nonlinear fiber were measured to be 22.5 dBm and 12.5 dBm respectively.

3.1.5 Demonstration of Crossing Point for Pulsed Probe

Using the setup shown in Fig. 3.11 we measured the spectrum at the output of the nonlinear fiber for a range of probe polarization states while the pump polarization state was held constant. In this case, the amount of wavelength shift is proportional to the XPM efficiency, which depends on the relative polarization state of the pump and probe. This can be seen in Fig. 3.12 (a) which plots the minimum and maximum spectra obtained by adjusting the probe polarization. The dashed line depicts the spectrum before entering the fiber. It can be seen from the spectrum that the wavelength shifts for the two polarization states differ by a factor of 3.
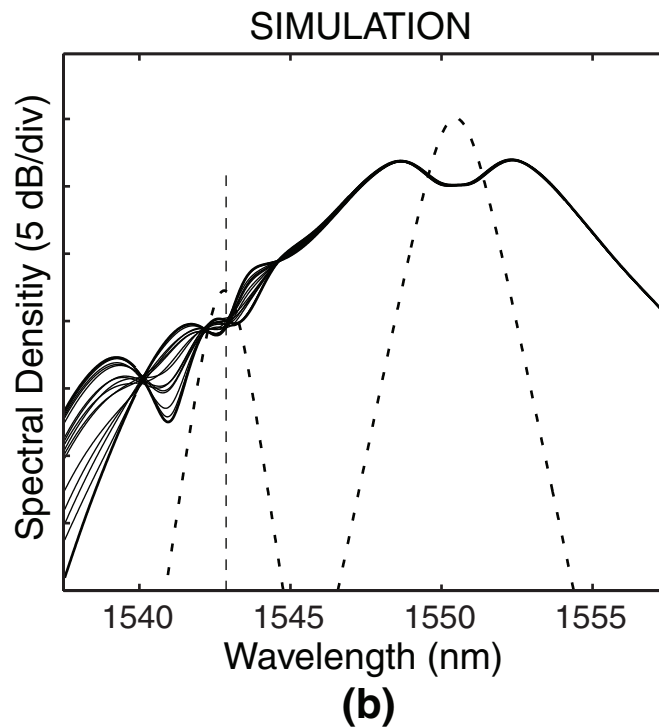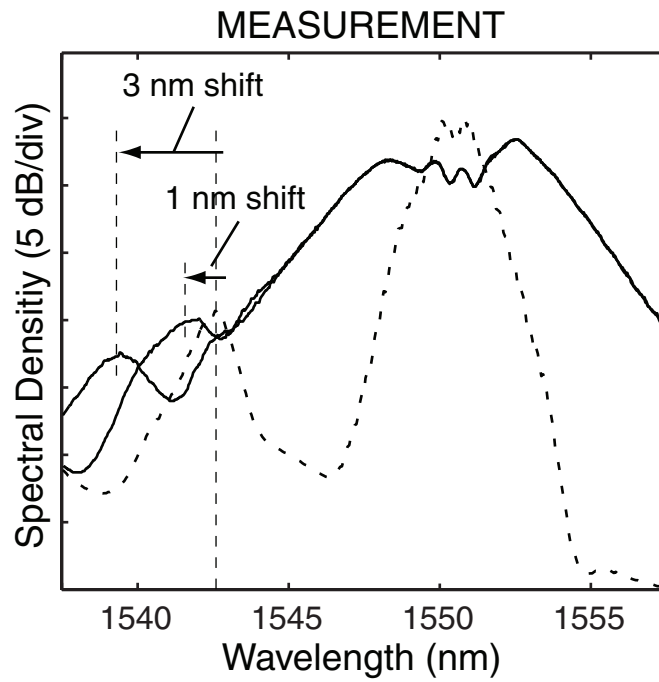
Fig. 3.12: Cross-phase modulation between two optical pulses. Part (a) shows the measured spectra for two extreme polarization states (solid curves) and the input spectrum (dashed curve). Part (b) plots the simulation results for the two extreme cases as well as 14 equally-spaced points on the Poincaré sphere.

As with the CW measurements, these results are confirmed by numerical simulations using the vector split-step software that we developed and used in Section 3.1.2. Similar to Section 3.1.2, We plotted the spectra for 16 different polarization states which are shown in Fig. 3.12 (b). Two of these 16 polarization states are the minimum and maximum cases while the other 14 are uniformly distributed points on the Poincaré sphere. Good agreement between the measurement and simulation results can be seen. As for the CW case, the experimental and simulation results show that the XPM spectra for all input polarization states cross at one wavelength. Polarization-independent demultiplexing can be achieved by band-pass filtering the spectrum around the crossing point, as described in the following section.

It is important to note that the pump power level determines the amount of wavelength shift for any given probe polarization state. Therefore the location of the crossing point depends upon the pump power level. This especially important for demultiplexing because we need the crossing point to occur at a wavelength that is sufficiently separated from the data center wavelength. When the crossing is point is too close to the data center wavelength, some of the high-bit-rate data signal can leak though the bandpass filter, which impairs the extinction ratio (or on-off ratio) of the switch. The following section presents a simple analytical model that approximates the pump power required to produce a sufficient spectral shift.

3.1.6 Simple Analytical Model

If we look at the amount of wavelength shift in Fig. 3.12, we can see that the spectral shift differs for two extreme polarization states by about a factor of 3. As we discussed in Section 3.1.3, the factor of 3 can be explained by the coupled nonlinear Schrodinger equations. As Eq. 3.10 shows, the nonlinear phase shift for co-polarized and cross-polarized components of the probe differ by a factor of 3. Therefore, the frequency shift for these two components differ by the same factor. As in Section 3.1.3, this effect can be approximately described by using a scalar model in the nonlinear Schrödinger equation, allowing the nonlinear coefficient γ to vary by a factor of up to $3\times$ depending on the relative polarization states of the pump and probe. This model considered a nonlinear fiber with no birefringence and dispersion. In this case if the pump is linearly polarized, the difference between XPM efficiency when probe is co-polarized or cross-polarized with respect to the pump is exactly a factor of 3. Under these conditions, the crossing point is predicted to be approximately at the midpoint between the two extreme cases. As shown schematically in Fig. 3.13, the polarization-independent crossing point wavelength is therefore expected to occur at about $\frac{2}{3}$ of the maximum wavelength shift. We emphasize that this is only an approximation used to find a relationship between the pump power and the offset wavelength of the crossing point. An accurate prediction of the crossing point location requires full numerical solution of the vector nonlinear Schrodinger equation, using the measured fiber parameters such as dispersion, birefringence and loss.
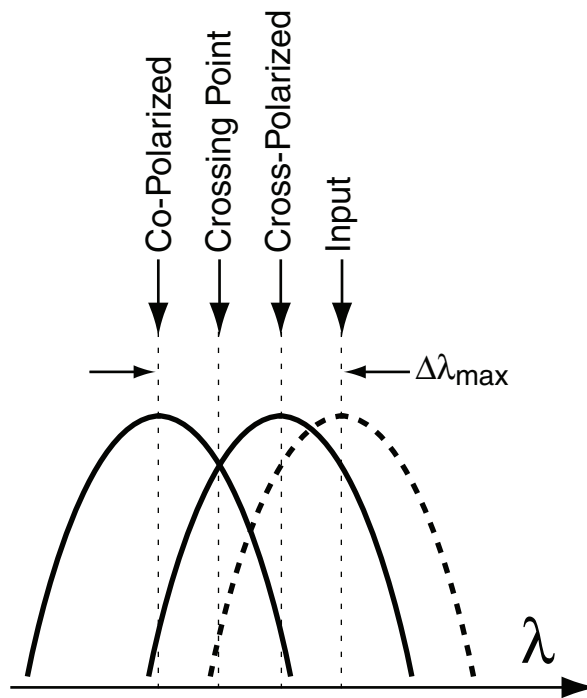
Fig. 3.13: Simple diagram showing the blue-shift in the probe spectrum. Two extreme cases correspond to co-polarized and cross-polarized pump and probe combinations. Intersection point is approximately in the midpoint between the two extreme cases.

In order to estimate the offset wavelength at which the crossing occurs, we need to determine the maximum frequency shift caused by cross-phase modulation, a quantity that depends upon the relative delay between the two signals. We assume that the probe pulse arrives to the nonlinear fiber at time $t = 0$ and that both signals travel with the same group velocity. We consider a Gaussian pulse shape for the pump signal with a time delay t_d relative to the probe pulse. If we use the time variable $\tau = t + t_d$, we can write the pump power as:

$$P(t) = P_0 e^{-\tau^2/T^2} \quad . \tag{3.11}$$

The nonlinear phase shift for the probe signal can be written as:

$$\phi(t) = 2P_0 \gamma L_{\text{eff}} e^{-\tau^2/T^2} = \phi_0 e^{-\tau^2/T^2} \quad , \tag{3.12}$$

where ϕ_0 is the amplitude of the nonlinear phase shift. All the parameters are defined as described in section 3.1.3. We can write the XPM-induced frequency chirp as [82, 95]:

$$\Delta\nu(\tau) = -\frac{1}{2\pi} \frac{\partial\phi(\tau)}{\partial\tau} = 2\phi_0 \tau e^{-\tau^2/T^2} \tag{3.13}$$

Fig. 3.14 plots $\Delta\nu(\tau)$ as a function of τ. In order to get the maximum frequency shift one should choose t_d such that $|\Delta\nu|$ is maximum around $t = 0$ (or $\tau = -t_d$). This is because the probe pulse is centered around $t = 0$ and if the probe pulse-width is not much longer than the pump pulse-width, we can assume a constant frequency shift of $|\Delta\nu_{\text{max}}|$ for
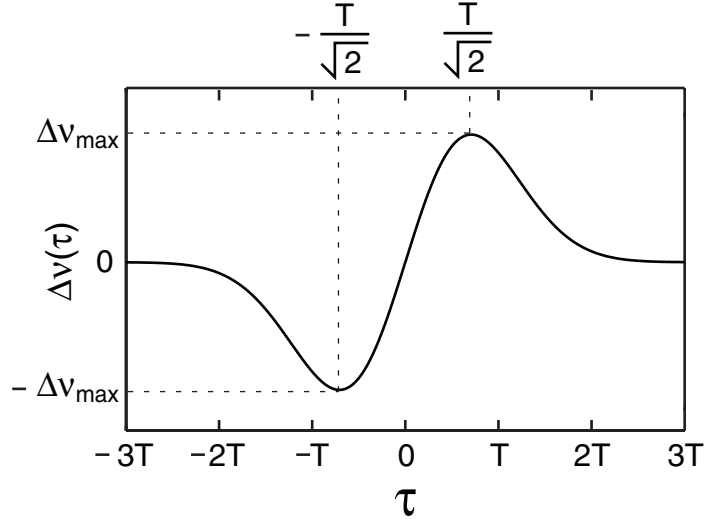
Fig. 3.14: XPM-induced frequency chirp caused by a Gaussian pump pulse as a function of τ.

the probe pulse. It is clear from Fig. 3.14 that the time delay to satisfy this condition should be:

$$t_{d,\mathrm{max}} = \pm \frac{T}{\sqrt{2}} \quad . \tag{3.14}$$

Substituting $\tau = \pm T/\sqrt{(2)}$ in Eq. 3.13, we find a formula for $\Delta\nu_{\mathrm{max}}$:

$$\Delta\nu_{\mathrm{max}}T = \frac{1}{2\pi}\sqrt{\frac{2}{e}}\phi_0 = \frac{1}{\pi}\sqrt{\frac{2}{e}}\gamma P_0 L_{\mathrm{eff}} \tag{3.15}$$

Using this formula one can find the maximum wavelength shift shown in Fig. 3.13 using the approximation:

$$\Delta\lambda \approx \frac{\lambda^2}{c}\Delta\nu \tag{3.16}$$

96

As we mentioned before, the offset wavelength at the crossing point can be approximated as $\frac{2}{3}$ of this maximum wavelength shift. In our experimental results shown in Fig. 3.12 the crossing point occurs at about 2.5 nm offset wavelength. Using our simple model the nonlinear phase shift amplitude is predicted to be $\phi_0 = 4.5$ which would correspond, for our fiber, to a peak power of $P_0 = 2.4W$, or an average power of 80 mW. This estimate is about 3 dB lower than what was actually used in the experiment. The discrepancy can be explained by the effect of the walk-off between pump and probe, fiber birefringence and approximations made in the simple analytical model. Nevertheless, this analysis provides a simple approximation for the power required to achieve polarization-insensitive operation.

3.1.7   160 Gb/s Demultiplexing Experiment

In the previous section we demonstrated that in the asymmetric broadening caused by cross-phase modulation between two pulses, a polarization-independent point can be found. We now show how this effect can be applied to the case of optical demultiplexing, in which a base rate (10 GHz) clock is used to extract every 16th pulse from a 160 Gb/s data signal. The only difference here is that the data spectrum consists of $N - 1$ pulses that are not affected by cross-phase modulation and 1 pulse that is asymmetrically broadened (spectrally-shifted) by the XPM process.

Fig. 3.15 shows the experiment used to demonstrate polarization-independent 160 Gb/s
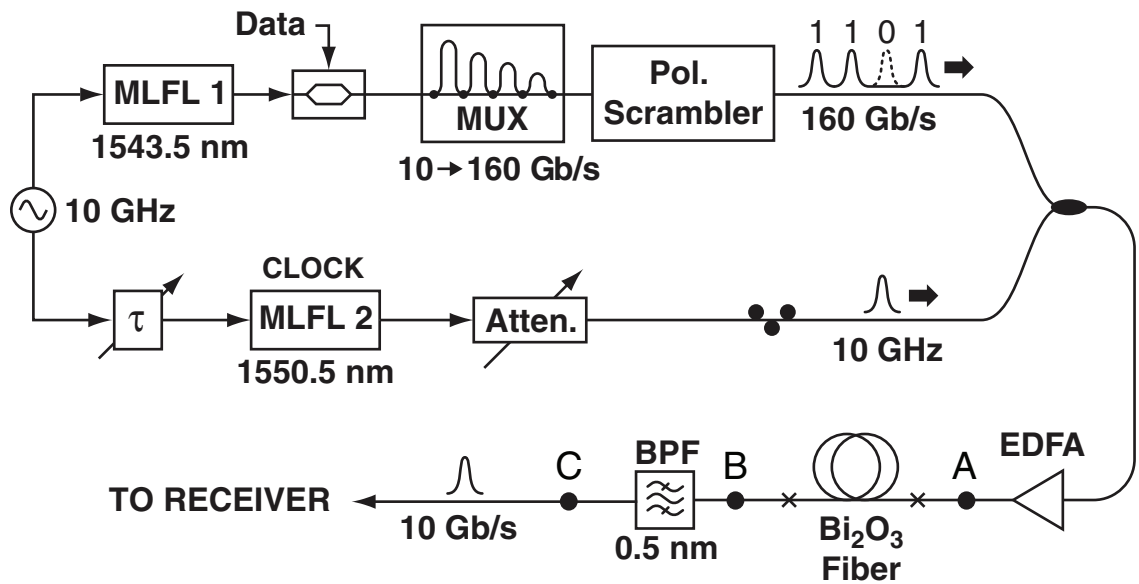
Fig. 3.15: Experimental setup used for demonstrating 160 Gb/s polarization-independent demultiplexing.

demultiplexing. The clock and data pulses were generated from two mode-locked fiber

lasers at 10 GHz with 2.8 ps and 2.0 ps pulsewidths, respectively. The data signal was

modulated with a 10 Gb/s, $2^{23} - 1$ pseudorandom data pattern and passively multiplexed

to 160 Gb/s. The smallest multiplexer delay was approximately 800 ps, to ensure decorre-

lation between adjacent bits. It is important to note that in a real system, the 16 channels

will be separate and independent. A passive multiplexer is used in this experiment to sim-

ulate a real system. The multiplexer uses polarization-maintaining fiber to guarantee that

all channels of the 160 Gb/s signal are co-polarized. The average powers of the data and

clock before entering the nonlinear fiber were 22.5 dBm and 12.5 dBm, respectively. As

discussed before, when the clock and data signals overlap in time, the strong clock signal

causes spectral shifting of the data signal through cross-phase modulation, and a subsequent bandpass filter was used to isolate the spectrally-shifted channel [7, 26].

Fig. 3.16 (a) plots the spectra at three different points (A,B,C) shown in Fig. 3.15. Points A, B and C correspond to the spectra before entering the fiber, after passing through the fiber and after the bandpass filter respectively. These spectra are plotted for one fixed polarization state of the data signal. In order to achieve polarization-independent demultiplexing, we need to tune the bandpass filter to point at which the spectra for all possible data polarization states intersect. This is shown in Fig. 3.16 (b) where the XPM-induced spectral shift is plotted for maximum and minimum cases. It can be seen that the crossing point and the bandpass filter output are aligned. As seen in this figure, the optimum position for the bandpass filter is not necessarily the wavelength at which the XPM spectrum is maximum.

In order to evaluate the system performance in the presence of polarization fluctuations, a high-speed polarization scrambler was inserted in the data path. The polarization scrambler produces the maximum degree of impairment from polarization fluctuations. The clock power and bandpass filter wavelength were adjusted while monitoring the bit error rate (BER) and eye diagram in order to achieve the lowest degree of polarization dependence. Fig. 3.17(a) plots the measured bit error rate (BER) vs. received optical power for back-to-back 10 Gb/s operation and for the 160 Gb/s demultiplexer. The circles indicate the BER obtained when the data polarization is constant, and the squares show that nearly identical performance is obtained when the data polarization is scrambled. The 3dB power
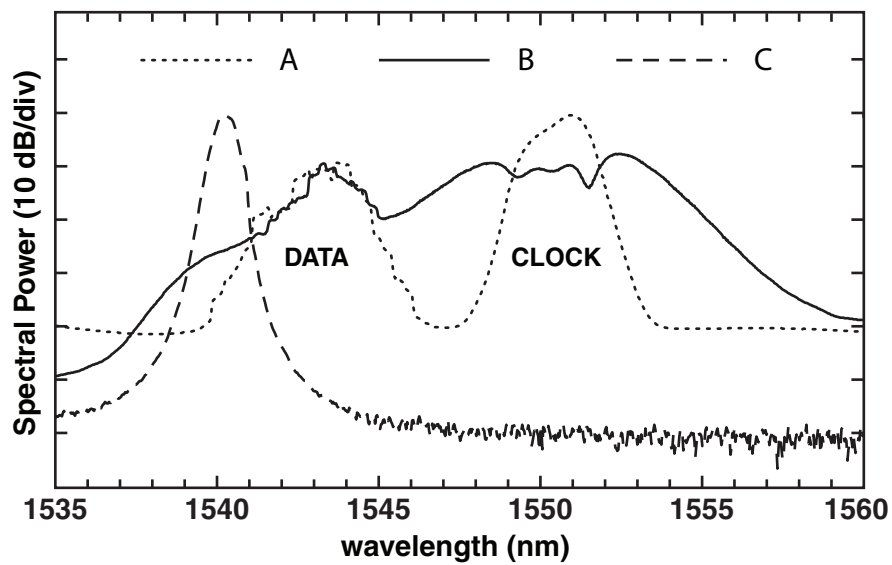
(a)
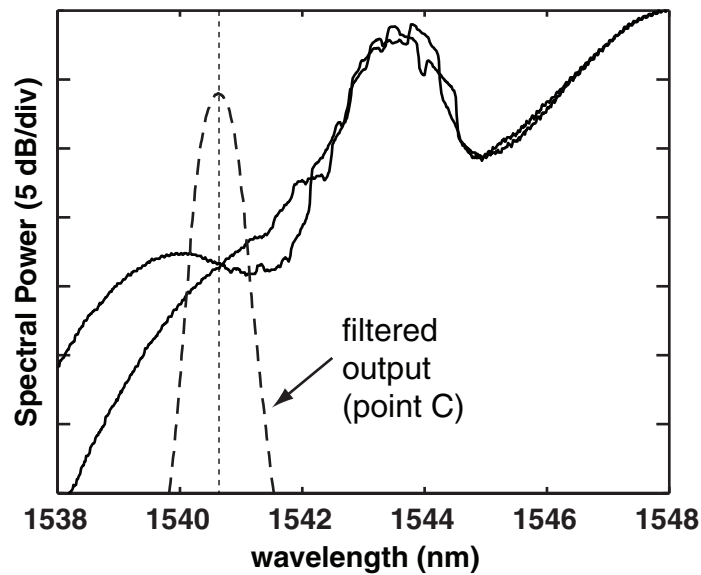
(b)

Fig. 3.16: (a) Measured spectra at three different points (A,B,C) in the demultiplexing experiment for a fixed data polarization state. (b) Magnified XPM-broadened data spectrum for maximum and minimum cases (solid curves) and the filtered output (dashed curve) showing alignment with the crossing point.

100
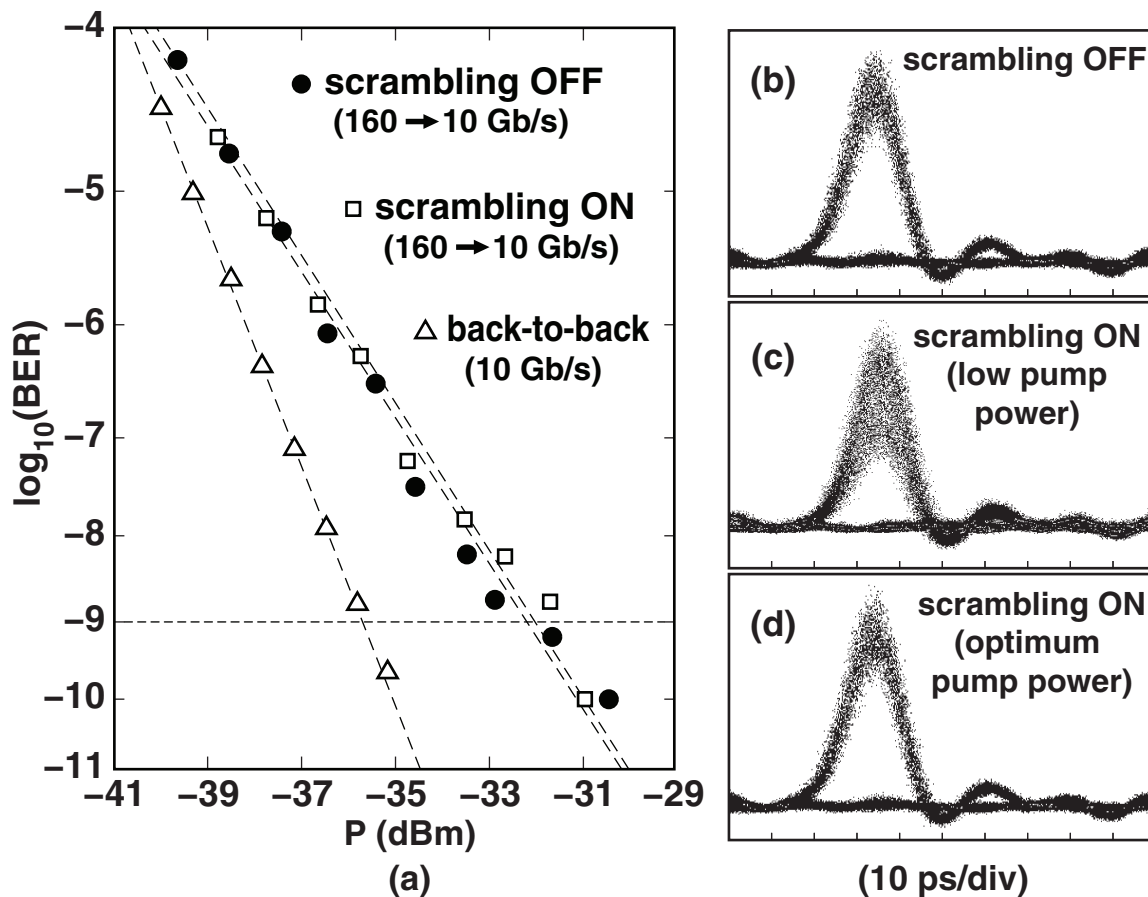
Fig. 3.17: (a) Bit error rate vs. received power for the 160 Gb/s demultiplexer, showing little penalty when polarization scrambling is enabled. Measured eye diagram of demultiplexed 10 Gb/s data while (b) polarization scrambling is disabled, (c) polarization scrambling is enabled but pump power is lower that optimum level and (d) polarization scrambling is enabled and optimum pump power is used.

penalty between back-to-back experiment and the demultiplexing results can be seen from these plots. This is due to extra amplification of the signal in the demultiplexing experiment which degrades the optical signal-to-noise ratio. Fig. 3.17(b) shows the demultiplexed eye diagram (10 Gb/s) when the polarization scrambler is disable. Part (c) shows the same eye diagram when the scrambling is enabled but the pump power is lower than the optimum level. In this case the crossing point and bandpass filter are not aligned and the system is polarization dependent as shown by the partial eye closure. Part (d) shows the eye diagram while the scrambling is enabled and the pump power is adjusted to the optimum level. In this case, the system is polarization independent as seen by comparing with part (b).

Similar behavior is seen for all 16 demultiplexed channels. In order to confirm this, we measures the BER vs. power for all 16 channels in the presence of polarization fluctuations. Fig. 3.18 plots the sensitivity curves for the 16 channels. We have plotted the channels in groups of 4 since it is otherwise difficult to show all 16 channels on one graph. The small differences seen between the channels is attributed to imperfect multiplexing of the original 10 Gb/s signal up to 160 Gb/s. We also captured the eye diagram for all 16 channels while the polarization is scrambled. Fig. 3.19 shows the eye diagrams for 16 channels in the 160 Gb/s data. The time difference between two adjacent channels is 6.25 ps. As seen in this figure, all channels are almost identical which agrees with out BER measurements in Fig. 3.18.
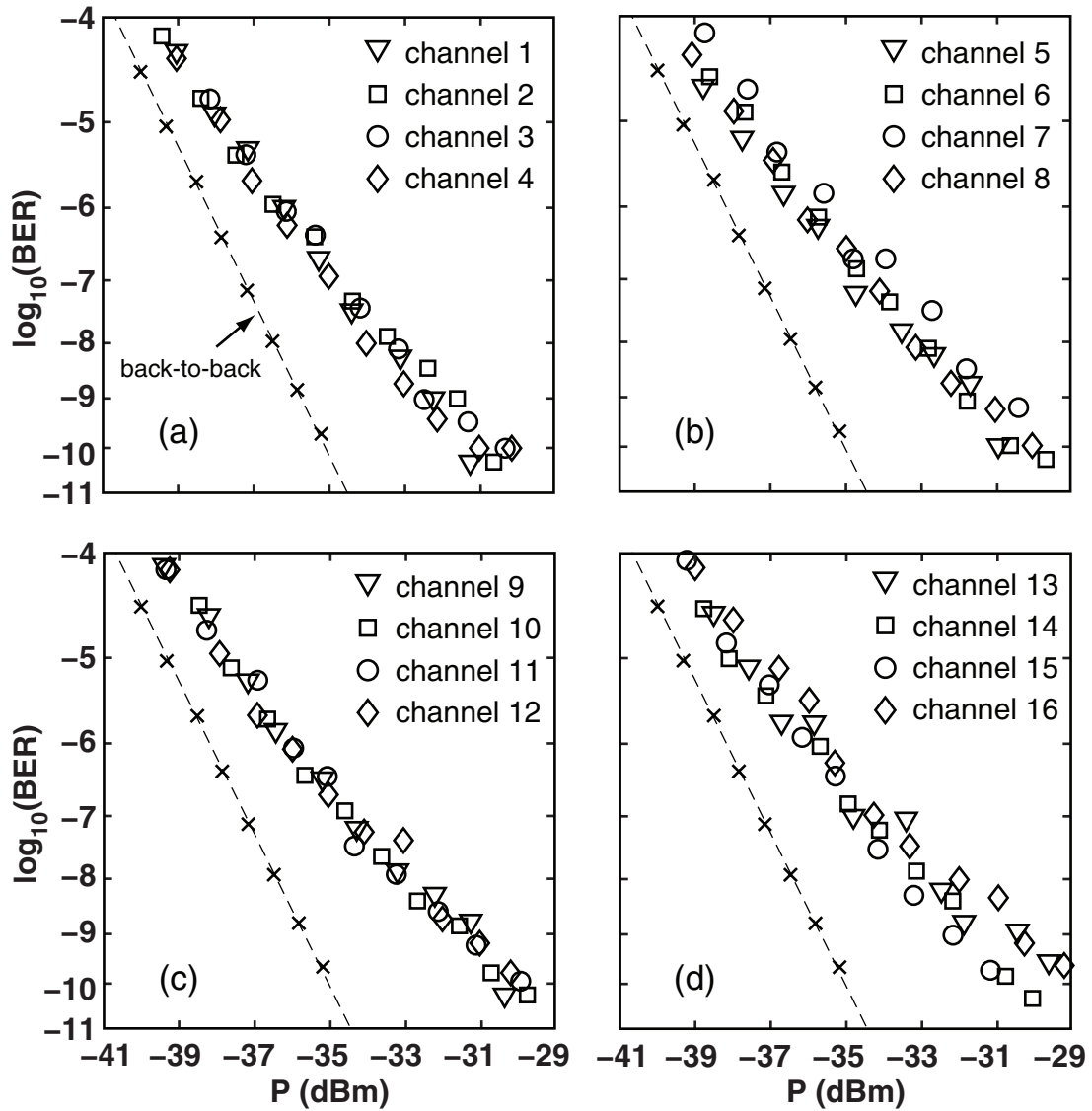
Fig. 3.18: BER vs. received power for 16 channels in the 160 Gb/s data stream. The channels are plotted in groups of 4 in parts (a)-(d).
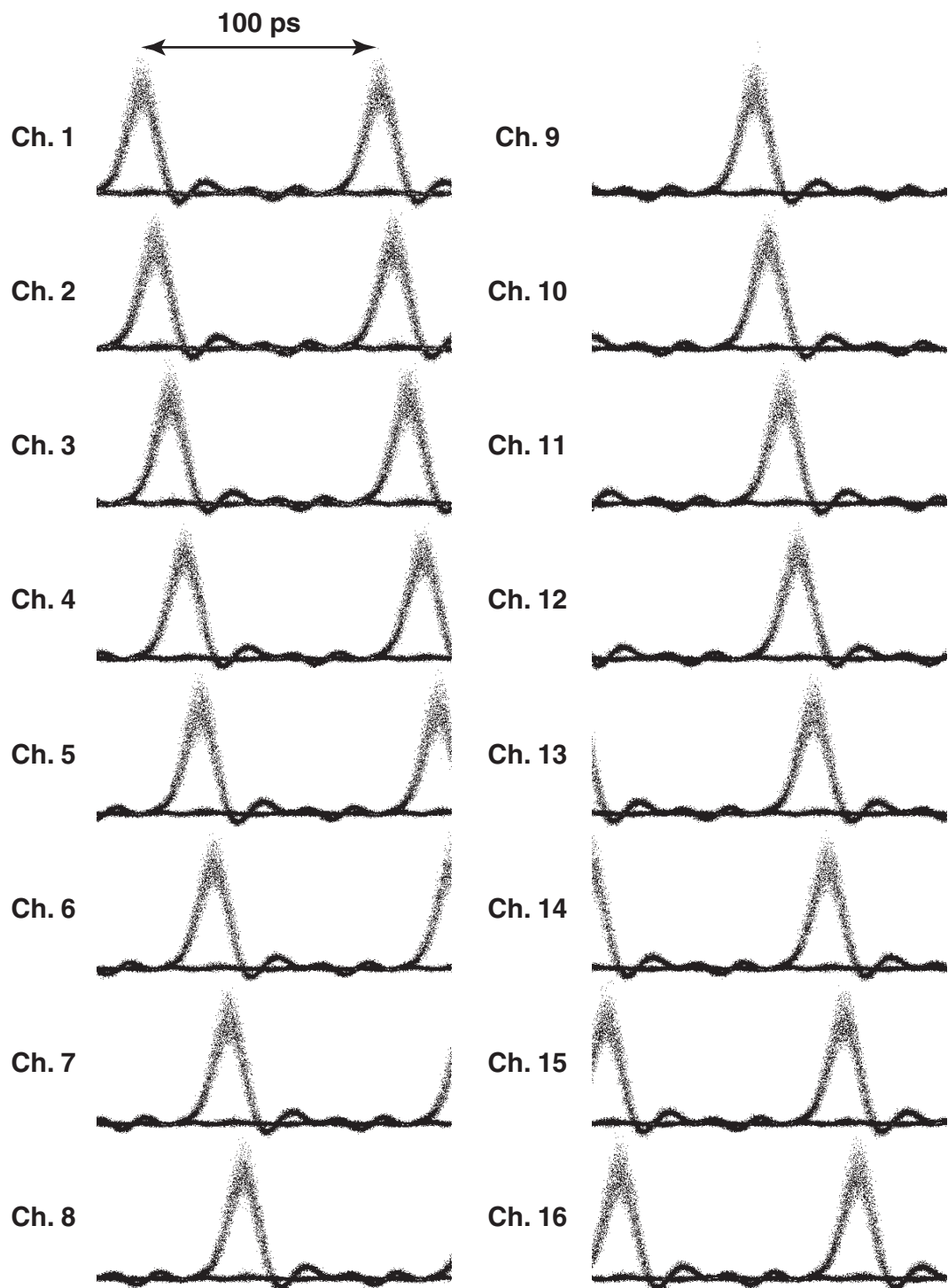
Fig. 3.19: Eye diagrams of the 16 channels in the 160 Gb/s data captured as the data polarization is scrambled.

3.2   Polarization-Independent Demultiplexing in Birefringent Photonic Crystal Fiber

In this section we look at another simple method to eliminate the polarization-dependence from the cross-phase modulation process. As we discussed in section 3.1, many new non-linear fibers have significant linear birefringence. Some birefringence in nonlinear fiber can be tolerated as long as the total differential group delay (DGD) is small compared to the pulse-widths used in the experiment. In this section we consider a 30m-long nonlinear fiber with photonic crystal structure. The measured value for the total DGD in the fiber is about 1.25 ps which is about 8 times higher that the bismuth-oxide-based fiber. Table 3.2 shows some of the parameters for the photonic crystal fiber used in the experiments in this section. The fiber is made by Crystal Fiber A/S (NL-1550-NEG-1) and the data provided in the table is taken from the fiber data sheet except for the DGD that is measured. The cross-section of the photonic crystal fiber is shown in Fig. 3.20.

Fiber Parameter	Value	Unit
Nonlinear Parameter (γ)	11	$\text{W}^{-1}\text{km}^{-1}$
Dispersion (D)	between -0.75 and 0	ps/nm·km
Loss	0.008	dB/m
Effective Area (A_{eff})	3.5	μm^2
Length	30	m
Differential Group Delay (DGD)	1.25	ps

Tab. 3.2: Parameters of the nonlinear photonic crystal fiber
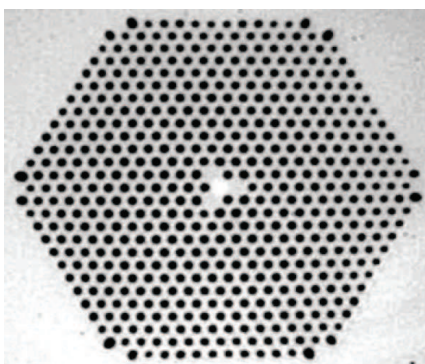
Fig. 3.20: Cross-section of the photonic crystal fiber made by Crystal Fiber A/S.
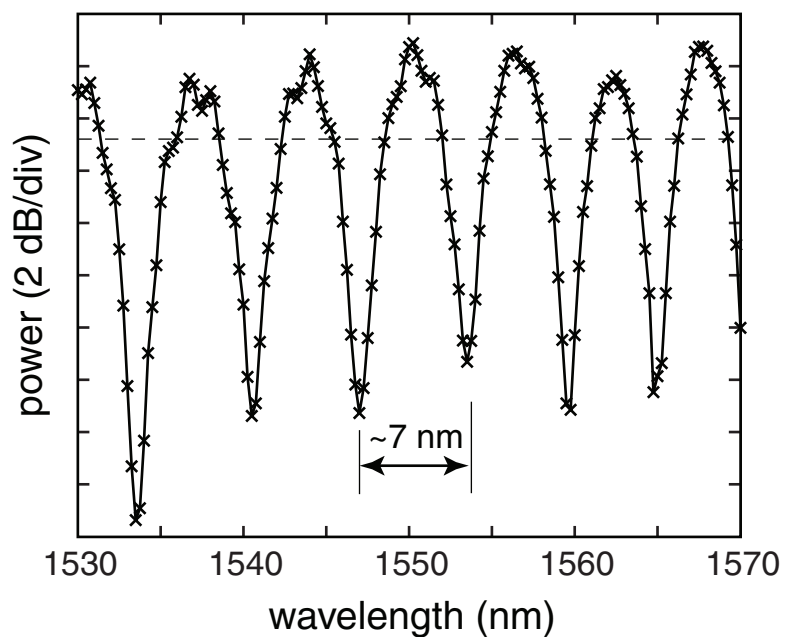
Fig. 3.21: Measured power as a function of wavelength used to determine the DGD in the photonic crystal fiber. Setup is shown in Fig. 3.2 (a).

The DGD is measured using the wavelength scanning method described in 3.1. The measured power as a function of wavelength is given in Fig. 3.21. From this measurement, the fiber DGD is calculated to be $\Delta\tau = 1.25$ ps. It is important to determine if the fiber is in the short-length regime or the long-length regime [85]. In other words, we are interested in knowing if the fiber can be treated as a system with fixed principal axes. As we discussed before, this can be determined by the test given in [85]. By drawing a horizontal line at the mean power in Fig. 3.21 (that dashed line), we can count the number of mean crossings. This number is approximately equal to the total number of minima and maxima. This test shows that the fiber can be treated as one wave plate with fixed axes.

One noticeable difference between the fibers is that the nonlinear coefficient of this fiber is much lower than that of the bismuth-oxide-based fiber. On the other hand because of the low group velocity dispersion, one can use a much longer fiber (30m in this case). The photonic crystal (holey) structure for the fiber is used to increase the nonlinearity by decreasing the mode size while minimizing the dispersion around 1550 nm wavelength. If we calculate the parameter ϕ_0 (nonlinear phase shift amplitude) for the same power levels and pulsewidths used in our previous experiments we get $\phi_0 \sim 3$. This is about 3X lower than our experiments with bismuth-oxide-based fiber which indicates we need to increase the power level in order to achieve polarization-independent operation using the method described in section 3.1. The high power requirements make that approach impractical in this fiber. In this section we describe a new technique that uses the higher birefringence of the fiber to eliminate polarization dependence without any specific requirements on the

optical power. The general method for demultiplexing is based on spectral filtering of the XPM as described before.

3.2.1 Polarization-Independent cross-phase modulation in birefringent nonlinear fiber

One way to achieve polarization-independent cross-phase modulation is to use a circularly polarized pump [29, 30]. However, in a linearly birefringent fiber, there is no way to maintain the circular polarization state for the pump signal along the fiber. As a result of linear birefringence, any input polarization state that is not aligned with one of the principal axes will periodically evolve as it propagates along the fiber. The periodicity of this evolution is characterized by a parameter called the beat length. If $\Delta\beta$ is the difference between the propagation constants of the two principal axes, the beat length (L_B) is given by:

$$L_B = \frac{2\pi}{\Delta\beta} \quad , \tag{3.17}$$

and describes the distance over which the two eigenstates acquire a relative phase shift of 2π. The propagation constant β is generally wavelength dependent and therefore the pump and probe signals have different beat lengths. We will show that if the difference between these beat lengths is large enough, polarization-independent XPM is achievable.

Consider an electric field that consists of two optical frequencies (pump and probe):

$$\mathbf{E}(x, y, z, t) = \hat{x} \left[A_{1x}(z,t)\phi_{1x}(x,y)e^{i(\beta_{1x}z - \omega_1 t)} + A_{2x}(z,t)\phi_{2x}(x,y)e^{i(\beta_{2x}z - \omega_2 t)} \right]$$

$$+\hat{y} \left[A_{1y}(z,t)\phi_{1y}(x,y)e^{i(\beta_{1y}z - \omega_1 t)} + A_{2y}(z,t)\phi_{2y}(x,y)e^{i(\beta_{2y}z - \omega_2 t)} \right] \quad ,$$

where $\phi(x,y)$ represents the transverse electromagnetic mode, ω_1 and ω_2 are optical frequencies associated with pump and probe respectively and β_{ij} ($i = 1, 2$ and $j = x, y$) represent the propagation constants for each frequency and for x- and y- polarizations. A_{ij} are the slowly varying amplitudes of the corresponding electric field components. The coupled equations that describe the evolution of pump and probe signals are given in Ref. [92]. Assuming that the pump ($i = 1$) signal is much stronger than the probe signal ($i = 2$), the probe slowly varying amplitude is governed by the following set of coupled nonlinear equations:

$$\frac{\partial A_{2x}}{\partial z} + \beta'_{2x}\frac{\partial A_{2x}}{\partial t} + \frac{i}{2}\beta''_{2x}\frac{\partial^2 A_{2x}}{\partial t^2} = i\gamma \left(2|A_{1x}|^2 + \frac{2}{3}|A_{1y}|^2 \right) A_{2x}$$

$$+\frac{2i\gamma}{3} A^*_{1x}A_{1y}A_{2y}e^{i[(\beta_{1y} - \beta_{1x}) + (\beta_{2y} - \beta_{2x})]z} \qquad (3.18)$$

$$+\frac{2i\gamma}{3} A_{1x}A^*_{1y}A_{2y}e^{i[(\beta_{1y} - \beta_{1x}) - (\beta_{2y} - \beta_{2x})]z}$$

$$\frac{\partial A_{2y}}{\partial z} + \beta'_{2y}\frac{\partial A_{2y}}{\partial t} + \frac{i}{2}\beta''_{2y}\frac{\partial^2 A_{2y}}{\partial t^2} = i\gamma \left(2|A_{1y}|^2 + \frac{2}{3}|A_{1x}|^2 \right) A_{2y}$$

$$+\frac{2i\gamma}{3} A^*_{1y}A_{1x}A_{2x}e^{i[(\beta_{1x} - \beta_{1y}) + (\beta_{2x} - \beta_{2y})]z} \qquad (3.19)$$

$$+\frac{2i\gamma}{3} A_{1y}A^*_{1x}A_{2x}e^{i[(\beta_{1x} - \beta_{1y}) - (\beta_{2x} - \beta_{2y})]z} \quad ,$$

where β'_{ij} and β''_{ij} are the first and second derivatives of the propagation constant with respect to the frequency evaluated at the carrier frequency. For example $\beta''ij$ is defined as:

$$\beta''_{ij} = \left.\frac{\partial^2 \beta_j(\omega)}{\partial \omega^2}\right|_{\omega=\omega_i} \tag{3.20}$$

The first and second equations describe the evolution of the x and y components of probe respectively. The probe polarization components A_{2x} and A_{2y} are coupled to one another through the last two terms on the right hand side of Eqs. 3.18-3.19. Under certain conditions, however, these terms may be neglected.

In a birefringent fiber, the beat length is usually shorter than the length of the fiber (L). This condition can be expressed as:

$$|\beta_y - \beta_x|L > 2\pi \tag{3.21}$$

In this case, the second term on the RHS of 3.18 and 3.19 can be neglected. This is because the exponential term will oscillate within the length of the fiber and average to a negligible value compared to the non-oscillatory terms. The cancellation of the oscillatory terms has been explained in [82] and [87]. Another way to explain this effect is that the light polarization evolves inside the fiber as a result of linear birefringence, and if the beat length for the evolution is smaller than the length of the fiber, the effect averages to a small value.

A stronger condition is required for the last term on the rand-hand-side to be negligible.

The pump and probe signals have different wavelengths and in general, the beat lengths for these two wavelengths are different. The third term will be small compared to the other terms if:

$$|(\beta_{1y} - \beta_{1x}) - (\beta_{2y} - \beta_{2x})|\, L > 2\pi \tag{3.22}$$

One can also think of this in terms of polarization evolution. The pump and probe evolve with two different beat lengths. In a Poincaré sphere representation, the Stokes vectors corresponding to the pump and probe signals rotate with different periods. If Eq. 3.22 is satisfied, the effect of the polarization-dependent terms becomes small. The sign of the birefringence is usually the same for the pump and probe signals. Therefore, if the inequality 3.22 holds, the inequality 3.21 will hold as well.

It is more useful to write the condition 3.22 in terms of the total differential group delay $\Delta\tau$ in the fiber and the frequency difference $\Delta\omega = |\omega_1 - \omega_2|$:

$$\Delta\omega \cdot \Delta\tau > 2\pi \quad, \tag{3.23}$$

where we have used the linear approximation:

$$
\begin{aligned}
|\beta_{1x} - \beta_{2x}| &\approx \beta'_x(\omega_1 - \omega_2) \\
|\beta_{1y} - \beta_{2y}| &\approx \beta'_y(\omega_1 - \omega_2) \quad,
\end{aligned}
\tag{3.24}
$$

where β'_x and β'_y are the first derivatives of the x and y components of propagation constant with respect to frequency evaluated at the mean frequency $\overline{\omega} = (\omega_1 + \omega_2)/2$. Condition

111

given by Eq. 3.23 can be rewritten in terms of the wavelengths λ_1 and λ_2:

$$\frac{c\Delta\lambda\Delta\tau}{\lambda_1\lambda_2} > 1 \quad , \tag{3.25}$$

where $\Delta\lambda = |\lambda_1 - \lambda_2|$ is the wavelength spacing and c is the velocity of light. In our experiments with the photonic crystal fiber we use a wavelength spacing similar to that used in the bismuth-oxide-based fiber experiment. Using this value and the amount of DGD in the fiber, the product $\Delta\omega \cdot \Delta\tau$ is about 10 which satisfies the condition.

It is interesting to note that in the bismuth-oxide-based fiber experiments, this product was about 8 times smaller and therefore it does not satisfy Eq. 3.23. This is why for lower pump power we saw a minimum of about 3dB of polarization dependence in the experimental results shown in Fig. 3.6 (b).

The final step in our analysis is to show that under this condition the XPM process will be polarization-independent. The key as we explained before is that Eq. 3.18 and 3.19 become decoupled when these conditions are satisfied. In order to have a polarization-independent behavior, Eqs. 3.18-3.19 should turn into two identical differential equations. From these equations, it is clear that we should launch the pump pulses such that their power is equal for both polarization states:

$$|A_{1x}(0,t)| = |A_{1y}(0,t)| = \sqrt{\frac{P(t)}{2}} \tag{3.26}$$

Before we proceed with the simplified formulas that describe the evolution of the probe components, we need to make one more assumption. In most signal processing applications, it is required that the total DGD ($\Delta\tau$) in the fiber be small compared with the pulse-widths used in the system. If this holds, we can:

- Eliminate the second term on the left-hand-side of 3.18 and 3.19 by solving the equations in a reference frame that is travelling at the average group velocity.

- Assume that the pump amplitude envelopes for x and y components remain approximately equal along the fiber:

$$|A_{1x}(z,t)| \approx |A_{1y}(z,t)| \approx \sqrt{\frac{P(t)}{2}} \tag{3.27}$$

We also assume that the group velocity dispersion (β_2'') is polarization-independent. With these assumptions, we can rewrite the simplified form of equations 3.18 and 3.19:

$$\frac{\partial A_{2x}}{\partial z} + \frac{i}{2}\beta_2''\frac{\partial^2 A_{2x}}{\partial T^2} \approx i\gamma\frac{4P(t)}{3}A_{2x} \tag{3.28}$$

$$\frac{\partial A_{2y}}{\partial z} + \frac{i}{2}\beta_2''\frac{\partial^2 A_{2y}}{\partial T^2} \approx i\gamma\frac{4P(t)}{3}A_{2y} \tag{3.29}$$

In these equation $T = t - \overline{\beta_2'}z$ is the time variable for the frame of reference moving with the average group velocity $\overline{\beta_2'}^{-1}$. Equations 3.28 and 3.29, describe two identical linear systems for the two probe polarization components. Therefore, any combination of x and y components with constant power generates the same nonlinear phase shift (XPM) at the

output.

In summary, in order to achieve polarization-independent XPM in birefringent fiber, we need to choose the fiber DGD and wavelength separation between pump and probe such that they satisfy Eq. 3.23. We also need to launch the pump signal such that its power is equally divided between the two fiber principal axes as described by Eq. 3.26.

3.2.2   CW Probe Experiment and Simulation Results

In order to prove this concept using the photonic crystal fiber (PCF) we set up an experiment similar to that shown in Fig. 3.5 . The main difference in this experiment is that the wavelengths used for pump and probe signals are 1545 nm and 1552 nm respectively. Fig. 3.22 (a) plots the minimum and maximum observed XPM spectra obtained by adjusting the probe polarization state while the pump polarization is adjusted to worst possible state. Based on our analysis, the worst choice for the polarization state of the pump signal is when it is aligned with one of the principal axes of the fiber, in which case only the co-polarized probe component experiences cross-phase modulation. In the experiment, there is no easy way to measure the light polarization right before entering or right after exiting the nonlinear fiber, because the PCF is spliced to an intermediate fiber and connector at each end. We experimentally find the worst state for the pump polarization by maximizing the observed difference between the minimum and maximum XPM spectra. Fig. 3.22 (b) plots the simulation results for the measurements plotted in part (a), assuming that the

probe is polarized along the principal axis of the fiber. The simulation is performed using the actual fiber parameters taking into account dispersion, birefringence and loss. There is a good agreement between the measurement and simulation and they both predict more than 6 dB of maximum polarization dependence.

The optimal state for pump polarization can also be achieved experimentally by adjusting the pump polarization until the XPM spectrum becomes insensitive to the probe polarization. Fig. 3.22 (c) plots the minimum and maximum XPM spectra observed when the pump polarization is optimally adjusted. In the simulation, we selected the pump polarization to be such that it equally excited the fiber principal axes. The result is plotted in Fig. 3.22 (d) which confirms our theoretical analysis and agrees with the measurements.

3.2.3   80 Gb/s Demultiplexing Experiment

Demultiplexing can be achieved by replacing the probe signal with the high-rate data signal (as explained in Sec. 3.1.7.) Similar to our previous experiments, we evaluate the system performance in the presence of polarization fluctuation introduced by a fast polarization scrambler. Fig. 3.23 shows our experimental setup for 80 Gb/s demultiplexing. In this experiment we employed a programmable polarization controller that can switch the input clock polarization state in order to find the best state. The programmable polarization controller allows us to better explore exactly which pump polarizations yield polarization-independent behavior. Fig. 3.24 plots the spectra of data and clock signals before they enter

polarization-dependent (worst case)

(a) MEASUREMENT

(b) SIMULATION

polarization-independent
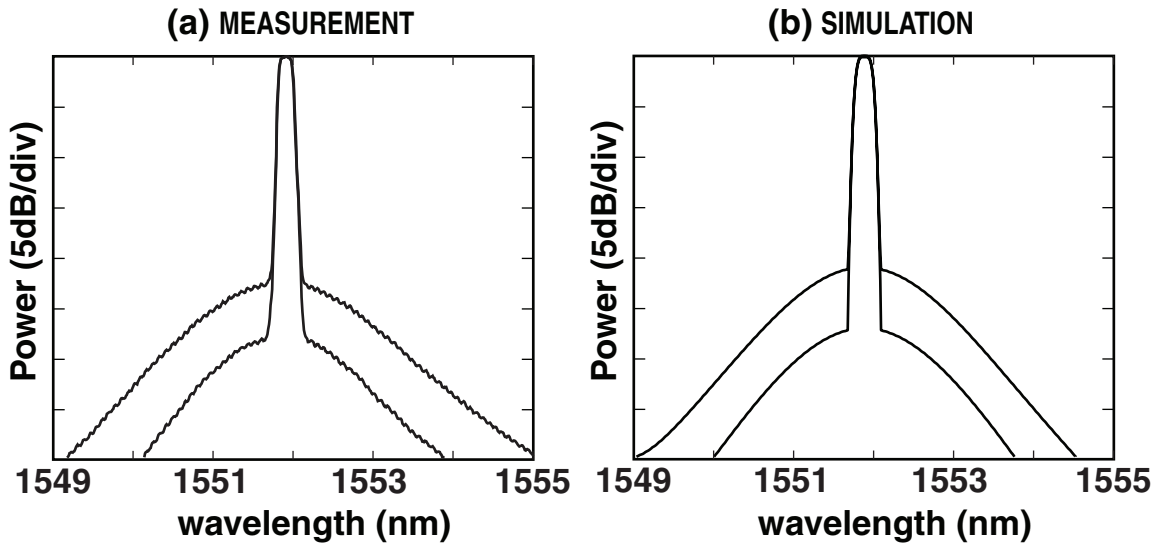
(c) MEASUREMENT
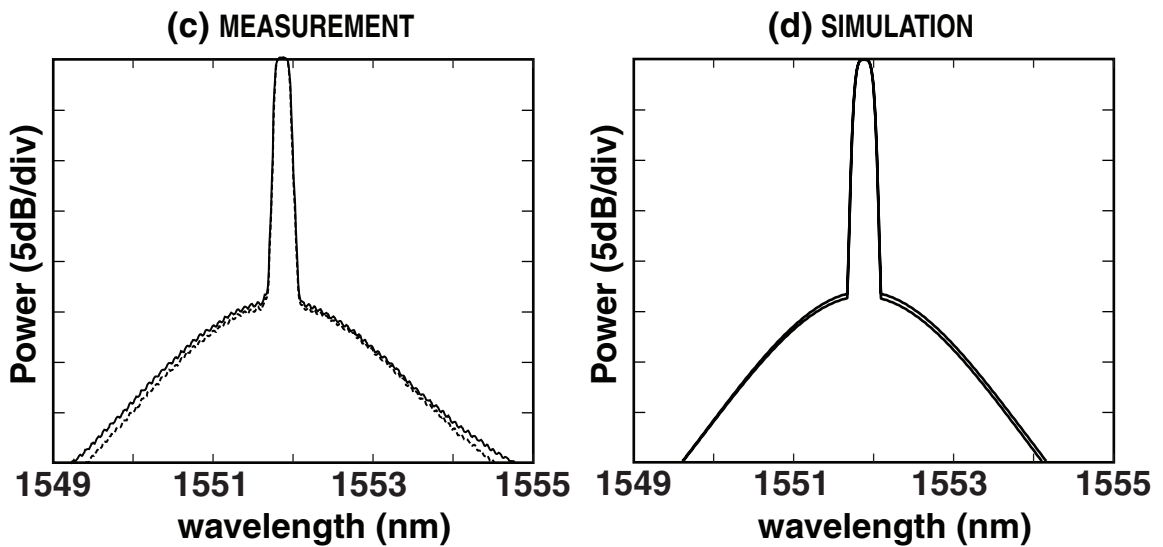
(d) SIMULATION

Fig. 3.22: Part (a) (measurement) and part (b) (simulation) plot the polarization dependence of XPM spectrum (two extreme probe polarization cases) while the pump polarization is adjusted to generate the maximum polarization dependence. Parts (c) and (d) plot the same spectra while the pump polarization state is chosen to minimize the polarization dependence.

116
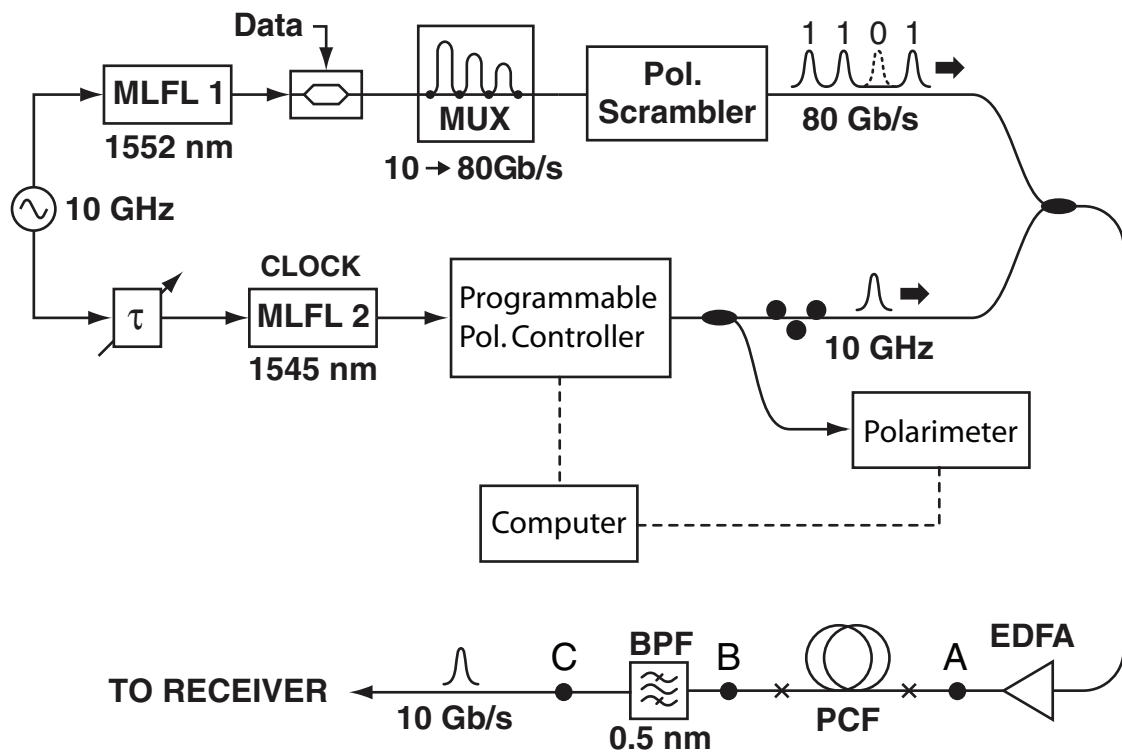
Fig. 3.23: Experimental setup used to demonstrate polarization-independent de-multiplexing in the photonic crystal fiber.

117
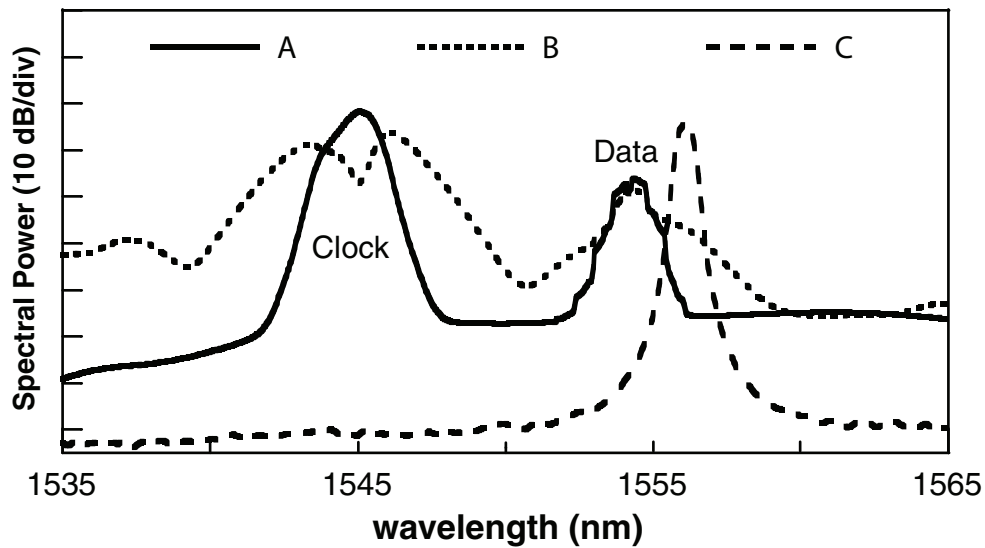
Fig. 3.24: Optical spectra measured at three different points (A,B,C) shown in Fig. 3.23.

the nonlinear fiber (point A), after exiting the nonlinear fiber (point B) and also after the bandpass filter (point C).

The 10 Gb/s demultiplexed signal can be analyzed on a sampling oscilloscope or bit-error-rate tester. Using these monitoring tools, we adjust the clock polarization state with the manual polarization controller until the lowest bit-error-rate (or cleanest eye diagram) is achieved. The goal is to demonstrate that low polarization sensitivity is achievable in this demultiplexing system. As a baseline for comparison, Fig. 3.25 (a) depicts the 10 Gb/s demultiplexed eye diagram when the data polarization is unscrambled. Part (b) of this fig-ure shows the same eye diagram when the data polarization is scrambled while the clock polarization state is adjusted to the worst state, maximizing the polarization dependence.

118

(a)

(b)

(c)

Pol. Scrambler
OFF

Clock SOP 1

POLARIZATION
DEPENDENT
(BER > 10^{-2})

Clock SOP 2

POLARIZATION
INDEPENDENT
(BER < 10^{-9})

Pol. Scrambler
ON

time (10 ps/div)
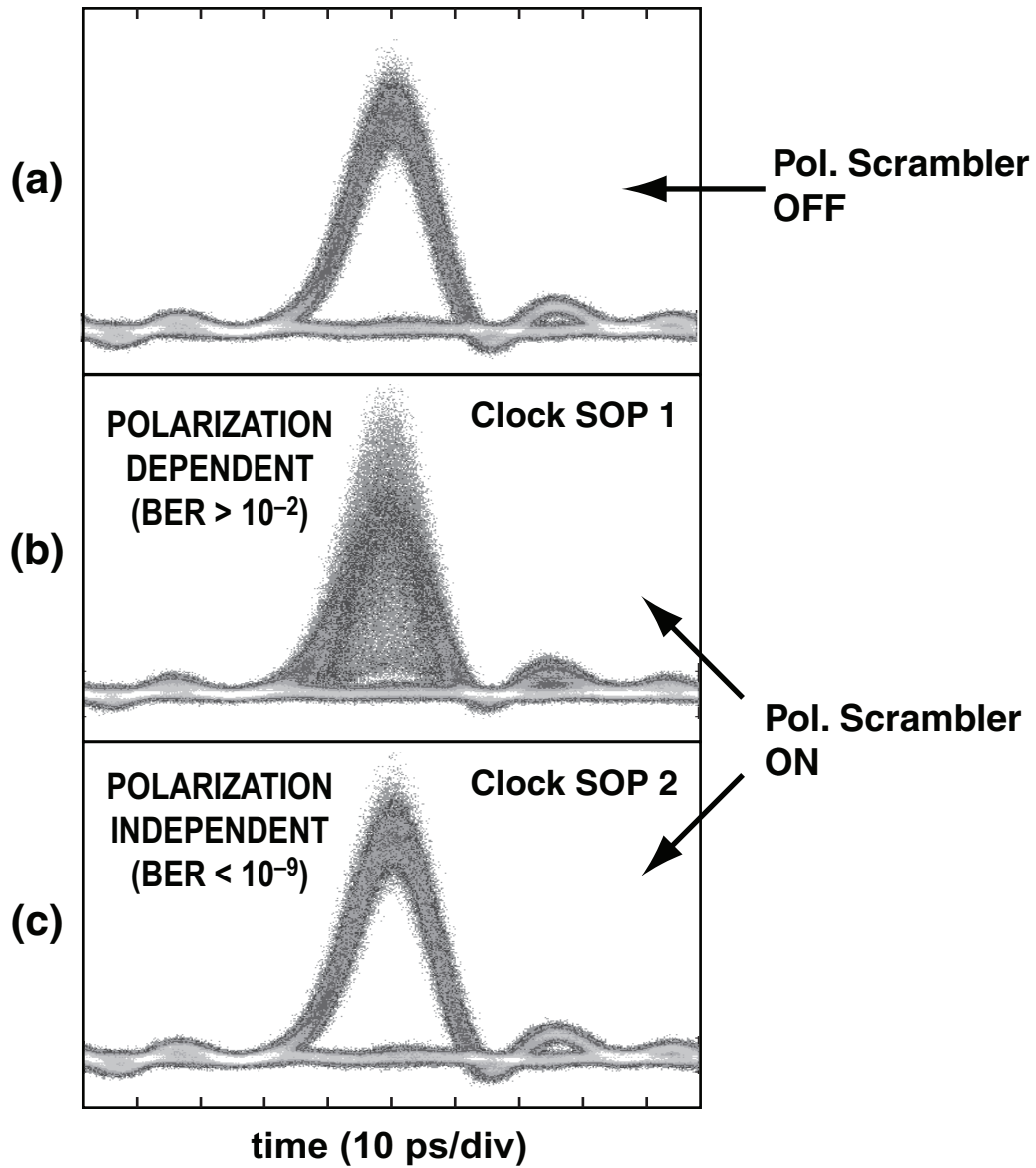
Fig. 3.25: (a) 10 Gb/s demultiplexed data eye diagram when the polarization scrambler is off. (b) data eye diagram when polarization scrambler is on and clock polarization is adjusted to the worst state. (c) data eye diagram when polarization scrambler in on and clock polarization is adjusted to the best state.
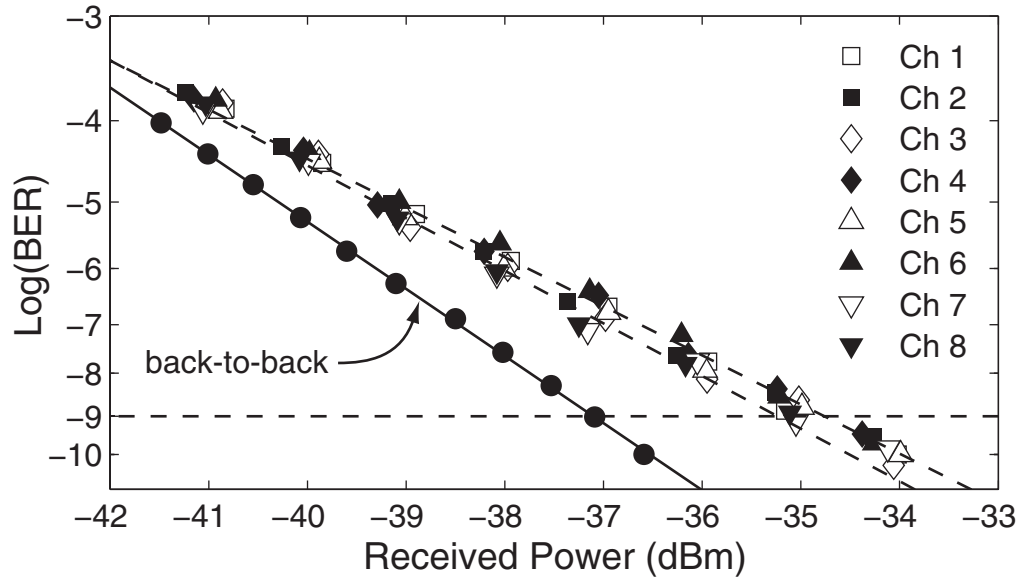
Fig. 3.26: BER vs. received power for 8 channels in the demultiplexing (80 Gb/s to 10 Gb/s) experiment showing very little difference between them. Back-to-back results are also shown.

Under this condition, the eye diagram is almost completely closed and the bit-error-rate is more than 10^{-2}. Part (c) shows the eye diagram when the scrambler is on and the clock polarization state is adjusted to give the lowest polarization dependence. In this case, the eye diagram is very similar to part (a) and the bit-error-rate is less than 10^{-9}. We also evaluated the demultiplexer by plotting the BER vs. received power for all 8 channels. These plots are shown in Fig. 3.26 demonstrating similar results for all 8 channels. The back-to-back results are also plotted showing about 2 dB of power penalty at 10^{-9} BER between the demultiplexed data and the back-to-back experiment. This penality is again attributed to extra amplification of the signal in the demultiplexing experiment which degrades the optical signal-to-noise ratio.
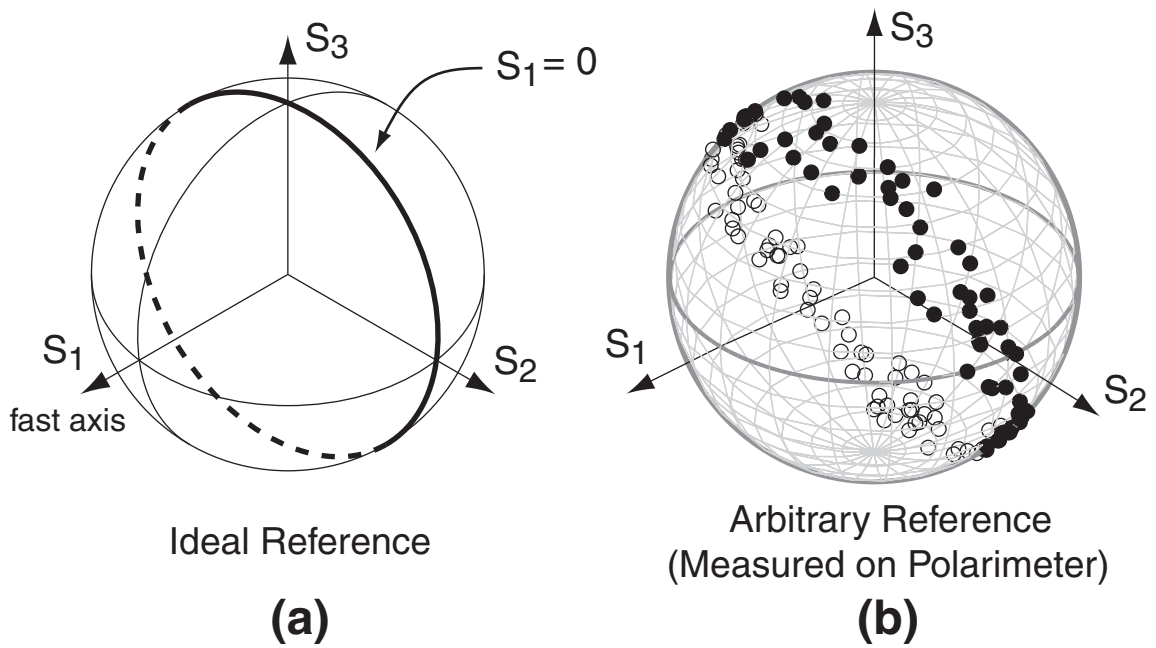
Fig. 3.27: (a) The circle including all pump polarization states that lead to polarization-independent XPM shown on Poincaré sphere with ideal reference axes. (b) The S parameters for the clock polarization states that lead to bit-error-rates $< 10^{-9}$ while data polarization is scrambled (reference for the Poincaré sphere is arbitrary due to measurement issues.)

As described in Eq. 3.26, the main condition to achieve polarization-independent XPM is to adjust the pump polarization state such that its power is divided equally between the two principal axes of the fiber. There is not just one polarization state that satisfies this condition, but a continuous range of states. On the Poincaré sphere, these states would follow a great circle passing through the two poles. Consider the Poincaré sphere representation for the input pump polarization state as shown in Fig. 3.27 (a). We choose the reference axes for this representation such that a linear polarization along the fast and slow axes of the fiber correspond to $S_1 = \pm 1$ respectively. It is easy to check that the condition for equally exciting the eigenstates of the fiber is equivalent to setting $S_1 = 0$ in this representation. As shown in Fig. 3.23, a programmable polarization controller systematically varies the pump polarization in a step-wise manner in order to cover the entire Poincaré sphere while data polarization is scrambled at a high speed. At each clock polarization state, the polarimeter reading for the clock signal and the bit-error-rate tester reading for the demultiplexed data signal are recorded. The polarimeter reading shows the Stokes parameters of the clock signal before entering the fiber in an arbitrary frame of reference. Because there are a few meters of fiber between the polarimeter and the splitter as well as between the splitter and the nonlinear fiber, there is no way to find the absolute polarization state going into the nonlinear fiber using this experimental setup. Nevertheless, the polarimeter does provide a picture of the relative polarization states, rotated on the Poincaré sphere by an unknown amount. In this experiment we are interested in showing that all clock polarization states that cause low bit-error-rates approximately lie on a circle. In this case we choose 10^{-9}

as our threshold for deciding if a bit-error-rate is low or high. Fig. 3.27 plots the Stokes parameter representation for all the points that lead to low BER. It can be seen that these points form a circle which confirms our theoretical analysis.

3.3 Summary

In summary, we developed two methods for performing polarization-independent cross-phase modulation in nonlinear fibers. Depending on the fiber parameters such as nonlinearity and birefringence, we suggested two different techniques for eliminating the polarization dependence. The first method suggests that if the nonlinear length of the fiber is small compared to the fiber length, a polarization-independent wavelength can be found in the XPM-induced spectrum. Using a narrow bandpass filter, this polarization-independent wavelength can be filtered out. The second method suggests that if the fiber birefringence is high enough, using a certain pump polarization state can make the XPM-induced spectrum insensitive to the probe polarization state. Both these methods were experimentally demonstrated and computer simulations were in agreement with the measurements. We also provided simple theoretical analysis that help in better understanding of these methods. Finally, we use both methods in high-speed OTDM demultiplexing experiments. In these experiments we evaluated our systems when the input data polarization was scrambled. As predicted, very low polarization dependence was observed in the demultiplexing experiments. The two demultiplexing systems discussed in this chapter have been reported

in [96, 97].

4. CONCLUSION AND FUTURE WORK

One of the main issues with optical signal processing using nonlinear optics is the polarization dependence. The main goal of this research was to provide solutions to this problem. In particular we tried to find polarization-insensitive techniques that can be used in an optical receiver in an OTDM network configuration. Two main stages in an OTDM receiver are the clock recovery and the demultiplexer. By building polarization-insensitive clock recovery and demultiplexing units, one of the main practical issues for these receivers can be solved.

In this work, we started by developing a clock recovery system based on two-photon absorption. One of the main motivations was that two-photon absorption exhibits lower polarization dependence compared to many other nonlinear processes. However, further studies showed that there is some polarization dependence in the TPA process. Using a theoretical model, we found a simple guideline for performing polarization-independent cross-correlation using TPA. This method was demonstrated experimentally and was the basis for our clock recovery experiments. In the clock recovery experiments that were performed at 80 Gb/s, we demonstrated very low polarization dependence. One realistic

method to evaluate the system for polarization dependence is to introduce random polarization fluctuations and monitor the system performance. The timing jitter of the recovered clock was monitored as the input data polarization was scrambled randomly. The results show a very low effect from the polarization scrambling on the timing jitter. Other advantages of using TPA for clock recovery include the fast response time allowing high speeds (much higher than 80 Gb/s) and broad optical wavelength range. Another way to test the system under realistic conditions is to perform transmission experiments. Our transmission experiments were done using recirculating fiber loops. Using our clock recovery system, we reached 840 km of transmission distance at 80 Gb/s while data polarization scrambling was used. Finally, we tested an improved system that is based on optical dithering. This system exhibits even lower polarization dependence and much lower dependence to the input data power and wavelength. Using this method we demonstrated a 10 dB dynamic range for the input data power and 40 nm operating wavelength range which was primarily limited by the EDFA bandwidth.

The next step in realizing polarization-independent OTDM receiver is to make a demultiplexing system that is not sensitive to the data polarization. One of the common methods for demultiplexing is using the cross-phase modulation in nonlinear fibers. There are methods for eliminating polarization dependence from the XPM process in fibers. All these methods involve twisting the fiber or using polarization diversity techniques that require higher powers and more complex systems. In this work, we showed two simple methods that do not require fiber twisting and do not add to the complexity of the system. This is

126

especially important because twisting the optical fiber is not practical for the new highly nonlinear fibers. Our first method that was demonstrated in bismuth-oxide-based fiber suggests that a polarization-independent wavelength can be found in the XPM spectrum. If such wavelength is found, it can be filtered out using a narrow bandpass filter. The nonlinear length should reach a minimum in order for this method to work properly. We demonstrated polarization-independent operation using both CW signal and pulsed signal as the probe input. The results were confirmed by computer simulations. Simple theoretical model was also provided that explains the principle of operation of this method. Demultiplexing was demonstrated using this technique at 160 Gb/s data rate. Again, the system evaluation was done using polarization scrambling. In this case the bit error rate and eye diagrams were monitored to ensure low polarization sensitivity. Our second method for polarization-independent XPM is based on fiber birefringence. First we showed theoretically that high enough birefringence in the fiber can lead to the elimination of the polarization-dependent terms in the XPM process. The condition under which this occurs depend on the fiber differential group delay and the wavelength separation between pump and probe signals. We used a 30m-long photonic crystal fiber in order to demonstrate this technique. Polarization-independent XPM was shown using CW probe signal and computer simulations confirmed the measurements. Optical demultiplexing at 80 Gb/s was performed while input polarization was scrambled. Very low polarization sensitivity was measured using BER and eye diagrams.

Due to equipment availability limitations, we were not able to put the two systems to-

gether in an OTDM receiver. This is usually difficult to do especially when the systems are not integrated. Our goal was to show that even though nonlinear processes are generally polarization dependent, methods can be invented to eliminate or minimize their polarization sensitivity. In particular, a high-speed polarization-independent OTDM receiver is realizable by integrating the clock recovery and demultiplexing systems in this work into one system. Therefore, one idea for future work is to design a receiver that includes the polarization-independent clock recovery and demultiplexing systems. Another interesting area to investigate is to study the behavior of the demultiplexing system in a long-haul transmission experiment similar to the one we described for the clock recovery experiments. This will demonstrate better the importance of a polarization-insensitive receiver.

Our methods for polarization-independent signal processing can be applied to other third-order nonlinear processes such as parametric amplification and four-wave mixing. Using the simulation tools that we developed in this work, such processes can also be numerically simulated. The concepts we used in cross-phase modulation experiments using nonlinear fiber can be modified in the case of these other processes.

APPENDIX

A. PHASE-LOCKED LOOP TRANSFER FUNCTION

In this appendix, we describe some of the details about the characteristics of the phase-locked loop (PLL). Fig. A.1 shows a simple block diagram for the PLL. Three main blocks can be seen in this diagram and we will try to explain the characteristics of each block first.

The first stage in a PLL is the phase detector. It is important to note that the term *phase* we does not refer to the phase of optical oscillations. It refers to the phase of the intensity modulation of the optical signal. A phase-detector in the case of optical clock recovery, measures the phase difference between an incoming data signal and a locally generated optical clock. Fig. A.2 shows the phase-detector circuit of our system. The photocurrent generated from the detector is converted to voltage and as we mentioned before an offset level is subtracted from that voltage in order to provide a bipolar signal. In order to reduce
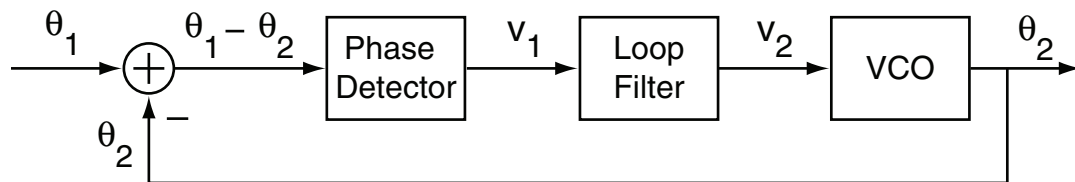
Fig. A.1: Block Diagram of a phase-locked loop.

130

Phase Detector, $H_{PD}(s)$
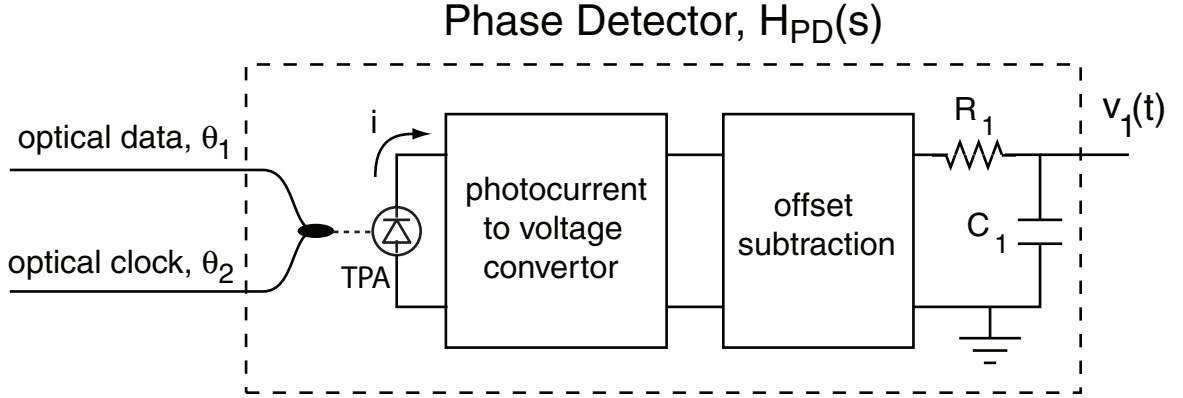
Fig. A.2: Diagram of the phase-detector section of the PLL used for optical clock recovery.

the noise from the detector circuit, we also add a low-pass filter after the voltage subtraction

circuit. The bandwidth of this filter should be larger that the closed-loop bandwidth of the

PLL. In our experiments, R_1 and C_1 were chosen such that the bandwidth of this lowpass

filter is about 25 kHz. The output of this stage $v_1(t)$ is usually referred to as the error signal

because it measured the phase discrepancy between the two inputs. The overall transfer

function of this stage can be written as:

$$H_{PD}(s) = \frac{V_1(s)}{\theta_1(s) - \theta_2(s)} = K_{PD}\frac{\omega_1}{s + \omega_1} \quad , \tag{A.1}$$

where K_{PD} determines the sensitivity of the phase-detector and $\omega_1 = 2\pi \times 25$ kHz is

the bandwidth of low-pass filter. It is important to measure the phase-detector sensitivity

in order to design the PLL with the desired characteristics. K_{PD} can be calculated by

measuring the error signal v_1 as a function of the phase difference $(\theta_1 - \theta_2)$.
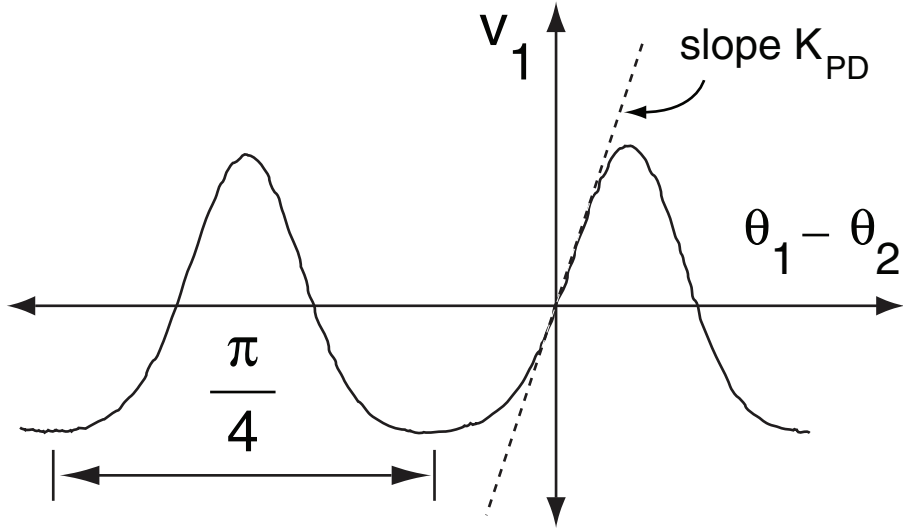
Fig. A.3: Measured error signal of the PLL as a function of the phase difference between the two optical inputs. Phase-detector sensitivity K_{PD} can be calculated by finding the slope of the tangent to the curve at the origin.

The measurement of this signal was previously described in section 2.3 and shown in Fig. 2.7. Here we have plotted the same error signal as a function of the phase difference between data and clock in Fig. A.3. It is important to note that the period of the error signal is $\frac{\pi}{4}$. This is because in our experiments we used 80 Gb/s data and 10 GHz clock. Therefore, clock and data pulses are aligned 8 times during one clock cycle. Also, the reference for the phases are chosen such that the error signal is zero when the phase difference is zero. Although the relationship between the error signal and the phase difference is nonlinear, it is linear in the proximity of the origin. When the PLL is locked, the phase difference will always be very small and in the proximity of the origin. Therefore, K_{PD} can be estimated by calculating the slope of the tangent to the curve at the origin. In our measurements, the
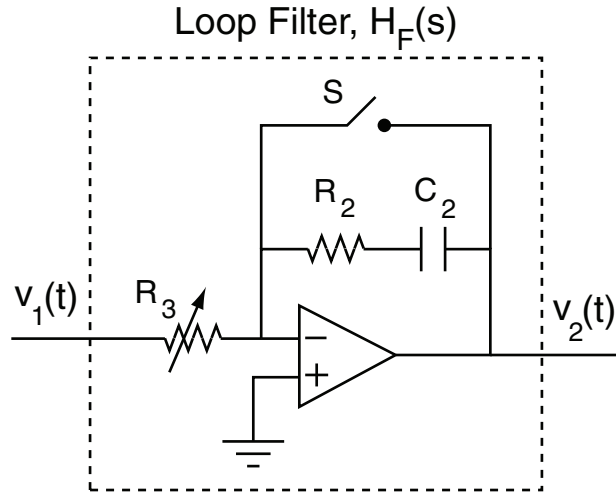
Fig. A.4: Loop filter circuit.

phase-detector sensitivity was calculated to be $K_{PD} \approx 1.2$ V/rad.

The second part of the PLL is the loop filter that we briefly mentioned in Section 2.3. In theory, one can design a PLL without using a loop filter. A variable attenuator is enough to control the bandwidth of the loop. However a simple attenuation of the error signal will limit the DC voltage entering the VCO. Therefore, the frequency range of the PLL will be extremely limited. An ideal loop filter for the PLL is comprised of an variable attenuator and an integrator. The integrator has an infinite DC gain and therefore it can provide any desired DC voltage to the VCO. Fig. A.4 shows the loop filter circuit. The transfer function of this circuit can be written as:

$$H_F(s) = \frac{V_2(s)}{V_1(s)} = K_A \frac{s + \omega_2}{s} \quad , \tag{A.2}$$

133

where K_A is the attenuation coefficient and ω_2 is determined by R_2 and C_2 values. In the circuit used in our experiments, R_1 is a variable resistor which controls the attenuation. For the representative measurements shown in Section 2.3 we set $K_A = 0.006$ and $\omega_2 = 2\pi \times 350$ Hz. The switch S shown in Fig. A.4 is used to enable or disable the PLL. When the switch is open, the PLL is enabled. When this switch is closed, the loop-filter transfer function is zero and therefore the PLL is disabled.

The last stage in the PLL is the voltage-controlled oscillator (VCO). If the input to the VCO is voltage v_2 and the output is the angle θ_2, the transfer function of an ideal VCO should be $\dfrac{1}{s}$. However, most VCOs have a limited bandwidth meaning that their frequency can follow the input voltage up to a certain speed. If the input voltage changes too rapidly, the output frequency does not adjust accordingly. Therefore, the sensitivity of the VCO drops as the input voltage frequency increases. Therefore, in a simplified case, the transfer function for the VCO can be written as a low-pass filter cascaded with an ideal VCO:

$$H_{VCO}(s) = \frac{\theta_2(s)}{V_2(s)} = K_{VCO}\frac{\omega_3}{s(s+\omega_3)} \quad , \tag{A.3}$$

where ω_3 is the bandwidth and K_{VCO} is the low-frequency sensitivity of the VCO. The measured normalized VCO sensitivity as a function of input frequency is plotted in Fig. A.5. Note that by normalized VCO sensitivity we mean $\dfrac{\omega_3}{s+\omega_3}$. The dashed curve shows the best fit to the data based on Eq. A.3. The bandwidth used in the dashed curve that fits the data is $\omega_3 \approx 2\pi \times 4.5$ kHz. The measured value for the low-frequency sensitivity of the
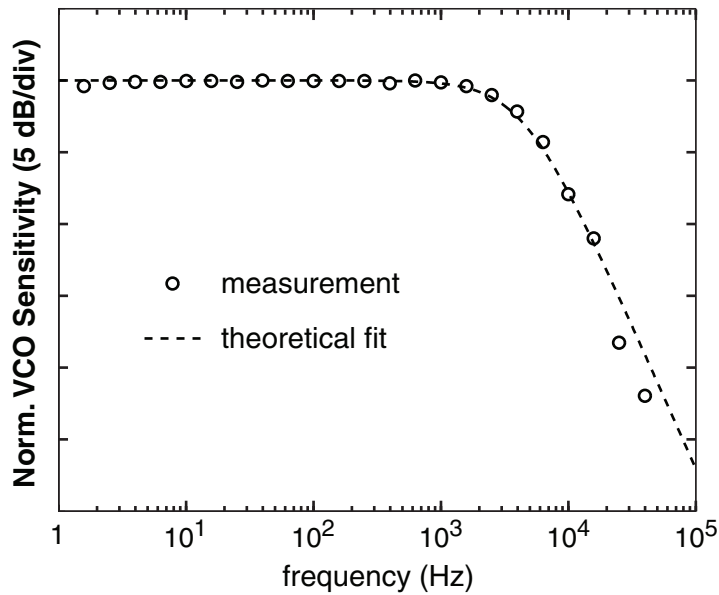
Fig. A.5: Normalized VCO sensitivity as a function of frequency. Circles indicate the measured data and the dashed curve shows the theoretical fit to the data.

VCO is $K_{VCO} \approx 2\pi \times 530$ krad/V. The closed-loop transfer function of the PLL can be found using the three transfer functions that we discussed above:

$$H_{PLL}(s) = \frac{H_{PD}(s)H_F(s)H_{VCO}(s)}{1 + H_{PD}(s)H_F(s)H_{VCO}(s)} \tag{A.4}$$

The frequency response and step response plotted in Fig. 2.8 were calculated using this formula and the transfer functions discussed in this appendix. We can easily see that the closed-loop PLL has a third order transfer function. The transfer function slope at frequencies higher than the closed-loop bandwidth (5.5 kHz) initially is 40 dB/dec and eventually changes to 60 dB/dec.

B. ANALYSIS OF POLARIZATION DEPENDENCE IN TWO-PHOTON ABSORPTION

In order to analyze the polarization dependence of two-photon absorption in a material, first we need to know about the nonlinear $\chi^{(3)}$ tensor for that material. There are different symmetry properties for the $\chi^{(3)}$ tensor depending on the material structure [59]. In this Appendix, we only focus on a specific case that applies to isotropic materials as well as crystalline structure with $m3m$, $\overline{4}3m$ or 432 symmetry. In these case there are generally 4 independent variables in the $\chi^{(3)}$ tensor: χ_{1122}, χ_{1212}, χ_{1221}, χ_{1111}. For TPA process, permutation symmetry [59] yields: $\chi_{1212} = \chi_{1122}$. Therefore, in the case of TPA, there are generally 3 independent parameters.

The difference between isotropic and anisotropic material in this case is that for an isotropic material:

$$\chi_{1111} = \chi_{1122} + \chi_{1212} + \chi_{1221} \; , \; (1, 2 = x, y, z) \tag{B.1}$$

But this relationship is not true for an anisotropic crystal and we can introduce a new

parameter as the anisotropy factor [54]:

$$\sigma = \frac{\chi_{1111} - (2\chi_{1212} + \chi_{1221})}{\chi_{1111}} \tag{B.2}$$

where we have used $\chi_{1122} = \chi_{1212}$ assuming two-photon absorption process. This factor is zero for an isotropic medium and can be estimated based on quantum mechanics for some materials. The numerical value of σ calculated for two some zincblende semiconductor materials are given in [54]. We were not able to find this number for silicon but our experimental results presented in Chapter 2 confirm that the anisotropy factor is very small for silicon.

In this analysis we assume a plane wave propagation model for simplicity. In order to find the expression for the TPA coefficient β (defined by Eq. 2.2) we first write the nonlinear polarization vector [59]:

$$\mathbf{P}^{\mathrm{NL}} = 3\epsilon_0 \left[2\chi_{1212} \left(\mathbf{E} \cdot \mathbf{E}^* \right) \mathbf{E} + \chi_{1221} \left(\mathbf{E} \cdot \mathbf{E} \right) \mathbf{E}^* + \sigma \chi_{1111} \sum_i |E_i|^2 E_i \hat{i} \right] \tag{B.3}$$

where $i = x, y, z$ and $\mathbf{E}$ is the electric field vector of a wave propagating in the direction of a unit vector $\hat{\eta}$ such that $\hat{\eta} \cdot \mathbf{E} = 0$. If η is the coordinate in the direction of propagation (which need not be x, y or z), we can write $\mathbf{E}(\eta) = \frac{1}{2}\mathbf{A}(\eta)e^{-jk\eta}$, where $\mathbf{A}(\eta)$ is the slowly varying amplitude vector. The factor of $\frac{1}{2}$ comes from the fact that we need to add two terms at frequencies ω and $-\omega$ in order to get a real-valued electric field. The wave

equation can be written as:

$$\frac{d^2\mathbf{E}(\eta)}{d\eta^2} + \frac{n^2\omega^2}{c^2}\mathbf{E}(\eta) = -\mu_0\omega^2\mathbf{P}^{NL}(\eta) \tag{B.4}$$

By substituting the slowly varying amplitude and writing the time-average intensity of light as:

$$I = \frac{n}{2}\left(\frac{\epsilon_0}{\mu_0}\right)^{\frac{1}{2}}|A|^2 \quad, \tag{B.5}$$

we get to the equation that describes the evolution of light intensity inside the medium:

$$\frac{\partial I(\eta)}{\partial \eta} = -\frac{3\omega}{2\epsilon_0 n^2 c^2}\left[2\mathsf{Im}(\chi_{1212}) + \mathsf{Im}(\chi_{1221})\frac{|\mathbf{A}\cdot\mathbf{A}|^2}{|\mathbf{A}|^4} + \sigma\mathsf{Im}(\chi_{1111})\frac{\sum_i|A_i|^4}{|\mathbf{A}|^4}\right]I^2(\eta) \tag{B.6}$$

By introducing the unit vector $\hat{p} = \dfrac{\mathbf{A}}{|\mathbf{A}|}$ which is the unit vector representing the polarization state we can write the TPA coefficient for the medium:

$$\beta = \frac{3\omega}{2\epsilon_0 n^2 c^2}\left[2\mathsf{Im}(\chi_{1212}) + \mathsf{Im}(\chi_{1221})\,|\hat{p}\cdot\hat{p}|^2 + \sigma\mathsf{Im}(\chi_{1111})\sum_i|p_i|^4\right] \tag{B.7}$$

This formula is given in [54]. Unit vector $\hat{p}$ can be complex, to accommodate circular and elliptical states, provided that $\hat{p}\cdot\hat{p}^* = 1$.

Now let us consider the special case of isotropic material. We should also note that different physical mechanisms may lead to the nonlinear susceptibility. In the case of the semiconductor materials the most important mechanism is the non-resonant electronic

response which provides $\chi_{1221} = \chi_{1212}$ [59]. Using this condition and assuming $\sigma = 0$ we can simplify Eq. B.6. We rewrite the right-hand-side of this equation in terms of A instead of the intensity:

$$\frac{\partial I(\eta)}{\partial \eta} = -\frac{2\omega \text{Im}(\chi_{1111})}{\mu_0 c^2} \left[2|\mathbf{A}|^4 + |\mathbf{A} \cdot \mathbf{A}|^2 \right] \tag{B.8}$$

Therefore, if the detector consists of a thin layer of absorbing material, the time-average photocurrent generated in the detector can be written as:

$$i_{\text{TPA}} \propto \left\langle 2|\mathbf{A}|^4 + |\mathbf{A} \cdot \mathbf{A}|^2 \right\rangle \tag{B.9}$$

In Section 2.4 we used Eq. 2.22 to derive our theoretical expressions for the polarization dependence. Therefore, it is desirable to show that Eq. B.9 is equivalent to Eq. 2.22. First we need to write down an expression that relates the complex field to the real-values electric field. For simplicity we write the electric field at point ($\eta = 0$). This is because the term $\exp(-jk\eta)$ is just a phase factor that will eventually go away in our calculation of the amount of power absorbed in the material:

$$\mathbf{E}(t) = \frac{1}{2}\mathbf{A}e^{j\omega t} + \frac{1}{2}\mathbf{A}^* e^{-j\omega t} \tag{B.10}$$

By substituting this expression for $\mathbf{E}(t)$ we can find the time-average value of $|\mathbf{E}(t)|^4$. After eliminating all the high-frequency terms we have:

$$\frac{1}{8} \left\langle 2|\mathbf{A}|^4 + |\mathbf{A} \cdot \mathbf{A}|^2 \right\rangle = \left\langle |\mathbf{E}(t)|^4 \right\rangle \quad , \tag{B.11}$$

which proves Eq. 2.22. In the case of two optical signals, we can used Eq. 2.22 if the wavelength separation between the two signals is within the slowly varying amplitude approximation condition. This means that that wavelength separation should be much smaller than the mean wavelength. In our experiments, we used optical signals with wavelength separations that satisfy this condition.

C. NUMERICAL SOLUTION FOR THE VECTOR NONLINEAR

SCHRODINGER EQUATIONS

Before explaining the vector form of nonlinear Schrodinger equation, we describe solving the scalar form of it using the split-step method. Consider the electric field propagating in the fiber:

$$E(x, y, x, t) = \phi(x, y)A(z, t)\exp(i\beta_0 z) \quad , \tag{C.1}$$

where $\phi(x, y)$ is the spatial distribution of the single mode supported by the fiber, $A(z, t)$ is the slowly varying amplitude, and $\beta_0 = \beta(\omega_0)$ is the propagation constant at frequency ω_0. For simplicity, we change the time variable to $T = t - \beta' z$. The light propagation in the fiber is described by the following nonlinear Schrodinger equation:

$$\frac{\partial A}{\partial z} = -\frac{i\beta''}{2}\frac{\partial^2 A}{\partial T^2} - \frac{\alpha}{2}A + i\gamma|A|^2 A \quad , \tag{C.2}$$

In this equation the first two terms on the right-hand-side describe the linear propagation of light while the last term describes the nonlinear propagation.

In order to solve this equation we split the fiber into N equal pieces of length dz. The

141
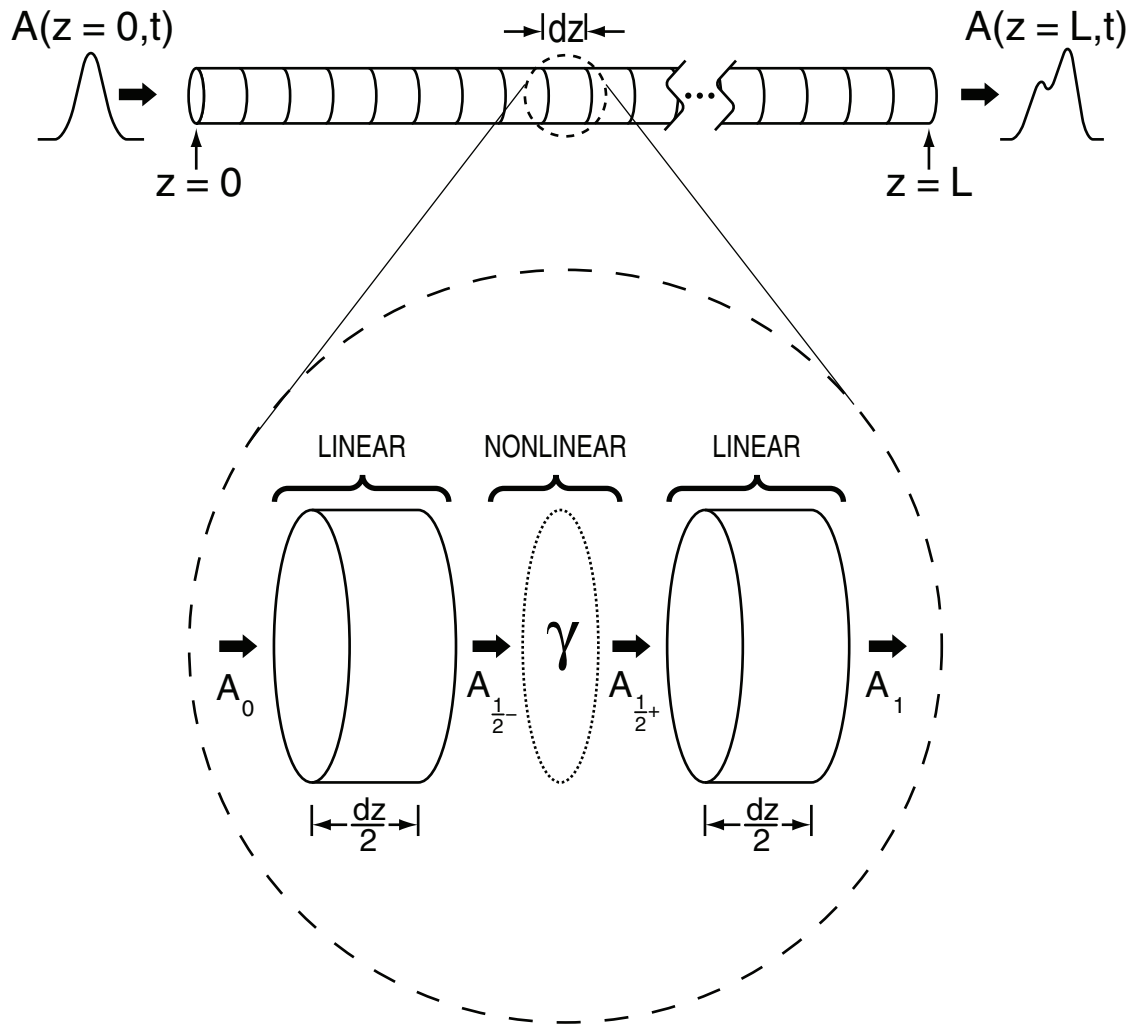
Fig. C.1: Simple diagram showing the split-step method for calculating a numerical solution for the nonlinear Schrodinger equation.

size of the step is determined by the nonlinearity in the fiber. If the fiber has zero nonlinearity, only one step can find the solution. If the nonlinearity is non-zero, the step size should satisfy the following condition:

$$\gamma P_{\max} dz \ll 1 \quad , \tag{C.3}$$

where $P_{\max}$ is the peak optical power in the fiber. Fig. C.1 shows how the split-step method works. Consider one of these steps with length dz as shown in the magnified diagram. Assume that the input to this step is A_0 and the step is divided into two equal substeps of length $\dfrac{dz}{2}$. First, the linear propagation of pulse is calculated in the first substep. The resulting electric field is called $A_{\frac{1}{2}-}$ and is given by:

$$A_{\frac{1}{2}-} = \mathsf{F}^{-1}\left(\mathsf{F}\left(A_0\right) e^{\left(-\frac{\alpha}{2}+i\beta(\omega)\right)dz/2}\right) \quad , \tag{C.4}$$

where $\mathsf{F}(\cdot)$ and $\mathsf{F}^{-1}(\cdot)$ are the Fourier transform and inverse Fourier transform respectively. In this case $\beta(\omega)$ only includes the second and higher order terms:

$$\beta(\omega) = \frac{1}{2}\beta''(\omega)\bigg|_{\omega=\omega_0} (\omega-\omega_0)^2 + ... \tag{C.5}$$

The nonlinearity effect is calculated in the middle of the step as shown in Fig. C.1. The slowly varying amplitude after the calculation of nonlinearity is called $A_{\frac{1}{2}+}$. The final output of the step is called A_1 and it is calculated similar to the first substep:

$$A_1 = \mathsf{F}^{-1}\left(\mathsf{F}\left(A_{\frac{1}{2}+}\right) e^{\left(-\frac{\alpha}{2}+i\beta(\omega)\right)dz/2}\right) \tag{C.6}$$

143

In order to complete the calculation we need to specify a formula to calculate $A_{\frac{1}{2}+}$ from $A_{\frac{1}{2}-}$. One method for approximating the nonlinear effect is to use the average of $|A_0|^2$ and $|A_1|^2$ in the nonlinear term of the equation:

$$A_{\frac{1}{2}+} \simeq A_{\frac{1}{2}-} e^{i\gamma(|A_0|^2+|A_1|^2)dz/2} \tag{C.7}$$

The calculation of A_1 depends on the calculation of $A_{\frac{1}{2}+}$. Therefore, an iterative method should be used in order to reach a minimum convergence tolerance. The final output of each step after enough number of iterations is used as the input to the next step.

The vector form of nonlinear Schrodinger equations is given in [82, 87, 98] and can be solved numerically using the same split-step method. The electric field vector is usually defined in this form:

$$E_j(x, y, z, t) = \phi(x, y) A_j(z, t) \exp(i\beta_{0j}z) \quad , \quad j = x, y \tag{C.8}$$

where $\phi(x, y)$ is the spatial distribution of the single mode supported by the fiber, $A_j(z, t)$ is the slowly varying amplitude, and $\beta_{0j} = \beta_j(\omega_0)$ is the corresponding propagation constant at frequency ω_0. The vector nonlinear Schrodinger equations that describe the evolution of the slowly varying amplitude in the fiber are given by:

$$\frac{\partial A_x}{\partial z} + \beta'_x \frac{\partial A_x}{\partial t} + \frac{i\beta''_{2x}}{2} \frac{\partial^2 A_x}{\partial t^2} + \frac{\alpha_x}{2} A_x = i\gamma \left(|A_x|^2 + \frac{2}{3}|A_y|^2 \right) A_x + \frac{i\gamma}{3} A_x^* A_y^2 \exp(-2i\Delta\beta z)$$

$$\tag{C.9}$$

$$\frac{\partial A_y}{\partial z} + \beta_y' \frac{\partial A_y}{\partial t} + \frac{i\beta_{2y}''}{2} \frac{\partial^2 A_y}{\partial t^2} + \frac{\alpha_y}{2} A_y = i\gamma \left(|A_y|^2 + \frac{2}{3}|A_x|^2 \right) A_y + \frac{i\gamma}{3} A_y^* A_x^2 \exp(2i\Delta\beta z)$$

(C.10)

In these equations, $\Delta\beta = \beta_{0x} - \beta_{0y} = \dfrac{2\pi}{L_B}$, where L_B is the beat length of the linearly birefringent fiber. For numerical analysis of the problem, it is more convenient to define the x-polarization and y-polarization components of the slowly varying amplitude in a way that they have the same phase velocity. Therefore, in our numerical simulations we used a slightly different definition for the field:

$$E_j(x, y, z, t) = \phi(x, y) A_j(z, t) \exp(i\overline{\beta_0} z) \quad , \quad j = x, y \quad , \qquad \text{(C.11)}$$

where $\overline{\beta_0}$ is in the vicinity of β_{0x} and β_{0y}. For example we can choose $\overline{\beta_0} = \dfrac{\beta_{0x} + \beta_{0y}}{2}$. Also, for simplicity of the equations we change the time variable to the one corresponding to the moving frame with the average group velocity. The new time variable is $T = t - \overline{\beta'} z$, where $\overline{\beta'}$ takes a value in the vicinity of β_x' and β_y', for example $\overline{\beta'} = \dfrac{\beta_x' + \beta_y'}{2}$. Using this new electric field definition and the new frame of reference, we can rewrite Eqs. C.9 and C.10:

$$\begin{aligned}
\frac{\partial A_x}{\partial z} =& i(\beta_{0x} - \overline{\beta_0}) A_x - (\beta_x' - \overline{\beta'}) \frac{\partial A_x}{\partial T} - \frac{i\beta_{2x}''}{2} \frac{\partial^2 A_x}{\partial T^2} - \frac{\alpha_x}{2} A_x \quad \text{(linear terms)} \\
&+ i\gamma \left(|A_x|^2 + \frac{2}{3}|A_y|^2 \right) A_x + \frac{i\gamma}{3} A_x^* A_y^2 \quad \text{(nonlinear terms)}
\end{aligned}$$

(C.12)

$$\frac{\partial A_y}{\partial z} = i(\beta_{0y} - \overline{\beta_0})A_y - (\beta'_y - \overline{\beta'})\frac{\partial A_y}{\partial T} - \frac{i\beta''_{2y}}{2}\frac{\partial^2 A_y}{\partial T^2} - \frac{\alpha_y}{2}A_y \quad \text{(linear terms)}$$

$$+ i\gamma\left(|A_y|^2 + \frac{2}{3}|A_x|^2\right)A_y + \frac{i\gamma}{3}A_y^* A_x^2 \quad \text{(nonlinear terms)}$$

(C.13)

These equations can be solved using a method similar to what was explained for the scalar case provided that the last nonlinear term vanishes. Based on an argument similar to the one discussed in Section 3.2.1, this term becomes negligible if $L_B < L$. This condition is satisfied by both fibers that were used in our experiments. After cancelling this term the simplified equations can be written as:

$$\frac{\partial A_x}{\partial z} \approx i(\beta_{0x} - \overline{\beta_0})A_x - (\beta'_x - \overline{\beta'})\frac{\partial A_x}{\partial T} - \frac{i\beta''_{2x}}{2}\frac{\partial^2 A_x}{\partial T^2} - \frac{\alpha_x}{2}A_x + i\gamma\left(|A_x|^2 + \frac{2}{3}|A_y|^2\right)A_x$$

(C.14)

$$\frac{\partial A_y}{\partial z} \approx i(\beta_{0y} - \overline{\beta_0})A_y - (\beta'_y - \overline{\beta'})\frac{\partial A_y}{\partial T} - \frac{i\beta''_{2y}}{2}\frac{\partial^2 A_y}{\partial T^2} - \frac{\alpha_y}{2}A_y + i\gamma\left(|A_y|^2 + \frac{2}{3}|A_x|^2\right)A_y$$

(C.15)

One difference between this case and the scalar case is that the propagation constant includes zeroth and first order terms as well. The nonlinear term is estimated by averaging the intensity of x and y components at the two ends of each step similar to the scalar case.

If the length of the fiber is smaller than the beat length, the foregoing approximation is not valid. We use a different method to simplify the equations in a form that can be solved using similar numerical approach. We use right-hand- and left-hand-circular components

for the slowly varying amplitude instead of the x and y components:

$$A_+ = \frac{1}{\sqrt{2}}\left(A_x + iA_y\right)$$
$$A_- = \frac{1}{\sqrt{2}}\left(A_x - iA_y\right)$$

(C.16)

Using these new variables, the nonlinear terms in Eqs. C.12 and C.13 can be written in the following form:

$$\frac{\partial A_+}{\partial z} = \frac{i2\gamma}{3}\left(|A_+|^2 + 2|A_-|^2\right)A_+$$
$$\frac{\partial A_-}{\partial z} = \frac{i2\gamma}{3}\left(|A_-|^2 + 2|A_+|^2\right)A_-$$

(C.17)

It is clear that the nonlinear terms in these equations are similar to the ones given in the scaler equation and therefore can be solved using the same numerical method. The transformations that relate A_+ and A_- to A_x and A_y are linear. Therefore, the solution to the linear part of the problem can easily be calculated for these new field variables. If $\hat{A}$ represents the Fourier transform of A, the solution for the linear propagation over a length Δz of the fiber based on Eqs. C.12 and C.13 is given by:

$$\hat{A}_x(z + \Delta z, \omega) = \exp\left[\left(-\frac{\alpha_x(\omega)}{2} + i\beta_x(\omega)\right)\Delta z\right]\hat{A}_x(z, \omega) = h_x(\omega)\hat{A}_x(z, \omega)$$
$$\hat{A}_y(z + \Delta z, \omega) = \exp\left[\left(-\frac{\alpha_y(\omega)}{2} + i\beta_y(\omega)\right)\Delta z\right]\hat{A}_y(z, \omega) = h_y(\omega)\hat{A}_y(z, \omega)$$

(C.18)

Using Eq. C.16, we can write the solution for the left-hand- and right-hand-circular com-

ponents:

$$\hat{A}_+(z + \Delta z, \omega) = \frac{1}{2} \left[h_x(\omega) + h_y(\omega) \right] \hat{A}_+(z, \omega) + \frac{1}{2} \left[h_x(\omega) - h_y(\omega) \right] \hat{A}_-(z, \omega)$$

$$\hat{A}_-(z + \Delta z, \omega) = \frac{1}{2} \left[h_x(\omega) - h_y(\omega) \right] \hat{A}_+(z, \omega) + \frac{1}{2} \left[h_x(\omega) + h_y(\omega) \right] \hat{A}_-(z, \omega)$$

(C.19)

In our simulations, we have confirmed that the approximation given by Eqs. C.14 and C.15 agrees with the solution using circular components for the electric field. This is due to the fact that the beat lengths for both fibers used in our experiments were much shorter than the fiber lengths. It is important to note that solving the problem using circular components for the field requires step sizes that are much smaller than the beat length.

BIBLIOGRAPHY

[1] M. Saruwatari. All-Optical Signal Processing for Terabit/Second Optical Transmission. 6(6):1363–1374, 2000.

[2] K. Kikuchi. All-optical signal processing using fiber nonlinearity. *Proc. Laser and Electro-Optics (LEOS) Conf.*, WI1:428–429, 2002.

[3] J. H. Lee, T. Tanemura, K. Kikuchi, T. Nagashima, T. Hasegawa, S. Ohara, and N. Sugimoto. Use of 1-m Bi_2O_3 nonlinear fiber for 160-Gbit/s optical time-division demultiplexing based on polarization rotation and a wavelength shift induced by cross-phase modulation. *Optics Lett.*, 30(11):1267–1269, 2005.

[4] C. Langrock, Kumar S, J. E. McGeehan, A. M. Willner, and M. M. Fejer. All-Optical Signal Processing Using $\chi^{(2)}$ Nonlinearities in Guided-Wave Devices. *Optics Communications*, 24(7):2579–2592, 2006.

[5] P. M. Krummrich and K. Kotten. Extremely fast (microsecond timescale) polarization changes in high speed long haul WDM transmission systems. *Proc. Optical Fiber Communications (OFC) Conf.*, FI3, 2004.

[6] O. Kamatani and S. Kawanishi. Ulta-High Speed Clock Recovery with Phase Lock

Loop Based on Four-Wave Mixing in a Travelling-Wave Laser Diode Amplifier. *Optics Communications*, 14(8):1757–1767, 1996.

[7] Y. Li, C. Kim, G. Li, Y. Kaneko, R. L. Jungerman, and O. Buccafusca. Wavelength and Polarization Insensitive All-Optical Clock Recovery From 96-Gb/s Data by Using a Two-Section Gain-Coupled DFB Laser. *IEEE Photon. Technol. Lett.*, 15(4):590–592, 2003.

[8] Y. Yang, Y. J. Wen, A. Nirmalathas, H. F. Liu, and D. Novak. Optical Clock Recovery at Line Rates via Injection Locking of a Long Cavity Fabry-Perot Lase Diode. *IEEE Photon. Technol. Lett.*, 16(6):1561–1563, 2004.

[9] T. Ohno, K. Sato, R. Iga, Y. Kondo, T. Ito, T. Furuta, K. Toshino, and H. Ito. Recovery of 160 GHz Optical Clock from 160 Gbit/s Data Stream Using Modelocked Laser Diode. *Electron. Lett.*, 40(4):265–267, 2004.

[10] Z. Hu, Hsu-Feng Chou, Kohsuke Nishimura, Masashi Usami, J. E. Bowers, and Daniel J. Blumenthal. Optical Clock Recovery Circuits Using Travelling-Wave Electroabsorption Modulator-Based Ring Oscillator for 3R Regeneration. *IEEE J. of Selected Topics in Quantum Electron.*, 11(2):329–337, 2005.

[11] J. Lasri, P. Devgan, R. Tang, and P. Kumar. Ultralow Timing Jitter 40 Gb/s Clock Recovery Using a Self-Staring Optoelectronic Oscillator. *IEEE Photon. Technol. Lett.*, 16(1):263–265, 2004.

[12] H. Tsuchida and M. Suzuki. 40 Gb/s Optical Clock Recovery Using an Injection-Locked Optoelectronic Oscillator. *IEEE Photon. Technol. Lett.*, 17(1):211–213, 2005.

[13] T. Saito, Y. Yano, and N. Henmi. Optical TDM 20 Gb/s-105 km Transmission Employing Newly Proposed Optical PLL Timing Extraction. *IEEE Photon. Technol. Lett.*, 6(4):555–557, 1994.

[14] E. Awad, P. S. Cho, N. Moulton, and J. Goldhar. Subharmonic Optical Clock Recovery From 160 Gb/s Using Time-Dependent Loss Saturation Inside a Single Electroabsorption Modulator. *IEEE Photon. Technol. Lett.*, 15(12):1764–1766, 2003.

[15] T. Yamamoto, L. K. Oxenlowe, C. Schmidt, C. Schubert, E. Hilliger, U. Feiste, J. Berger, R. Ludwig, and H. G. Weber. Clock recovery from 160 Gbit/s data signals using phase-locked loop with interferometric optical switch based on semiconductor optical amplifier. *Electron. Lett.*, 37(8):509–510, 2001.

[16] Dennis T. K. Tong, Benny Mikkelsen, Greg Raybon, Torben N. Nielsen, Kevin F. Dreyer, and John E. Johnson. Optoelectronic Phase-Locked Loop with Balanced Photodetection for Clock Recovery in High-Speed Optical Time-Division-Multiplexed Systems. *IEEE Photon. Technol. Lett.*, 12(8):1064–1066, 2000.

[17] C. Boerner, C. Schubert, C. Schmidt, E. Hilliger, V. Marembert, J. Berger, S. Ferber, E. Diertrich, R. Ludwig, B. Schmauss, and H. G. Weber. 160 Gb/s clock recovery with electro-optical PLL using bidirectionally operated electroabsorption modulator as phase comparator . *Electron. Lett.*, 39(14):1071–1073, 2003.

[18] Yang Jing Wen, Chang-Joong Chae, and Hai Feng Liu. Time-Domain Polarization Interleaving of Signal to Allow Polarization-Insensitive All-Optical Clock Recovery. *IEEE Photon. Technol. Lett.*, 17(6):1304–1306, 2005.

[19] T. Sakamoto, K. Seo, K. Taira, N. S. Moon, and K. Kikuchi. Polarization-Insensitive All-Optical Time-Division Demultiplexing Using a Fiber Four-Wave Mixer With a Peak-Holding Optical Phase-Locked Loop. *IEEE Photon. Technol. Lett.*, 16(2):563–565, 2004.

[20] T. Hasegawa, K. Inoue, and K. Oda. Polarization Independent Frequency Conversion by Fiber Four-Wave Mixing with a Polarization Diversity Technique. *IEEE Photon. Technol. Lett.*, 5(8):947–949, 1993.

[21] T. Miyazaki and T. Kubota. All-Optical Reshaping in a 160-Gb/s OTDM Receiver Using an XAM Gate Followed by an SPM Discriminator. *IEEE Photon. Technol. Lett.*, 16(8):1909–1911, 2004.

[22] T. Morioka, H. Takara, S. Kawanishi, K. Uchiyama, and M. Saruwatari. Polarization-Independent All-Optical Demultiplexing up to 200 Gbit/s Using Four-Wave Mixing in a Semiconductor Laser Amplifier. *Electron. Lett.*, 32(9):840–842, 1996.

[23] T. Yamamoto, E. Yoshida, and M. Nakazawa. Ultrafast Nonlinear Optical Loop Mirror for Demultiplexing 640 Gbit/s TDM Signals. *Electron. Lett.*, 34(10):1013–1014, 2000.

[24] K. Suzuki, K. Iwatsuki, S. Nishi, and M. Saruwatari. Error-Free Demultiplexing of 160 Gbit/s Pulse Signal Using Optical Loop Mirror Including Semiconductor Laser Amplifier. *Electron. Lett.*, 30(18):1501–1503, 1994.

[25] E. Tangdiongga, Y. Liu, H. de Waardt, G. D. Khoe, and H. J. S. Dorren. 320-to-40-gb/s demultiplexing using a single soa assisted by an optical filter. *IEEE Photon. Technol. Lett.*, 18(8):908–910, 2006.

[26] B.-E. Olsson and D. J. Blumenthal. All-Optical Demultiplexing Using Fiber Cross-Phase Modulation (XPM) and Optical Filtering. *IEEE Photon. Technol. Lett.*, 13(8):875–877, 2001.

[27] J. Toulouse. Optical Nonlinearities in Fibers: Review, Recent Examples, and Systems Applications. *Optics Communications*, 23(11):3625–3641, 2005.

[28] S. Bigo, O. Leclerc, and E. Desurvire. All-Optical Fiber Signal Processing and Regeneration for Soliton Communications. *IEEE J. of Selected Topics in Quantum Electron.*, 3(5):1208–1223, 1997.

[29] J. W. Lou, K. S. Jepsen, D. A. Nolan, S. H. Tarcza, W. J. Bouton, A. F. Evans, and M. N. Islam. 80 Gb/s to 10 Gb/s polarization-insensitive demultiplexing with circularly polarized spun fiber in a two-wavelength nonlinear optical loop mirror. *IEEE Photon. Technol. Lett.*, 12(12):1701–1703, 2000.

[30] T. Tanemura, J. Suzuki, K. Katoh, and K. Kikuchi. Polarization-Insensitive All-

Optical Wavelength Conversion Using Cross-Phase Modulation in Twisted Fiber and Optical Filtering. *IEEE Photon. Technol. Lett.*, 17(5):1052–1054, 2005.

[31] K. Utchiyama, S. Kawanishi, H. Takara, T. Morioka, and M. Saruwatari. 100Gbit/s to 6.3Gbit/s demultiplexing experiment using polarisation-independent nonlinear optical loop mirror. *Electron. Lett.*, 30(11):873–875, 1994.

[32] R. Calvani, F. Cisternin, R. Girardi, and E. Riccardi. Polarisation independent all-optical demultiplexing using four wave mixing in dispersion shifted fibre. *Electron. Lett.*, 35(1):72–73, 1999.

[33] K. K. Chow, C. Shu, C. Lin, and A. Bjarklev. Polarization-Insensitive Widely Tunable Wavelength Converter Based on Four-Wave Mixing in a Dispersion-Flattened Nonlinear Photonic Crystal Fiber. *IEEE Photon. Technol. Lett.*, 17(3):624–626, 2005.

[34] H. C. Lim, T. Sakamoto, and K. Kikuchi. Polarization-Independent Optical Demultiplexing by Conventional Nonlinear Optical Loop Mirror in a Polarization-Diversity Loop Configuration. *IEEE Photon. Technol. Lett.*, 12(12):1704–1706, 2000.

[35] B.-E. Olsson and P. A. Andrekson. Polarization-independent all-optical AND-gate using randomly birefringent fiber in a nonlinear optical loop mirror. 1998.

[36] L. P. Barry, P. G. Bollond, J. M. Dudley, J. D. Harvey, and R. Leonhardt. Autocorrelation of ultrashort pulses at 1.5 μm based on nonlinear response of silicon photodiodes. *Electron. Lett.*, 32(20):1922–1923, 1996.

[37] S. Jayaraman and C. Lee. Multiphoton Conductivity in Semiconductors and its Application to Ultra-Short Pulse Measurement. *J. Quantum Electron.*, 30(18):1501–1503, 1973.

[38] K. Kikuchi. Highly sensitive interferometric autocorrelator using si avalanche photodiode as two-photon absorber. *Electron. Lett.*, 34(1):123–125, 1998.

[39] K. Kikuchi, F. Futami, and K. Katoh. Highly sensitive and compact cross-correlator for measurement of picosecond pulse transmission characteristics at 1550 nm using two-photon absorption in si avalanche photodiode. *Electron. Lett.*, 34(22):2161–2162, 1998.

[40] B.C. Thomsen, L.P. Barry, J.M. Dudley, and J.D. Harvey. Ultra highspeed all-optical demultiplexing based on two-photon absorption in a laser diode. *Electron. Lett.*, 34(19):1871 – 1872, 1998.

[41] T. Inui, K.R. Tamura, K. Mori, and T. Morioka. Bit rate flexible chirp measurement technique using two-photon absorption. *Electron. Lett.*, 38(23):1459–1460, 2002.

[42] M. Dinu, D. C. Kilper, and H. R. Stuart. Optical Performance Monitoring Using Data Stream Intensity Autocorrelation. *Optics Communications*, 24(3):1194–1202, 2006.

[43] D. J. Moss, L. Fu, I. Littler, and B. J. Eggleton. Ultrafast all-optical modulation via two-photon absorption in silicon-on-insulator waveguides. *Electron. Lett.*, 41(6):320–321, 2005.

[44] A. P. Baronavski, H. D. Ladouceur, and J. K. Shaw. Analysis of Cross Correlation, Phase Velocity Mismatch, and Group Velocity Mismatched in Sum-Frequency Generation. *J. Quantum Electron.*, 29(2):580–589, 1993.

[45] K. Inoue and H. Toba. Wavelength Conversion Experiment Using Fiber Four-Wave Mixing. *IEEE Photon. Technol. Lett.*, 4(1):69–72, 1992.

[46] D. J. Ripin, C. Chudoba, J. T. Gopinath, J. G. Fujimoto, E. P. Ippen, U. Morgner, F. X. Kärtner, V. Scheuer, G. Angelow, and T. Tschudi. Generation of 20-fs pulses by a prismless Cr^{4+}:YAG laser. *Optics Lett.*, 27(1):61–63, 2002.

[47] Jinendra K. Ranka, Alexander L. Gaeta, Andrius Baltuska, Maxim S. Pshenichnikov, and Douwe A. Wiersma. Autocorrelation measurement of 6-fs pulses based on the two-photon-induced photocurrent in a gaasp photodiode. *Optics Lett.*, 22(17):1344–1346, 1997.

[48] R. Salem. Characterization of Two-Photon Absorption Detectors for Applications in High-Speed Optical Systems. *M.S. Thesis, Department of Electrical and Computer Engineering, University of Maryland, College Park*, 2003.

[49] M. Dinu, F. Quochi, and H. Garcia. Third-Order nonlinearities in silicon at telecom wavelengths. *Appl. Phys. Lett.*, 82(18):2954–2956, 2003.

[50] R. Claps, V. Raghunathan, D. Dimitropoulos, and B. Jalali. Influence of nonlinear absorption on Raman amplification in Silicon waveguides. *Optics Express*, 12(12):2774–2780, 2004.

[51] R. Salem, G. E. Tudury, T. U. Horton, G. M Carter, and T. E. Murphy. Polarization-Insensitive Optical Clock Recovery at 80 Gb/s Using a Silicon Photodiode. *IEEE Photon. Technol. Lett.*, 17(9):1968–1970, 2005.

[52] IEEE Standard Definitions of Physical Quantities for Fundamental Frequency and Time Metrology - Random Instabilities. *IEEE Std 1139-1999*.

[53] N. S. Bergano, F. W. Kerfoot, and C. R. Davidson. Margin Measurements in Optical Amplifier. *IEEE Photon. Technol. Lett.*, 5(3):304–306, 1993.

[54] Mark D. Dvorak, W. Andreas Schroeder, David R. Andersen, and Brian S. Wherrett Arthur L. Smirl. Measurement of the anisotropy of two-photon absorption coefficients in zincblende semiconductors. *J. Quantum Electron.*, 30(2):256–268, 1994.

[55] M. M. Karkhanehchi, J. H. Marsh, and D. C. Hutchings. Polarization dependence of two-photon absorption in an AlGaAs waveguide autocorrelator. *Appl. Opt.*, 36(30):7799–7801, 1997.

[56] K. R. Allakhverdiev, T. Baykara, S. Joosten, E. Gunay, A. A. Kaya, A. Kulibekov, A. Seilmeier, and E. Y. Salaev. Anisotropy of two-photon absorption in gallium selenide at 1064 nm. *Optics Comm.*, 261(1):60–64, 2006.

[57] D. C. Hutchings and B. S. Wherrett. Theory of anisotropy of two-photon absorption in zinc-blend semiconductors. *Phys. Review B*, 49(4):2418–2427, 1994.

[58] M. Murayama and T. Nakayama. Summetry-induced anisotropy of two-photon ab-

sorption spectra in zinc-blende semiconductors. *Phys. Review B*, 55(15):9628–9636, 1997.

[59] Robert W. Boyd. *Nonlinear Optics*. Academic Press, 1992.

[60] R. Salem and T. E. Murphy. Polarization-Insensitive Cross-Correlation Using Two-Photon Absorption in a Silicon Photodiode. *Optics Lett.*, 29(13):1524–1526, 2004.

[61] M. E. Marhic, K. K. Y. Wong, and L. G. Kazovsky. Fibre optical parametric amplifiers with circularly-polarised pumps. *Electron. Lett.*, 39(4):350–351, 2003.

[62] Y. Su, G. Raybon, R.-J. Essiambre, and L. Wickham. 80 gbit/s single-channel transmission over 1200 km of nonzero-dispersion fibre with 100 km amplifier spacing. *Electron. Lett.*, 38(12):573–574, 2002.

[63] J. Lou, M. Dennis, I. Duling, and T. Carruthers. Raman-pumped, dense dispersion-managed soliton transmission of 80 gb/s otdm data. *Proc. Optical Fiber Communications (OFC) Conf.*, WE7:335–336, 2003.

[64] G. C. Gupta, L. L. Wang, O. Mizuhara, R. E. Tench, N. N. Dang, P. Tabaddor, and A. Judy. 3.2 tb/s (40ch x 80 gb/s) transmission with spectral efficiency of 0.8 b/s/hz over 21 x 100 km of dispersion-managed high local dispersion fiber using all-raman amplified spans. *IEEE Photon. Technol. Lett.*, 15(7):996–998, 2003.

[65] J. P. Turkeiwicz, E. Tangdiongga, G. Lehmann, H. Rohde, W. Schairer, Y. R. Zhou,

E. S. R. Sikora, A. Lord, D. B. Payne, G.-D. Khoe, and H. DE Waardt. 160 gb/s otdm networking using deployed fiber. *Optics Communications*, 23(1):225–235, 2005.

[66] G. E. Tudury, R. Salem, G. M. Carter, and T. E. Murphy. Transmission of 80 Gbit/s over 840 km in standard fibre without polarisation control. *Electron. Lett.*, (accepted for publication), 2005.

[67] N. S. Bergano and C. R. Davidson. Circulating Loop Transmission Experiments for the Study of Long-Haul Transmission Systems Using Erbium-Doped Fiber Amplifiers. *Optics Communications*, 13(5):879–888, 1995.

[68] H. Xu, H. Jiao, L. Yan, and G. M. Carter. Measurement of Distributions of Differential Group Delay in a Recirculating Loop With and Without Loop-Synchronous Scrambling. *IEEE Photon. Technol. Lett.*, 16(7):1691–1693, 2004.

[69] Y. Sun, A. O. Lima, I. T. Lima, J. Zweck, L. Yan, C. R Menyuk, and G. M Carter. Statistics of the System Performance in a Scrambled Recirculating Loop With PDL and PDG. *IEEE Photon. Technol. Lett.*, 15(8):1067–1069, 2003.

[70] Q. Yu, L.-S. Yan, S. Lee, Y. Xie, and A. E. Willner. Loop-Synchronous Polarization Scrambling Technique for Simulating Polarization Effects Using Recirculating Fiber Loops. *Optics Communications*, 21(7):1593–1600, 2003.

[71] T. F. Carruthers and J. W. Lou. 80 to 10 Gbit/s clock recovery using phase detection with Mach-Zehnder modulator. *Electron. Lett.*, 37(14):906–907, 2001.

[72] I. D. Phillips, A. Gloag, P. N. Kean, N. J. Doran, I. Bennion, and A. D. Ellis. Simultaneous demultiplexing, data recognition, and clock recovery with a single semiconductor optical amplifier-based nonlinear-optical loop mirror. *Optics Lett.*, 22(17):1326–1328, 1997.

[73] J. Yu and P. Jeppesen. 80-Gb/s Wavelength Conversion Based on Cross-Phase Modulation in High-Nonlinearity Dispersion-Shifted Fiber and Optical Filtering. *IEEE Photon. Technol. Lett.*, 13(8):833–835, 2001.

[74] V. Perlin and H. G. Winful. All-Fiber Wavelength Conversion Using Cross-Phase Modulation and Bragg Gratings. *IEEE Photon. Technol. Lett.*, 14(2):176–178, 2002.

[75] C. Kolleck and U. Hempelmann. All-Optical Wavelength Conversion of NRZ and RZ Signals Using a Nonlinear Optical Loop Mirror. *Optics Communications*, 15(10):1906–1913, 1997.

[76] P. A. Andrekson, N. A. Olsson, J. R. Simpson, D. J. Digiovani, P. A. Morton, T. Tanbun-Ek, R. A. Logan, and K. W. Wecht. 64 Gb/s All-Optical Demultiplexing with the Nonlinear Optical-Loop Mirror. *IEEE Photon. Technol. Lett.*, 4(6):644–647, 1992.

[77] A. T. Clausen, A. I. Siahlo, J. Seoane, L. K. Oxenlowe, and P. Jeppesen. 320 to 10 Gb/s demultiplexing using a NOLM based on commercially available components. *Electron. Lett.*, 41(5):265–266, 2005.

[78] J. Yu, Y. Qian, P. Jeppesen, and S. N. Knudsen. Broad-Band and Pulsewidth-Maintained Wavalength Conversion Based on a High-Nonlinearity DSF Nonlinear Optical Loop Mirror. *IEEE Photon. Technol. Lett.*, 13(4):344–346, 2001.

[79] M. N. Islam, L. F. Mollenauer, R. H. Stolen, J. R. Simpson, and H. T. Shang. Cross-phase modulation in optical fibers. *Optics Lett.*, 12(8):825–827, 1987.

[80] G. P. Agrawal, P. L. Baldeck, and R. R. Alfano. Temporal and spectral effects of cross-phase modulation on copropagating ultrashort pulses in optical fibers. *Phys. Rev. A*, 40(9):5063–5072, 1989.

[81] N. Sugimoto, T. Nagashima, T. Hasegawa, S. Ohara, K. Taira, and K. Kikuchi. Bismuth-based optical fiber with nonlinear coefficient of 1360 $w^{-1}km^{-1}$. *Optical Fiber Communication Conference (PDP26)*, (PDP26), Feb. 2004.

[82] Govind P. Agrawal. *Nonlinear Fiber Optics*. Academic Press, 3rd edition, 2001.

[83] A. Boskovic, S. V. Chernikov, and J. R. Taylor. Direct continuous-wave measurement of n_2 in various types of telecommunication fiber at 1.55 μm. *Optics Lett.*, 21(24):1966–1968, 1996.

[84] Y. Namihira and J. Maeda. Comparison of Various Polarisation Mode Dispersion Measurement Methods in Optical Fibres. *Electron. Lett.*, 28(25):2265–2266, 1992.

[85] C. D. Poole and D. L. Favin. Polarization-Mode Dispersion Measurements Based on

Transmission Spectra Through a Polarizer. *Optics Communications*, 12(6):917–929, 1994.

[86] D. K. Gifford, B. J. Soller, M. S. Wolfe, and M. E. Froggatt. Polarization-Mode Dispersion Measurements Based on Transmission Spectra Through a Polarizer. *Appl. Opt.*, 44(34):7282–7286, 2005.

[87] C. R. Menyuk. Nonlinear Pulse-Propagation in Birefringent Optical Fibers. *J. Quantum Electron.*, 23(2):174–176, 1987.

[88] R. A. Fisher and W. K. Bischel. Numerical studies of the interplay between self-phase modulation and dispersion for intense plane-wave laser pulses. *Appl. Phys. Lett.*, 46(11):4921–4934, 1975.

[89] G. P. Agrawal and M. J. Potasek. Nonlinear pulse distortion in single-mode optical fibers at the zero-dispersion wavelength. *Phys. Review A*, 33(3):1765–1776, 2005.

[90] H. Ghafouri-Shiraz, P. Shum, and M. Nagata. A Novel Method for Analysis of Soliton Propagation in Optical Fibers. *J. Quantum Electron.*, 31(1):190–200, 1995.

[91] Q. Lin and G. P. Agrawal. Vector Theory of Cross-Phase Modulation: Role of Nonlinear Polarization Rotation. *J. Quantum Electron.*, 40(7):958–954, 2004.

[92] S. Kumar, A. Selvaraian, and G. V. Anand. Nonlinear copropagation of two optical pulses of different frequencies in birefringent fibers. *J. Opt. Soc. America B*, 11(5):810–817, 1994.

[93] T.-K. Chiang, N. Kagi, T. K. Fong, M. E. Marhic, and L. G. Kazovsky. Cross-Phase Modulation in Dispersive Fibers: Theoretical and Experimental Investigation of the Impact of Modulation Frequency. *IEEE Photon. Technol. Lett.*, 6(6):733–736, 1994.

[94] M. Shtaif. Analytical description of cross-phase modulation in dispersive optical fibers. *Optics Lett.*, 23(15):1191–1193, 1998.

[95] J. Li, B.-E. Olsson, M. Karlsson, and P. A. Andrekson. OTDM Add-Drop Multiplexer Based on XPM-Induced Wavelength Shifting in Highly Nonlinear Fiber. *Optics Communications*, 23(9):2654–2661, 2005.

[96] A. S. Lenihan, R. Salem, T. E. Murphy, and G. M. Carter. All-Optical 80 Gb/s Time-Division Demultiplexing Using Polarization-Insensitive Cross-Phase Modulation in Photonic Crystal Fiber. *to appear in IEEE Photon. Technol. Lett.*, 2006.

[97] R. Salem, A. S. Lenihan, G. M. Carter, and T. E. Murphy. 160 Gb/s Polarization-Independent Optical Demultiplexing in 2-m Bismuth-Oxide Fiber. *IEEE Photon. Technol. Lett.*, 2006.

[98] E. Seve, P. T. Dinda, G. Millot, M. Remoissenet, J. M. Bilbault, and M. Haelterman. Modulation instability and critical regime in a highly birefringent fiber. *Phys. Review A*, 54(4):3519–3534, 1996.